Photoluminescence Studies of InGaN/GaN Quantum Well Structures

A thesis submitted to the University of Manchester for the degree of
Doctor of Philosophy
in the Faculty of Science and Engineering

2018

George M. Christian
School of Physics and Astronomy

Contents

Word count: 34 122

Photoluminescence Studies of InGaN/GaN Quantum Well Structures

George M. Christian

A thesis submitted to the University of Manchester for the degree of Doctor of Philosophy

Abstract

In this thesis, optical studies of *c*-plane InGaN/GaN quantum well (QW) structures are presented.

The effects of a Si-doped underlayer (UL) on the optical properties of multiple quantum well (MQW) structures are investigated. The QW photoluminescence (PL) emission peak energy and radiative recombination rate decrease and increase respectively with increasing number of QWs. These observations are attributed to the increasing net electric field across the MQW structure as the strength of the surface polarisation field, which acts in the opposite sense to the piezoelectric polarisation fields across the QWs, reduces with increasing distance of the UL from the sample surface. This leads to a reduction in the electron-hole recombination energy and wavefunction overlap. It is also shown that the internal quantum efficiency of the MQW structures may decrease with increasing number of QWs due to the reducing radiative recombination rate, which could indicate that carrier losses due to thermionic emission or interface recombination are mitigated by the inclusion of an UL.

Optical studies of single QW structures containing Si-doped ULs with different net electric fields across the QW are presented. The net electric field across the QW is changed by varying the thickness of the GaN cap layer. The full width at half maximum of the emission peak increases with increasing net electric field across the QW. This is attributed to the increasing variation in electron ground state energies due to the role of the electric field in the localisation of electrons at quantum well width fluctuations. For one sample, a smaller Huang-Rhys factor compared to the rest of the samples is calculated. The non-exponential PL decays detected on the low energy side of the QW emission peak from this sample are also of a different shape to the other PL decays detected at all energies for the other samples. This may be due to the reversal of the net electric field across these QW regions.

Observations of a broad emission band on the high energy side of single QW structures at high excited carrier densities are presented. This band occurs in the carrier density regime at which the efficiency droop is observed. The emission band is attributed to higher energy weakly localised or delocalised electron and hole states that are populated following the saturation of the localised ground states. PL decay curves detected across this emission band exhibit plateaus where the PL intensity remains constant until the higher energy emission has decayed. These are similar to decays observed in semiconductor quantum dots, which are characteristic of Pauli state blocking.

Declaration

No portion of the work referred to in the thesis has been submitted in support of an application for another degree or qualification of this or any other university or other institute of learning.

Copyright

i The author of this thesis (including any appendices and/or schedules to this thesis) owns certain copyright or related rights in it (the "Copyright") and he has given The University of Manchester certain rights to use such Copyright, including for administrative purposes.

ii Copies of this thesis, either in full or in extracts and whether in hard or electronic copy, may be made only in accordance with the Copyright, Designs and Patents Act 1988 (as amended) and regulations issued under it or, where appropriate, in accordance with licensing agreements which the University has from time to time. This page must form part of any such copies made.

iii The ownership of certain Copyright, patents, designs, trademarks and other intellectual property (the "Intellectual Property") and any reproductions of copyright works in the thesis, for example graphs and tables ("Reproductions"), which may be described in this thesis, may not be owned by the author and may be owned by third parties. Such Intellectual Property and Reproductions cannot and must not be made available for use without the prior written permission of the owner(s) of the relevant Intellectual Property and/or Reproductions.

iv Further information on the conditions under which disclosure, publication and commercialisation of this thesis, the Copyright and any Intellectual Property and/or Reproductions described in it may take place is available in the University IP Policy[1], in any relevant Thesis restriction declarations deposited in the University Library, The University Library's regulations[2] and in The University's policy on Presentation of Theses.

[1] `http://documents.manchester.ac.uk/DocuInfo.aspx?DocID=24420`
[2] `http://www.library.manchester.ac.uk/about/regulations/`

Acknowledgements

Firstly, I would like to thank my supervisor, Phil Dawson, for his invaluable support and guidance over the last four years.

Thanks to Simon Hammersley and Matt Davies for all the help they gave me when I was starting out. Thanks also to the other members of the research group, past and present, for making the experience an enjoyable one: Stephen Church, Lydia Jim, Will Blenkhorn, Danny Sutherland, Marina Leontiadou, Dave Binks and Peter Mitchell.

I am grateful to colleagues at the Department of Materials Science and Metallurgy, University of Cambridge, for providing me with the samples that I studied in this work as well as their expertise in structural characterisation. Thanks in particular to Rachel Oliver, Colin Humphreys, Menno Kappers and Fabien Massabuau for the many helpful discussions and for making me feel welcome in Cambridge. Thanks also to Stefan Schulz from the Tyndall National Institute in Cork for the helpful discussions around the theoretical side of this work.

Thanks as well to all of the friends I have made over the last four years, and to those who have stuck around from before then, especially all of my house- and flat-mates from the various places I have lived in Manchester. You are the reason that this city has felt like home for eight years. Special thanks go to Kate for putting up with me over the last few months when I might have been a bit too distracted by this document!

Finally, I would like to thank my mum, Josie, and my dad, John, for the love and support that they have continued to provide me in everything that I do.

List of Publications

[1] G. M. Christian *et al.* "Optical properties of c-Plane InGaN/GaN single quantum wells as a function of total electric field strength" (2018), Submitted.

[2] G. M. Christian *et al.* "Recombination from polar InGaN/GaN quantum well structures at high excitation carrier densities". *Physical Review B* **98**, 15 (2018), 155301. DOI: 10.1103/PhysRevB.98.155301.

[3] G. Christian *et al.* "Effects of a Si-doped InGaN Underlayer on the Optical Properties of InGaN/GaN Quantum Well Structures with Different Numbers of Quantum Wells". *Materials* **11**, 9 (2018), 1736. DOI: 10.3390/ma11091736.

[4] G. M. Christian *et al.* "Room temperature PL efficiency of InGaN/GaN quantum well structures with prelayers as a function of number of quantum wells". *physica status solidi (c)* **13**, 5-6 (2016), 248. DOI: 10.1002/pssc.201510180.

List of Figures

List of Tables

List of Abbreviations

1T	single-temperature
2T	two-temperature
AFM	atomic force microscopy
APT	atom probe tomography
CB	conduction band
CFD	constant fraction discriminator
CL	cathodoluminescence
CW	continuous-wave
EL	electroluminescence
EQE	external quantum efficiency
FWHM	full width at half maximum
HEB	high energy band
IQE	internal quantum efficiency
LED	light emitting diode
LEEBI	low energy electron beam irradiation
LO	longitudinal optical
MBE	molecular beam epitaxy
MCA	multi-channel analyser
MCP	micro-channel plate
MOVPE	metalorganic vapour phase epitaxy
MQW	multiple quantum well
PC	personal computer

PL	photoluminescence
PMT	photomultiplier tube
Q2T	quasi-two-temperature
QCSE	quantum confined Stark effect
QD	quantum dot
QW	quantum well
QWWF	quantum well width fluctuation
RGB	red-green-blue
SRH	Shockley-Read-Hall
TAC	time-to-amplitude converter
TCSPC	time-correlated single photon counting
TEM	transmission electron microscopy
TIPL	time-integrated photoluminescence
TRPL	time-resolved photoluminescence
UL	underlayer
UV	ultraviolet
VB	valence band
VLC	visible light communication
XRD	X-ray diffraction

Chapter 1

Introduction

The group III-nitrides, that is gallium nitride, indium nitride and aluminium nitride (hereafter referred to as GaN, InN and AlN, respectively) and their ternary and quaternary alloys form an important group of compound semiconductors with direct bandgaps. They have made possible the development of highly efficient light emitting diode (LED)-based light sources, as well as short-wavelength semiconductor laser diodes. The low temperature (0 K) bandgaps of the materials range from 0.78 eV for InN to 6.25 eV for AlN [1], with the intermediate energies achieved through alloying of the materials. This means that they can potentially provide light emission and detection ranging from the infrared through to the ultraviolet (UV) region of the electromagnetic spectrum, leading many research groups to pursue them as the active regions in LEDs and lasers.

1.1 Applications

Because of the wide range of bandgaps covered by the group III-nitrides, there has been considerable research into their potential as light emitters across the visible spectral range. Initially, the most intensive work was into developing a blue LED based on GaN (and later InGaN) since a device emitting light efficiently in this range

had yet to be realised [2]. Since the advent of the first highly efficient blue LED [3] the development and adoption of solid state white lighting, usually comprising a blue LED coated in a yellow phosphor [2, 4], has been rapid. Internal quantum efficiencies (IQEs), that is the fraction of electron-hole recombination events that are radiative, greater than 90 % have been reported for blue InGaN/GaN quantum wells (QWs) [5, 6], leading to external quantum efficiencies (EQEs) (in which the current injection and light extraction efficiencies are included) of over 80 % for blue and violet LEDs [7, 8]. Commercial white LEDs have a luminous efficacy greater than $150\,\mathrm{lm\,W^{-1}}$, which is significantly greater than that of incandescent lamps ($12\,\mathrm{lm\,W^{-1}}$) or compact fluorescent lamps ($80\,\mathrm{lm\,W^{-1}}$) [9].

In a study by Tsao and Waide [10], it was found that lighting accounted for 6.5 % of global energy consumption in 2005. In the 2016 Annual Energy Outlook produced by the United States Energy Information Administration [11], it was predicted that the average United States household electricity consumption for lighting will decrease by 62 % by 2040 thanks to the improved efficiency of domestic lighting based on LEDs compared with incandescent bulbs or compact fluorescent lamps. This has benefits both in terms of cost to the consumer and a reduction in greenhouse gas emissions [12]. Portable LED lanterns with long battery lives have also had a positive impact on rural communities where mains electricity is unavailable, where previously fuel-burning lamps were used which produce emissions that are harmful if breathed in [13].

The output of LEDs can be switched at a rate that is faster than can be perceived by the human eye. This has led to investigations into their potential for visible light communication (VLC), where data is encoded in the modulated switching rate [14, 15]. With an appropriate detector, wireless data transfer can be achieved using the LEDs that illuminate a room. This type of network could reduce demand on the radio spectrum as it would be localised to one particular room since the visible light would not be transmitted through walls or partitions [15].

The bandgaps of GaN and AlN lie within the UV region of the electromagnetic spectrum, and this has been exploited in the production of UV LEDs. The use of these has been demonstrated in sterilisation through UV illumination of micro-organisms [16, 17]. An efficient UV light source, provided by LEDs, would have applications in water purification in rural areas where low-pressure mercury lamps are impractical due to the short lifetime of the lamp and the production of mercury waste [16].

The first blue semiconductor laser diode based on an $In_{0.2}Ga_{0.8}N/In_{0.05}Ga_{0.95}N$ multiple quantum well (MQW) structure was demonstrated by Nakamura *et al.* [18] in 1996. Group III-nitride-based blue and violet laser diodes have since enabled high density optical data storage as the minimum spot size of the focused beam is directly proportional to the wavelength of the radiation, meaning that a higher track density can be read by a shorter wavelength laser [19]. So-called Blu-ray discs have a capacity of 25 GB, compared to 4.7 GB for digital versatile discs (which are read by a red laser) and 780 MB for compact discs (read by an infrared laser) [20].

1.2 A Brief History of the Blue Light Emitting Diode

The impact of the blue LED on lighting technology cannot be understated. In 1963, a year after inventing the first device based on a semiconductor *p-n* junction that emitted visible light, in this case red light [21], Nick Holonyak Jr. was quoted as saying that he and his research group believed that semiconductor LEDs or lasers would soon lead to an efficient and practical white light source that would replace incandescent lamps [22]. However, while the continued development and improvement of the red LED that occurred over subsequent years rapidly led to highly efficient devices made from the group III-phosphide family of materials [2, 7, 22, 23], efficient light emission from materials with larger bandgaps proved much more difficult to achieve.

The first LED based on GaN was produced by Pankove *et al.* [24]. The GaN was unintentionally *n*-type, and an insulating layer of GaN was produced by doping it with Zn (an acceptor in GaN) to compensate the large electron population. The Zn-doped material was grown on top of the unintentionally doped material and blue luminescence was produced when a bias was applied due to radiative recombination from *i*-*n* transitions occurring at the interface between these two layers [25]. An LED emitting violet light was produced by Maruska *et al.* [26] using a similar structure but with Mg as the dopant instead of Zn.

Early GaN-based LEDs suffered from poor crystalline quality due to the lattice mismatch between GaN and sapphire, the most commonly used substrate. It was demonstrated by Yoshida *et al.* [27] that cathodoluminescence (CL) peaks with increased intensity were produced from GaN thin films grown by molecular beam epitaxy (MBE) with an AlN buffer layer between the sapphire substrate and the GaN layer. Since the lattices of GaN and AlN match much better than GaN and sapphire, the improvements were attributed to the improved crystalline quality of the GaN grown on the AlN buffer layer compared with GaN grown directly on sapphire. Amano *et al.* [28] later reported on the growth of GaN thin films with no cracks using an AlN buffer layer in metalorganic vapour phase epitaxy (MOVPE) growth. The improvements reported by Amano *et al.* [28] were equalled by Nakamura [29] a few years later using a GaN buffer layer, grown at a lower temperature than the top layer of GaN, instead of an AlN buffer layer.

Because successful *p*-type conductivity in GaN had not yet been achieved, the LEDs produced by Pankove *et al.* [24, 25] and Maruska *et al.* [26] were based on metal-insulator-semiconductor structures (the acceptors that had been used as dopants were to compensate the unintentional *n*-type conductivity). Amano *et al.* [30] and Nakamura *et al.* [31] reported on the increased photoluminescence (PL) intensity of GaN films doped with Mg following low energy electron beam irradiation (LEEBI). Nakamura *et al.* [31] also reported an improved hole mobility for the films in Hall-effect

measurements following LEEBI. It was suggested by Van Vechten *et al.* [32] that H^+ ions compensate the acceptor dopant impurities, and that the electrons introduced by LEEBI neutralise these ions. Some of the resultant H atoms then diffuse to the surface of the lattice and combine with another H atom to leave the material as gas molecules. Performing LEEBI for sufficiently long times allows enough ions to be neutralised and to reach the surface that the uncompensated acceptors left behind give a measurably increased hole conductivity. Nakamura *et al.* [33] later showed that thermal annealing of GaN films doped with Mg in a N_2 atmosphere at temperatures above 700 °C led to a reduction in the resistivity of the films by a factor of 10^5. The authors concluded that the neutral acceptor-H complexes formed by compensation are dissociated by the annealing process. The first GaN LED based on a *p*-*n* junction was produced by Amano *et al.* [34], where the *p*-type layer was produced from a Mg doped GaN film grown by MOVPE and then treated with the LEEBI technique. This LED emitted UV light and was shown to be significantly brighter than the metal-insulator-semiconductor devices grown before.

Following the successful production of high crystalline quality GaN, along with *p*-type GaN, progress accelerated. In 1994, Nakamura *et al.* [35] produced an LED consisting of an InGaN:Zn/AlGaN:Mg double heterostructure. An EQE of 2.7 % and a luminous intensity of over 1 cd, the highest ever for a blue LED at the time, were reported. The following year, Nakamura *et al.* [3] reported on the production of blue and violet LEDs based on InGaN/GaN single QWs with EQEs of 8.7 % and 9.2 %, respectively. These were the highest EQEs ever reported for LEDs emitting in these spectral regions. Since then, development of III-nitride LEDs has focused on QW-based designs and it is these, in combination with a yellow phosphor, on which commercial white LEDs are based [2, 4]. In 2014, the Nobel Prize in Physics was awarded jointly to Isamu Akasaki, Hiroshi Amano and Shuji Nakamura "for the invention of efficient blue light-emitting diodes which has enabled bright and energy-saving white light sources" [36], in recognition of the importance of their work.

While the blue LED has now achieved ubiquity in many domestic, commercial, and public lighting applications, there remain several unsolved problems. Among these is the hotly debated efficiency droop [5, 37, 38], discussed in more detail in Chapter 6, where the emission intensity of LEDs increases sublinearly with drive current at high current densities. Another major issue is the dramatically lower efficiencies of structures designed to emit green light compared with blue, the so-called "green gap" [7]. This creates a barrier to more efficient red-green-blue (RGB) lighting, where the need for the yellow phosphor (in which some energy is lost in the conversion from blue to yellow light) is removed. Solutions to these problems, for which several causes and remedies have been proposed, will require a deep understanding of the fundamental physics of the group III-nitrides. Therefore, the study of this materials system remains a highly active field of research.

1.3 Thesis Outline

In Chapter 2 of this thesis, some of the fundamental properties of the group III-nitrides are discussed. Particular attention is paid to the effects of strain between epitaxial layers of different alloy compositions on QWs, as well as the phenomenon of carrier localisation in QWs. The growth techniques that were used to produce the samples studied in this work are also outlined.

In Chapter 3, the experimental techniques that were employed in this work are detailed. These include PL spectroscopy, time-correlated single photon counting (TCSPC) and time-resolved photoluminescence (TRPL) spectroscopy.

In Chapter 4, the effects of a Si-doped InGaN underlayer (UL) on MQW structures with different numbers of QWs are presented and discussed. The inclusion of an UL has been shown to lead to efficiency improvements in LEDs and in optical experiments on QW structures, at least partly due to compensation of the strain-induced electric fields across the QWs. This occurs through manipulation of the surface polarisation

field that is present across the whole structure and which acts in the opposite sense to the strain-induced fields. Increasing the number of QWs in a structure has also been shown to lead to efficiency improvements, possibly due to the recapturing of carriers that are lost from QWs due to thermionic emission. The competition between these effects is investigated and discussed.

In Chapter 5, the effects of single QW structures containing ULs and with varying cap layer thickness are investigated. It is expected that varying the total distance between the UL and the sample surface leads to a variation in the net electric field across the QW. The electric fields across QWs have been shown to play an important role in the localisation of electrons at low temperatures, and the effects of varying the net electric field on the optical properties of single QWs are discussed in light of this.

In Chapter 6, investigations into an emission band that occurs on the high energy side of the QW emission peak at high excited carrier densities are presented and discussed. Similar emission features have been reported by other research groups, but no consensus exists as to the origin of this emission feature. The emission band occurs at excited carrier densities where the sample is observed to undergo efficiency droop. Therefore, a summary of the proposed mechanisms for the efficiency droop is presented along with reports of the observation of the high energy emission band where its origin has been associated with a particular droop mechanism. Time-integrated and time-resolved PL spectroscopic studies on 3 single QW structures with different QW In composition fractions are then presented. In particular, the form of the PL time decay curves is studied as a function of detection energy across the emission band. These results are compared to decays that have been observed in self-assembled quantum dots (QDs).

In Chapter 7, recommendations for further work are made.

1.4 References

[1] I. Vurgaftman and J. R. Meyer. "Band parameters for nitrogen-containing semiconductors". *Journal of Applied Physics* **94**, 6 (2003), 3675. DOI: 10.1063/1.1600519 (Cited on page 16).

[2] S. Nakamura. "Nobel Lecture: Background story of the invention of efficient blue InGaN light emitting diodes". *Reviews of Modern Physics* **87**, 4 (2015), 1139. DOI: 10.1103/RevModPhys.87.1139 (Cited on pages 17, 18, 20).

[3] S. Nakamura *et al.* "High-power InGaN single-quantum-well-structure blue and violet light-emitting diodes". *Applied Physics Letters* **67**, 13 (1995), 1868. DOI: 10.1063/1.114359 (Cited on pages 17, 20).

[4] Y. Narukawa. "White-Light LEDS". *Optics and Photonics News* **15**, 4 (2004), 24. DOI: 10.1364/OPN.15.4.000024 (Cited on pages 17, 20).

[5] C. Weisbuch *et al.* "The efficiency challenge of nitride light-emitting diodes for lighting". *physica status solidi (a)* **212**, 5 (2015), 899. DOI: 10.1002/pssa.201431868 (Cited on pages 17, 21).

[6] T. Sano *et al.* "High Internal Quantum Efficiency Blue-Green Light-Emitting Diode with Small Efficiency Droop Fabricated on Low Dislocation Density GaN Substrate". *Japanese Journal of Applied Physics* **52**, 8S (2013), 08JK09. DOI: 10.7567/JJAP.52.08JK09 (Cited on page 17).

[7] M. Auf der Maur *et al.* "Efficiency Drop in Green InGaN/GaN Light Emitting Diodes: The Role of Random Alloy Fluctuations". *Physical Review Letters* **116**, 2 (2016), 027401. DOI: 10.1103/PhysRevLett.116.027401 (Cited on pages 17, 18, 21).

[8] P. Pust *et al.* "A revolution in lighting". *Nature Materials* **14**, 5 (2015), 454. DOI: 10.1038/nmat4270 (Cited on page 17).

[9] P. Von Dollen *et al.* "Let There Be Light-With Gallium Nitride: The 2014 Nobel Prize in Physics". *Angewandte Chemie International Edition* **53**, 51 (2014), 13978. DOI: 10.1002/anie.201410693 (Cited on page 17).

[10] J. Y. Tsao and P. Waide. "The world's appetite for light: Empirical data and trends spanning three centuries and six continents". *LEUKOS* **6**, 4 (2010), 259. DOI: 10.1582/LEUKOS.2010.06.04001 (Cited on page 17).

[11] U.S. Energy Information Administration. *Annual Energy Outlook 2016*. 2016. URL: https://www.eia.gov/outlooks/aeo/pdf/0383(2016).pdf (visited on 11/22/2018) (Cited on page 17).

[12] L. Liu *et al.* "Replacement policy of residential lighting optimized for cost, energy, and greenhouse gas emissions". *Environmental Research Letters* **12**, 11 (2017), 114034. DOI: 10.1088/1748-9326/aa9447 (Cited on page 17).

[13] G. Bensch *et al.* "The lighting transition in rural Africa - From kerosene to battery-powered LED and the emerging disposal problem". *Energy for Sustainable Development* **39** (2017), 13. DOI: 10.1016/j.esd.2017.03.004 (Cited on page 17).

[14] P. H. Pathak *et al.* "Visible Light Communication, Networking, and Sensing: A Survey, Potential and Challenges". *IEEE Communications Surveys & Tutorials* **17**, 4 (2015), 2047. DOI: 10.1109/COMST.2015.2476474 (Cited on page 17).

[15] S. Zhang *et al.* "1.5 Gbit/s Multi-Channel Visible Light Communications Using CMOS-Controlled GaN-Based LEDs". *Journal of Lightwave Technology* **31**, 8 (2013), 1211. DOI: 10.1109/JLT.2013.2246138 (Cited on page 17).

[16] A. Hamamoto *et al.* "New water disinfection system using UVA light-emitting diodes". *Journal of Applied Microbiology* **103**, 6 (2007), 2291. DOI: 10.1111/j.1365-2672.2007.03464.x (Cited on page 18).

[17] J. Li *et al.* "Enhanced germicidal effects of pulsed UV-LED irradiation on biofilms". *Journal of Applied Microbiology* **109**, 6 (2010), 2183. DOI: 10.1111/j.1365-2672.2010.04850.x (Cited on page 18).

[18] S. Nakamura *et al.* "Room-temperature continuous-wave operation of InGaN multi-quantum-well structure laser diodes". *Applied Physics Letters* **69**, 26 (1996), 4056. DOI: 10.1063/1.117816 (Cited on page 18).

[19] I. Ichimura *et al.* "Optical Disk Recording Using a GaN Blue-Violet Laser Diode". *Japanese Journal of Applied Physics* **39**, Part 1, No. 2B (2000), 937. DOI: 10.1143/JJAP.39.937 (Cited on page 18).

[20] Blu-ray Disc Association. *White paper Blu-ray Disc (TM) format.* 2012. URL: http://blu-raydisc.com/Assets/Downloadablefile/White_Paper_General_4th_20150817_clean.pdf (visited on 11/22/2018) (Cited on page 18).

[21] N. Holonyak and S. F. Bevacqua. "Coherent (visible) light emission from GaAsP junctions". *Applied Physics Letters* **1**, 4 (1962), 82. DOI: 10.1063/1.1753706 (Cited on page 18).

[22] T. Palucka. "50 years ago: How Holonyak won the race to invent visible LEDs". *MRS Bulletin* **37**, 10 (2012), 963. DOI: 10.1557/mrs.2012.262 (Cited on page 18).

[23] G. Stringfellow. "Materials Issues in High-Brightness Light-Emitting Diodes". *High-Brightness Light-Emitting Diodes*. Ed. by G. Stringfellow and M. G. Craford. Academic Press, 1997. DOI: 10.1016/S0080-8784(08)62402-3 (Cited on page 18).

[24] J. Pankove *et al.* "GaN blue light-emitting diodes". *Journal of Luminescence* **5**, 1 (1972), 84. DOI: 10.1016/0022-2313(72)90038-5 (Cited on page 19).

[25] J. Pankove *et al.* "Electroluminescence in GaN". *Journal of Luminescence* **4**, 1 (1971), 63. DOI: 10.1016/0022-2313(71)90009-3 (Cited on page 19).

[26] H. Maruska *et al.* "Preparation of Mg-doped GaN diodes exhibiting violet electroluminescence". *Materials Research Bulletin* **7**, 8 (1972), 777. DOI: 10.1016/0025-5408(72)90127-4 (Cited on page 19).

[27] S. Yoshida *et al.* "Improvements on the electrical and luminescent properties of reactive molecular beam epitaxially grown GaN films by using AlN-coated sapphire substrates". *Applied Physics Letters* **42**, 5 (1983), 427. DOI: 10.1063/1.93952 (Cited on page 19).

[28] H. Amano *et al.* "Metalorganic vapor phase epitaxial growth of a high quality GaN film using an AlN buffer layer". *Applied Physics Letters* **48**, 5 (1986), 353. DOI: 10.1063/1.96549 (Cited on page 19).

[29] S. Nakamura. "GaN Growth Using GaN Buffer Layer". *Japanese Journal of Applied Physics* **30**, Part 2, No. 10A (1991), L1705. DOI: 10.1143/JJAP.30.L1705 (Cited on page 19).

[30] H. Amano *et al.* "Electron beam effects on blue luminescence of zinc-doped GaN". *Journal of Luminescence* **40-41**, C (1988), 121. DOI: 10.1016/0022-2313(88)90117-2 (Cited on page 19).

[31] S. Nakamura *et al.* "Highly P-Typed Mg-Doped GaN Films Grown with GaN Buffer Layers". *Japanese Journal of Applied Physics* **30**, Part 2, No. 10A (1991), L1708. DOI: 10.1143/JJAP.30.L1708 (Cited on page 19).

[32] J. A. Van Vechten *et al.* "Defeating Compensation in Wide Gap Semiconductors by Growing in H that is Removed by Low Temperature De-Ionizing Radiation". *Japanese Journal of Applied Physics* **31**, Part 1, No. 11 (1992), 3662. DOI: 10.1143/JJAP.31.3662 (Cited on page 20).

[33] S. Nakamura *et al.* "Hole Compensation Mechanism of P-Type GaN Films". *Japanese Journal of Applied Physics* **31**, Part 1, No. 5A (1992), 1258. DOI: 10.1143/JJAP.31.1258 (Cited on page 20).

[34] H. Amano *et al.* "P-Type Conduction in Mg-Doped GaN Treated with Low-Energy Electron Beam Irradiation (LEEBI)". *Japanese Journal of Applied Physics* **28**, Part 2, No. 12 (1989), L2112. DOI: 10.1143/JJAP.28.L2112 (Cited on page 20).

[35] S. Nakamura *et al.* "Candela-class high-brightness InGaN/AlGaN double heterostructure blue-light-emitting diodes". *Applied Physics Letters* **64**, 13 (1994), 1687. DOI: 10.1063/1.111832 (Cited on page 20).

[36] *The 2014 Nobel Prize in Physics - Press Release*. 2014. URL: https://www.nobelprize.org/nobel_prizes/physics/laureates/2014/press.html (visited on 11/09/2017) (Cited on page 20).

[37] G. Verzellesi *et al.* "Efficiency droop in InGaN/GaN blue light-emitting diodes: Physical mechanisms and remedies". *Journal of Applied Physics* **114**, 7 (2013), 071101. DOI: 10.1063/1.4816434 (Cited on page 21).

[38] L. Wang *et al.* "A Review on Experimental Measurements for Understanding Efficiency Droop in InGaN-Based Light-Emitting Diodes". *Materials* **10**, 11 (2017), 1233. DOI: 10.3390/ma10111233 (Cited on page 21).

Chapter 2

Properties of InGaN/GaN Quantum Wells

2.1 Basic Properties of Group III-Nitride Semiconductors

Group III-nitride semiconductors can exist in either the wurtzite or zincblende crystal phase. The structures studied in this work were all grown in the wurtzite crystal phase along the [0 0 0 1] direction, where group III and N atoms are arranged in alternating hexagonal layers. The spacing between adjacent atoms in the hexagonal layers is defined by the lattice constant, a, and the spacing between the hexagonal planes is defined by a different lattice constant, c. The [0 0 0 1] growth direction is therefore referred to as the "c" direction and material grown this way is referred to as "c-plane" material, where the c-plane is the atomic plane perpendicular to the c axis.

The high cost of native group III-nitride substrates has led to sapphire (Al_2O_3) becoming the most common substrate material used for growing c-plane structures, including commercial LEDs [1]. The a lattice parameter for sapphire, $a_{Al_2O_3}$, is 4.76 Å [2]. This is 50 % larger than that of GaN (the a and c lattice parameters of GaN,

AlN and InN are listed in Table 2.1 [3]). Therefore, the group III-nitride crystal structure rotates by 30° with respect to the sapphire substrate. Atoms in adjacent group III-nitride unit cells then have a spacing of $\sqrt{3}a_{\text{III-N}}$, where $a_{\text{III-N}}$ is the a lattice parameter for the group III-nitride material, which is closer to $a_{\text{Al}_2\text{O}_3}$ and so leads to a reduced lattice mismatch. This is illustrated schematically in Figure 2.1.

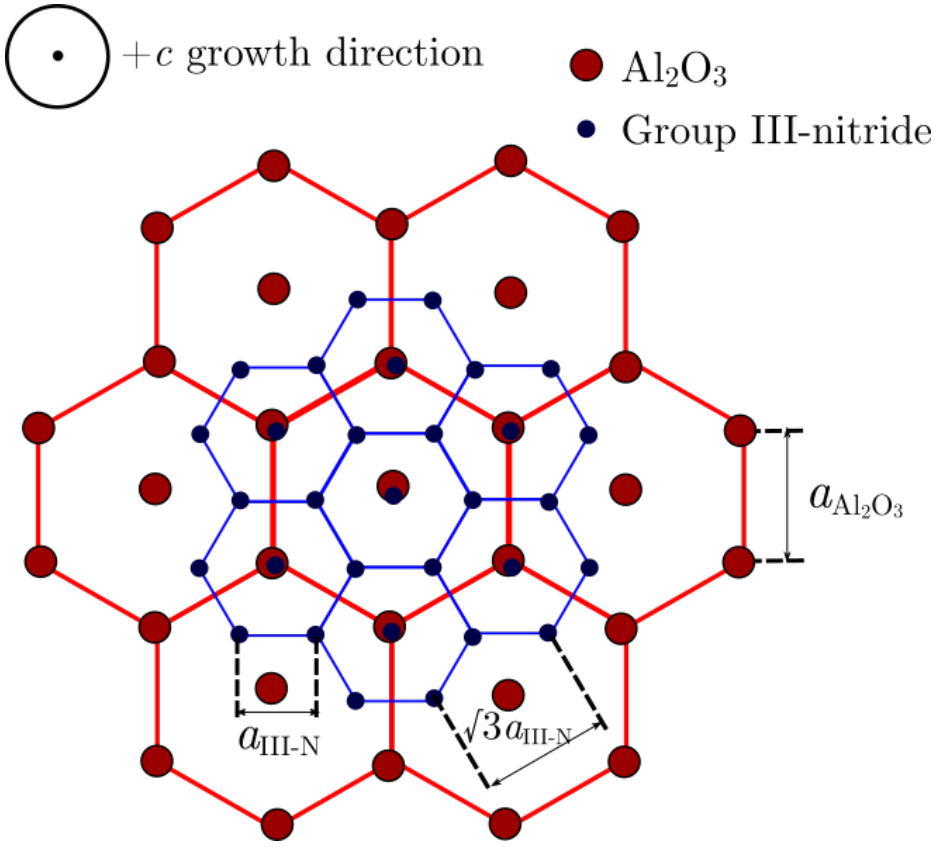

Figure 2.1: Schematic diagram showing the rotated wurtzite group III-nitride crystal structure grown on sapphire (Al_2O_3). $a_{\text{Al}_2\text{O}_3}$ and $a_{\text{III-N}}$ are the a lattice parameters of sapphire and the group III-nitride material, respectively.

Table 2.1: Summary of some crystal parameters for GaN, AlN and InN from Vurgaftman and Meyer [3].

Parameter	GaN	AlN	InN
Lattice constant, a (Å)	3.189	3.112	3.545
Lattice constant, c (Å)	5.703	5.185	4.982
Bandgap at 0 K, $E_G(0)$ (eV)	3.510	6.25	0.78
Varshni parameter, α (meV K^{-1})	0.909	1.799	0.245
Varshni parameter, β (K)	830	1462	624

The residual strain in the group III-nitride layers, following the rotation of the crystal lattice described above, is relieved by the formation of threading dislocations. These are crystal defects which originate at the interface between the group III-nitride material and the substrate, and which propagate to the surface of the structure [4, 5]. Threading dislocation densities as high as $\sim 10^{10}\,\mathrm{cm}^{-2}$ have been measured in group III-nitride structures grown on sapphire [4–6] as a result of the strain relaxation that occurs. However, while the efficiencies of LEDs based on group III-phosphide and group III-arsenide structures have been shown to decrease rapidly when the threading dislocation density is greater than $\sim 10^{4}\,\mathrm{cm}^{-2}$ [7, 8], the efficiencies of InGaN/GaN QWs and LEDs have been found to be much less sensitive to these threading dislocation densities [4, 9–11]. The quenching of luminescence by threading dislocations occurs because they act as non-radiative recombination centres. It is therefore widely believed that the insensitivity of InGaN/GaN QW structures to threading dislocations is due to the localisation of carriers at potential minima, preventing their diffusion towards these defects. This is explained in more detail in Section 2.5.

The bandgaps, E_G, of GaN, AlN and InN at temperature, $T = 0\,\mathrm{K}$, are listed in Table 2.1 [3]. The dependence of E_G on T can be described using the empirically-derived Varshni formula [12],

$$E_G(T) = E_G(0) - \frac{\alpha T^2}{\beta + T}, \tag{2.1}$$

where α and β are the Varshni parameters. The values of α and β for GaN, AlN and InN are also listed in Table 2.1 [3].

The ability to tune a light emitting device to a particular emission energy is achieved using alloys of materials with different bandgap energies with carefully chosen compositions. The a lattice constant for a ternary group III-nitride alloy, a_{12}, can be calculated by a linear interpolation of the values for the two materials, 1 and 2, from which it is composed (referred to as Vergard's rule) [13],

$$a_{12} = xa_1 + (1 - x)a_2, \tag{2.2}$$

where a_1 and a_2 are the values of a for materials 1 and 2, respectively, and x is the alloy composition fraction of material 1. The alloy composition dependent bandgap for a ternary alloy of materials 1 and 2, E_{G12}, follows the bowed Vergard rule,

$$E_{G12} = xE_{G1} + (1 - x)E_{G2} - x(1 - x)b_{12}, \tag{2.3}$$

where b_{12} is the quadratic bowing parameter between materials 1 and 2 [13]. The values of b_{12} for InGaN, AlGaN and AlInN have been determined as 1.4 eV [3] 0.7 eV [3] and 3.0 eV [14, 15], respectively. E_G is shown varying with a while x is varied continuously from 0–1 between the different group III-nitride materials in Figure 2.2.

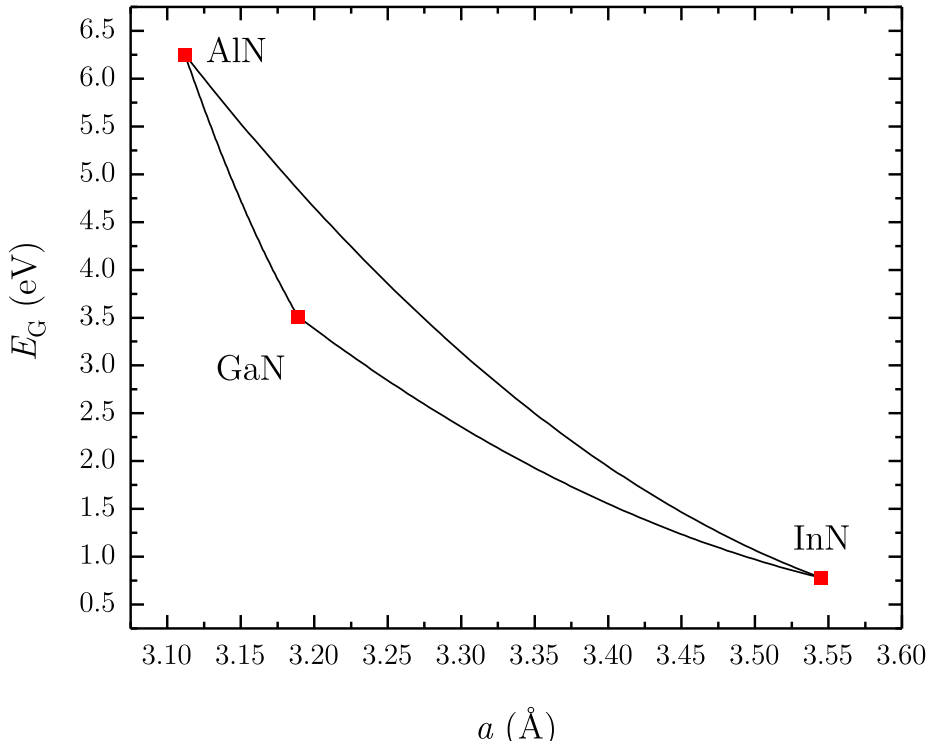

Figure 2.2: Variation of bandgap, E_G, with lattice parameter, a, for GaN, AlN and InN and ternary alloys, calculated using bowing parameters taken from Vurgaftman and Meyer [3] for InGaN and AlGaN and Wu *et al.* [14, 15] for AlInN.

2.2 Polarisation

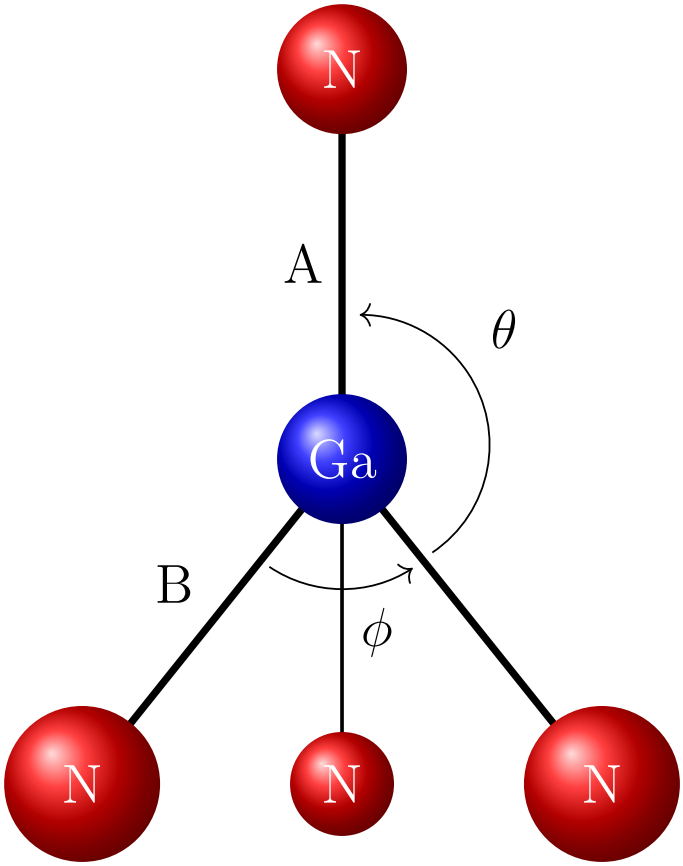

Figure 2.3: Schematic diagram showing a Ga atom (blue sphere) surrounded by a tetrahedron of N atoms (red spheres). The atomic bonds, A and B, and the angles between them, θ and ϕ, are as described in the text.

Wurtzite group-III nitride crystals exhibit both spontaneous and piezoelectric polarisations. Group III atoms, represented by a Ga atom in Figure 2.3, are surrounded by a tetrahedron of N atoms. Each atomic bond has an associated polarisation. The bond between the group III atom and the N atom at the apex of the tetrahedron is labelled as A, while the bonds between the bottom three N atoms and the group III atom are each labelled as B. The angle between A and any B is labelled as θ, and the angle between any two B is labelled as ϕ. Under no strain, the lengths of A and B as well as angles θ and ϕ are not equal. This results in a residual polarisation, referred to as the spontaneous polarisation, P^{sp}, because the sum of the polarisations is non-zero. The values of P^{sp} for GaN, AlN and InN [3] are listed in Table 2.2. The

spontaneous polarisation for a ternary alloy, P_{12}^{sp}, composed of materials 1 and 2 with respective polarisations P_1^{sp} and P_2^{sp}, is calculated using a bowed Vergard rule [13],

$$P_{12}^{\mathrm{sp}} = xP_1^{\mathrm{sp}} + (1-x)P_2^{\mathrm{sp}} - x(1-x)b_{12}^{\mathrm{sp}}, \tag{2.4}$$

where x is again the alloy composition fraction of material 1 and b_{12}^{sp} is a bowing parameter. The values of b_{12}^{sp} have been determined as $-0.037\,\mathrm{C\,m^{-2}}$, $-0.021\,\mathrm{C\,m^{-2}}$ and $-0.070\,\mathrm{C\,m^{-2}}$ for InGaN, AlGaN and AlInN, respectively [3].

Table 2.2: Summary of the spontaneous polarisations [3], piezoelectric constants [16] and elastic constants [3] for GaN, AlN and InN.

Parameter	GaN	AlN	InN
P^{sp} ($\mathrm{C\,m^{-2}}$)	−0.034	−0.090	−0.042
e_{31} ($\mathrm{C\,m^{-2}}$)	−0.34	−0.53	−0.41
e_{33} ($\mathrm{C\,m^{-2}}$)	0.67	1.50	0.81
C_{13} (GPa)	106	108	92
C_{33} (GPa)	398	373	224

For InGaN/GaN QW structures, such as those studied in this work, the larger a lattice parameter for InGaN compared to GaN results in compressive strain of the InGaN. This modifies the angles θ and ϕ, shown in Figure 2.3, resulting in what is referred to as the piezoelectric polarisation, $\mathbf{P}^{\mathrm{pz}}$. This is calculated as the product of the piezoelectric constants tensor, $\bar{\bar{e}}$, and the strain field tensor, $\vec{\boldsymbol{\epsilon}}$ [17],

$$\mathbf{P}^{\mathrm{pz}} = \bar{\bar{e}} \cdot \vec{\boldsymbol{\epsilon}}. \tag{2.5}$$

In a QW grown along the [0 0 0 1] crystallographic axis, referred to here as the z axis, it is assumed that the components of strain orthogonal to z (x and y) are equal [18]. The expression for the piezoelectric polarisation then reduces to [19]

$$P^{\mathrm{pz}} = 2e_{31}\epsilon_{xx} + e_{33}\epsilon_{zz}, \tag{2.6}$$

where ϵ_{xx} is the in-plane strain at the QW/barrier interface and ϵ_{zz} is the strain in the growth direction. The values of the piezoelectric constants, e_{31} and e_{33}, are listed for GaN, InN and AlN [16] in Table 2.2. For layers grown pseudomorphically, as is the case for InGaN QW layers grown with GaN barriers, ϵ_{xx} is given by [18, 19]

$$\epsilon_{xx} = \frac{a_{\mathrm{b}} - a_{\mathrm{QW}}}{a_{\mathrm{QW}}}, \tag{2.7}$$

where a_{b} and a_{QW} are the a lattice parameters for the barrier and QW materials, respectively. ϵ_{zz} can be written in terms of ϵ_{xx} as [19]

$$\epsilon_{zz} = -2\epsilon_{xx}\frac{C_{13}}{C_{33}}, \tag{2.8}$$

where C_{13} and C_{33} are the elastic constants for the material, listed for GaN, AlN and InN in table 2.2 [3]. The values of the elastic and piezoelectric constants for ternary alloys can be calculated from a linear interpolation of those for the binary compounds [3].

It was later shown by Bernardini and Fiorentini [13] that the piezoelectric polarisations for AlN, GaN and InN (P^{pz}_{AlN}, P^{pz}_{GaN} and P^{pz}_{InN}, respectively) vary non-linearly with ϵ_{xx} as

$$P^{pz}_{GaN} = -0.918\epsilon_{xx} + 9.514\epsilon^2_{xx}, \tag{2.9}$$

$$P^{pz}_{AlN} = -1.808\epsilon_{xx} + 5.624\epsilon^2_{xx} \quad \text{for} \quad \epsilon_{xx} < 0, \tag{2.10}$$

$$P^{pz}_{AlN} = -1.808\epsilon_{xx} - 7.888\epsilon^2_{xx} \quad \text{for} \quad \epsilon_{xx} > 0, \tag{2.11}$$

and

$$P^{pz}_{InN} = -1.373\epsilon_{xx} + 7.559\epsilon^2_{xx}. \tag{2.12}$$

Discontinuities in the spontaneous and piezoelectric polarisations at the interfaces

between layers of QW and barrier material result in the accumulation of electric charge at these interfaces. Assuming that the barriers are identical, the total electric field across a QW, F_{QW}, is calculated by [18]

$$F_{\mathrm{QW}} = \frac{(P_{\mathrm{b}}^{\mathrm{total}} - P_{\mathrm{QW}}^{\mathrm{total}})d_{\mathrm{b}}}{\varepsilon_0(\varepsilon_{\mathrm{QW}}d_{\mathrm{QW}} + \varepsilon_{\mathrm{b}}d_{\mathrm{b}})}, \tag{2.13}$$

where $P_{\mathrm{QW}}^{\mathrm{total}}$ and $P_{\mathrm{b}}^{\mathrm{total}}$ are the sums of the spontaneous and piezoelectric polarisations for the QW and barrier materials, respectively, d_{QW} and d_{b} are the respective thicknesses of the well and barrier materials, $\varepsilon_{\mathrm{QW}}$ and ε_{d} are the respective permittivities and ε_0 is the permittivity of free space. The potential drop across the QW due to the electric field, E_{PD}, is given by

$$E_{\mathrm{PD}} = F_{\mathrm{QW}}d_{\mathrm{QW}}. \tag{2.14}$$

In wurtzite group III-nitride structures grown by MOVPE, the electric field across the QW due to the spontaneous polarisation is in the opposite sense to that due to the piezoelectric polarisation, but the piezoelectric polarisation dominates in InGaN/GaN QWs [17]. However, through manipulation of the magnitudes of the two types of polarisation, the net electric field across a QW can be controlled. This is explored in more detail in Chapters 4 and 5.

2.3 Quantum Confined Stark Effect

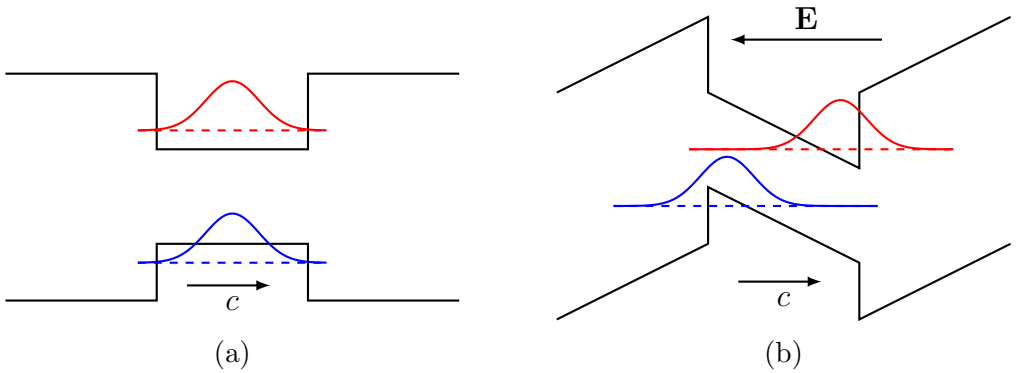

Figure 2.4: Schematic illustration of the process that causes QCSE. In (a), a square QW with zero net electric field across it is shown. In (b), the case where the net electric field across the QW, **E**, is non-zero is shown. The electron and hole $n = 1$ wavefunctions are shown in red and blue, respectively. Arrows indicate the c growth direction.

A non-zero net electric field across a QW leads to a separation of the electron and hole wavefunctions in the growth direction as they are attracted to opposite QW/barrier interfaces by opposing sheet charges. This separation reduces the overlap of the electron and hole wavefunctions and so increases the electron-hole radiative recombination lifetime. The potential drop across the QW means that the electron and hole $n = 1$ wavefunctions are confined at lower energies by a triangular potential well, leading to a reduced energy difference between the lowest confined electron and hole states relative to the case of an ideal square QW. This was observed in experiments performed by Miller *et al.* [20], who reported a decreasing excitonic peak energy in absorption spectra of a GaAs/AlGaAs MQW structure with increasing strength of an electric field applied parallel to the growth axis. This energy shift is referred to as the quantum confined Stark effect (QCSE) [21], and is illustrated schematically in Figure 2.4.

The large net electric fields across InGaN QWs with GaN barriers, caused by the large piezoelectric polarisations at the QW/barrier interfaces, mean that the QCSE and the associated phenomena play a significant role in the optical properties of these

structures [17, 22, 23]. They have been identified as a contributing factor to the so-called "green gap" problem [24, 25], as the piezoelectric polarisation of InGaN layers increases with increasing In fraction due to the increasing lattice mismatch between the QW and barrier layers. As higher In fractions are required for green light emission compared to blue, the increased spatial separations of the electron and hole wavefunctions in green-emitting QWs lead to longer radiative recombination lifetimes, making non-radiative recombination processes more competitive.

2.4 Growth Techniques

Several techniques have been employed in growing group III-nitride structures, including MBE [26], hydride vapour phase epitaxy [27] and MOVPE [28, 29]. The QW structures studied in the work described in this thesis were all grown on sapphire by MOVPE in a Thomas Swan closed coupled shower head reactor by colleagues at the Department of Materials Science and Metallurgy, University of Cambridge. Trimethylindium, trymethylgallium and ammonia (NH_3) were used as the sources of In, Ga and N, respectively. The different QW In fractions were achieved by varying the growth temperature of the InGaN, as lower temperatures result in a lower rate of In desorption and so a higher final QW In fraction [30, 31].

Three different growth methods were used in the production of the QW structures studied in this thesis: single-temperature (1T), two-temperature (2T) and quasi-two-temperature (Q2T). The effects of these different methods on the microstructural properties and the room temperature internal quantum efficiencies (IQEs) of 10-period InGaN/GaN QW structures were investigated by Oliver *et al.* [32]. In 1T growth, the InGaN QWs and the GaN barriers are grown at the same temperature. This means that the QW barrier is grown at a sub-optimal temperature, but that there is little interruption in the growth process between the growth of the different layers. In 2T growth, the temperature is ramped up over a period of 90 s between the growth of

the InGaN QW layer and the GaN barrier layer. During this period, the sample is held under ammonia but with no metal sources. The barrier growth temperature is then ramped up further during its growth. This means that the layers are grown mostly at their respective optimal temperatures, but In atoms are lost from the QW while the growth is interrupted. This has been shown to lead to gross QW width fluctuations, where the QW width is reduced to zero in some regions, leaving a GaN-filled gap and so resulting in discontinuities in the QWs [32, 33]. In Q2T growth, a GaN cap of thickness 1 nm is grown immediately after the QW and at the InGaN growth temperature. The rest of the barrier is then grown during a 90 s temperature ramp. This means that the loss of In atoms from the QW is prevented by the thin GaN cap layer, and the majority of the barrier layer is grown close to the optimal temperature.

Transmission electron microscopy (TEM) images showed that QWs grown by the 1T and Q2T methods exhibited well-defined and continuous QW layers (that is, no gaps), while gaps were observed in the QWs grown by the 2T method [32], consistent with the In desorption from the QWs described above. The room temperature IQEs were determined for the structures grown by the different methods from temperature dependent PL measurements. The lowest IQE was reported for the structure grown by the Q2T method and the highest for the 2T method [32]. It was suggested that the gaps in the QWs may act as potential barriers which would prevent carriers from reaching defects and so reduce the probability of non-radiative recombination in the 2T-grown structure. It was later demonstrated [34] that In atoms had been unintentionally incorporated into the QW barriers in all of the structures, with the In composition fraction exhibiting an exponential tail into the barrier following the growth of the InGaN QW layers. The characteristic length of this tail was reported to be 2.1 nm in the structure grown by the 1T method, but only 0.9 and 0.5 nm for the structures grown by the Q2T and 2T methods, respectively. In the case of the Q2T method, this length is similar to the 1 nm low temperature GaN cap layer that

was grown as part of this procedure. This was therefore attributed to the diffusion of In atoms into any barrier material that was grown at the InGaN growth temperature.

2.5 Carrier Localisation

Despite the large defect densities and the strong piezoelectric polarisation fields, LEDs based on InGaN/GaN QWs can exhibit room temperature IQEs above 90 % [35, 36]. It is now widely accepted that the reason for this is the localisation of carriers at potential minima within the QW [9, 10, 37–41].

2.5.1 Experimental Evidence of Carrier Localisation

Evidence for carrier localisation is provided in low temperature PL spectra of InGaN/GaN QWs by the large inhomogeneous broadening of the emission peaks that are observed from these structures [9, 37]. Peaks with full widths at half maximum (FWHMs) of several 10s to 100s of meV are typically reported for single QWs [9, 37, 42–46].

Further evidence of localisation is provided in temperature dependent PL spectroscopy, where a so-called S-shaped temperature dependence of the QW emission peak energy is often observed [38, 39, 47–50]. An example of this behaviour is shown in Figure 2.5. Rubel *et al.* [51, 52] proposed that this occurs due to the presence of a band tail of localised states, with the shift in emission energy caused by the thermal redistribution of carriers among localised states [38, 39, 47–51]. At low temperatures (0–10 K), carriers are randomly distributed among localised states. As the temperature is increased (between points A and B in Figure 2.5), carriers are thermally ejected from the shallow localised states and are then redistributed among lower energy, more deeply localised states. The shift in the distribution of occupied states to lower average energies leads to a red shift in the emission peak. The emission energy reaches a minimum, typically at temperatures around 50–100 K [38, 39, 47–

50], labelled in Figure 2.5 as B. As the temperature is increased further, carriers are thermally redistributed among higher energy, less deeply localised states. This causes the peak emission energy to blue shift until a local maximum is reached, labelled as C in Figure 2.5. The redistribution of carriers among still higher energy localised states continues as the temperature is increased above that at C up to room temperature, but the variation in the peak emission energy is now dominated by the shrinkage of the bandgap with temperature as described by Varshni [12] (Equation 2.1).

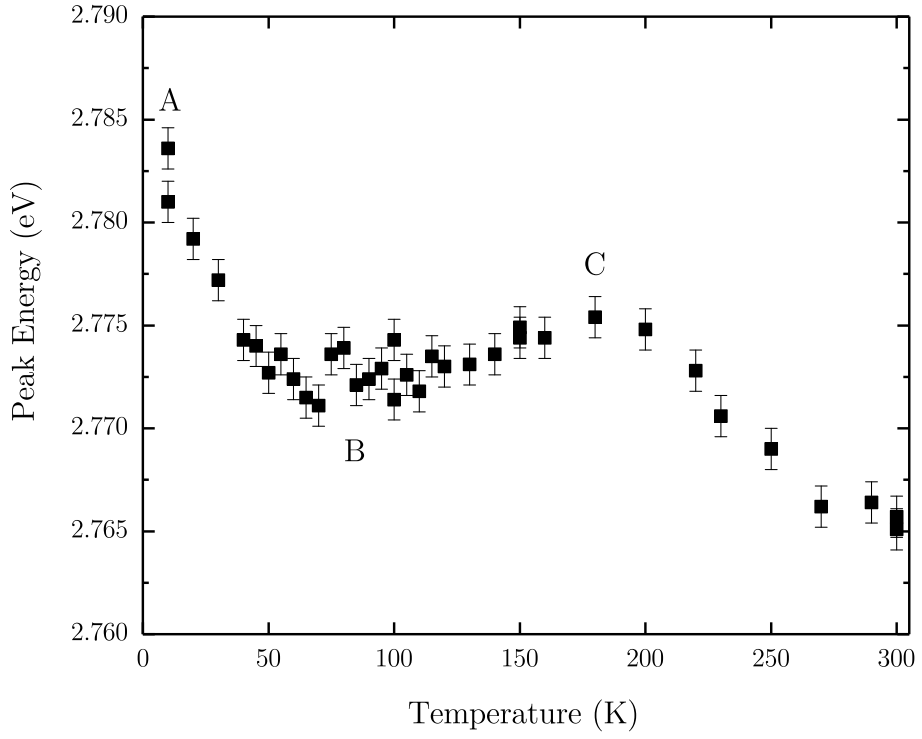

Figure 2.5: Example of the S-shaped temperature dependence of the InGaN/GaN QW emission peak energy. Points A, B and C are referred to in the text. The data shown is that of a single QW. Structural information for this sample (number C5978A) is given in Section 4.4 of Chapter 4.

In early studies [9, 53, 54], it was suggested that the spontaneous emission of light from InGaN/GaN QWs originates from the recombination of localised excitons. However, in later investigations, evidence was presented of separately localised electrons and holes at low temperatures, rather than excitons [55–58].

Kalliakos *et al.* [55] and Graham *et al.* [56] performed investigations into the

longitudinal optical (LO) phonon replica peaks that occur on the low energy side of InGaN/GaN QW emission spectra. A small dipole moment exists between a spatially separated electron and hole which leads to a local deformation of the crystal lattice. When the electron and hole recombine, the potential energy stored in the lattice by this deformation is released as an LO phonon [59]. The ratio of the peak intensities of successive LO phonon replicas is given by [60]

$$\frac{I_{n+1}}{I_n} = \frac{S}{n+1}, \quad n = 0, 1, 2, 3, ... \tag{2.15}$$

where I_0 is the peak intensity of the zero-phonon emission and S is the Huang-Rhys factor which describes the strength of the LO phonon interaction. Kalliakos *et al.* [55] investigated the variation in S for InGaN/GaN QWs with different QW widths. S was found to increase monotonically with increasing QW width. The authors were unable to find agreement between their experimental results and calculated S values for localised excitons. They therefore concluded that electrons and holes must be localised at opposite QW interfaces, with a minimum spatial separation imposed by the electric field parallel the growth axis. The subsequent recombination was described as analogous to donor-acceptor pair recombination. In later work by Graham *et al.* [56], low temperature PL spectra from InGaN/GaN QWs with varying QW In fractions were compared. The authors reported that S increases monotonically with In fraction and attributed this to an increasing electron-hole separation due to the increasing electric field strength across the QW as the piezoelectric polarisation becomes more pronounced. A minimum in-plane electron-hole separation was calculated to be approximately 2 nm. LO phonon replica peaks separated by energies close to 91 meV have been reported for InGaN/GaN QWs with a range of In composition fractions [56, 60, 61]. This compositional independence of the LO phonon energy has been attributed to the competing effects of the compositional and strain dependences of the LO phonon energy [62]. Pecharromán-Gallego *et al.* [60] argued that the zero-phonon

emission peak is due to recombination by a mixture of strongly and weakly localised carriers, while the LO phonon replica peaks are due to strongly localised carriers only, and that S can therefore only be accurately determined from the ratio between the first and second LO phonon peak intensities (or any other subsequent adjacent replica peaks).

Non-exponential PL decays are regularly observed in polar InGaN/GaN QWs at low temperatures [41, 56–58, 63, 64]. This was identified as further evidence of the donor-acceptor pair-like model for separately localised electrons and holes by Morel *et al.* [57, 58]. The authors attributed non-exponential PL decays from $In_{0.2}Ga_{0.8}N$/GaN QWs of different widths to electrons and holes localised respectively at opposite QW interfaces. The PL decay time was observed to increase with increasing QW width, attributed to the increasing separation of the electron and hole wavefunctions parallel to the growth direction. The shape of the decays was seen to be preserved when the decay time varied over 4 orders of magnitude by placing the decays on a reduced time scale, where the time scale was given in units of the measured PL decay time for a given decay. It was therefore concluded that the QWs had a particular "nanotexture" leading additionally to a separation of the electron and hole wavefunctions in the plane of the QW which is characterised by the shape of the PL decay.

2.5.2 Proposed Mechanisms for Carrier Localisation

Initial proposals for the localisation mechanism in InGaN/GaN QWs were potential minima caused by In-rich regions of the QW alloy material that were observed in transmission electron microscopy (TEM) images [53, 65, 66]. Some groups suggested that these In clusters should be treated as QDs [65, 67]. It was later shown by Smeeton *et al.* [68–70] and O'Neill *et al.* [71] that the In clusters that had been reported by other groups were in fact due to sample damage caused by the electron beams used to perform TEM measurements. In 3-dimensional atom probe tomography (APT)

measurements performed by Galtrey *et al.* [72], it was demonstrated that polar InGaN QWs exist as a random alloy.

It has been shown that carrier localisation can still occur in a random alloy. Wang [73] compared calculations of the electronic structure of an InN QD embedded in a GaN matrix with that of a random InGaN alloy (that is, no clustering of In atoms) for both wurtzite and zincblende crystal phases. For the random alloy in both crystal phases, it was found that holes are localised at In-N-In atomic chains. Fluctuations in the energies among the localised hole states were found to have a distribution of ∼100 meV, which accounts for the broad QW emission peaks observed for these structures.

Galtrey *et al.* [74] observed step changes in the QW/barrier interfaces of InGaN/GaN QWs with different In composition fractions in APT measurements. These quantum well width fluctuations (QWWFs) were observed to be of the order of 1 monolayer and were found to be present on the upper interface of the QW, while the lower interface was reported to be comparatively smooth. The authors speculated that the QWWFs could provide a mechanism for carrier localisation.

Separate works by Graham *et al.* [56], Mayrock *et al.* [75], and Hangleiter *et al.* [76] had previously identified single monolayer QWWFs as a possible source of the broad emission spectra observed for InGaN/GaN QWs. This is due to the large piezoelectric polarisation-induced fields across the QWs which result a larger potential drop across the QW in regions where the effective width of the QW is greater, resulting in a reduced electron-hole recombination energy in these regions. This is illustrated schematically in one dimension in Figure 2.6. Watson-Parris *et al.* [40] compared solutions to the Schrödinger equation for electrons and holes in an InGaN QW where In atoms were randomly distributed in cases with and without monolayer QWWFs at the upper QW interface, based on the work of Galtrey *et al.* [74]. The random distribution of atoms was simulated by a smoothly varying concentration function. By comparing the calculated electron and hole localisation lengths for the two cases,

the authors concluded that holes are strongly localised at regions of above average In content but that electrons are much less susceptible to localisation at alloy composition fluctuations. It was concluded that electrons are localised by a combination of composition fluctuations and QWWFs. Electrons and holes were shown to be localised at opposite interfaces of the QW due to the net electric field across it, and the in-plane electron localisation was shown to be enhanced by the inclusion of QWWFs in the model.

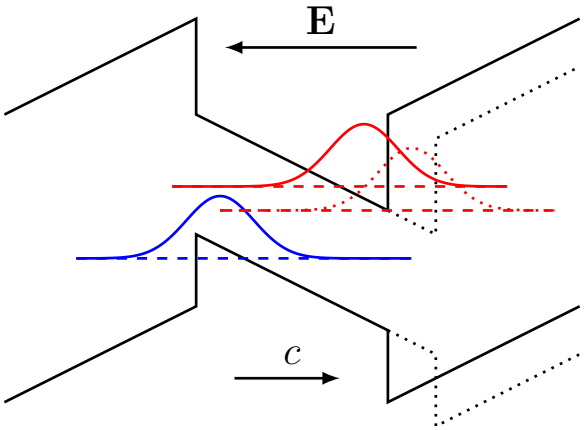

Figure 2.6: Schematic diagram showing localisation of an electron at a QWWF in one dimension. The electron and hole wavefunctions are shown in red and blue, respectively. The electron wavefunction is confined at a lower energy in the wider QW (dotted lines) due to the additional potential drop across the well. The growth direction (c axis) is labelled. **E** is the net electric field across the QW.

In the work by Watson-Parris *et al.* [40], the alloy composition variation throughout the QW was modelled as a smoothly varying continuum. The Coulomb interaction between electrons and holes was assumed to be negligible due to their large spatial separation as a result of the electric fields across polar QWs. A fully atomistic model of InGaN/GaN QWs was developed by Schulz *et al.* [77]. The 3-dimensional wavefunction extents for the lowest energy electron and hole states, referred to as the ground states, were calculated and presented for cases with and without the inclusion of the Coulomb interaction between carriers. A region of an InGaN/GaN QW was modelled as a supercell of approximately 82 000 atoms in which In atoms were randomly distributed in the alloy. The In composition fraction was 25 %. QWWFs were included

as a disc-shaped structures with a diameter of 5 nm and a height of 2 monolayers at the top QW/barrier interface. The calculations were repeated multiple times to give different random atomic configurations analogous to different regions of a QW. Hole wavefunctions were found to be localised at regions of high In concentration, close to the bottom QW interface, while electrons were localised at QWWFs at the top interface. This resulted in a variation in the ground state energies of 2–45 meV for electrons and 10–150 meV for holes, the combination of which was given as the reason for the broad luminescence peaks observed experimentally for these structures. The in-plane separation between electrons and holes was also reported to vary between the different random atomic configurations and was shown to have a significant impact on the total wavefunction overlap between electron and hole states. When the Coulomb interaction between electrons and holes was included in the calculations, slight changes in the in-plane separations of the electrons and holes occurred but their separations parallel to the growth axis were not significantly affected. The authors therefore concluded that electrons and holes must be localised at opposite QW interfaces in real structures, as well as in the plane of the QW, and that the strength of the Coulomb interaction is not sufficient to overcome the electric fields across QWs due to the piezoelectric polarisation. The in-plane electron-hole separation is illustrated in Figures 2.7(a) (perpendicular to the c axis) and 2.7(b) (parallel to the c axis). These are schematic representations of the charge density maps calculated by Schulz *et al.* [77].

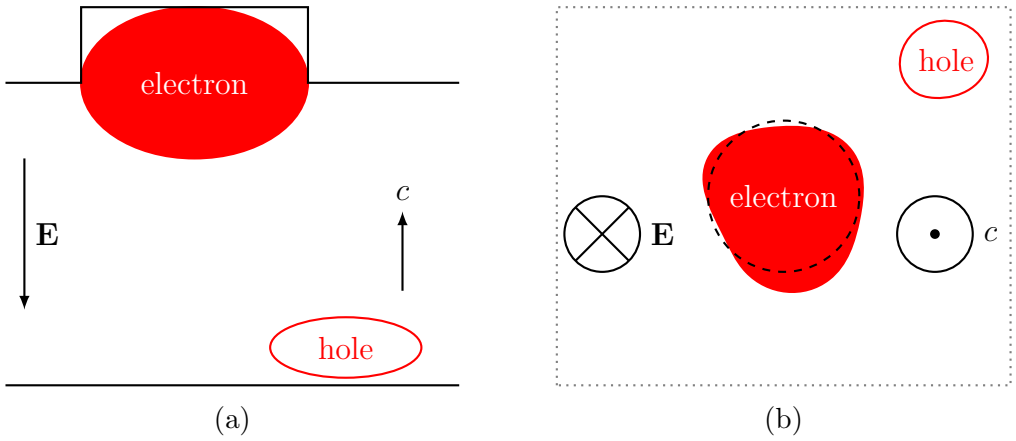

Figure 2.7: Schematic diagrams showing the electron and hole separations due to localisation of the electron at a QWWF and of the hole at a random alloy composition fluctuation. (a) and (b) show the same system viewed from the side (perpendicular to the c axis) and from above (parallel to the c axis, where the disc-shaped QWWF is represented by the dashed line). The separate localisation occurs both parallel to the growth (c) axis and in the plane of the QW. This is a schematic illustration of the type of result presented in the work of Schulz *et al.* [77]. **E** is the net electric field across the QW.

The atomistic calculations developed by Schulz *et al.* [77] were repeated in work by Tanner *et al.* [78] for QWs with different In composition fractions, 10, 15 and 25 %, based on real structures investigated by Graham *et al.* [56], and for the first 60 confined electron and hole states. The calculations were repeated 20 times and the hole ground state energies were reported to vary by $\sim\pm100$ meV about the mean value for all QW In composition fractions. The authors reported this as significant as it demonstrated that the effects of hole localisation at random alloy composition fluctuations are important for QW In fractions as low as 10 %. The variations about the mean value for the electron ground state energies were found to be strongly dependent on the QW In composition fraction, with variations of $\sim\pm10$ meV and $\sim\pm20$ meV reported for the 10 and 25 % In QWs, respectively, and $\sim\pm50$ meV for the 15 % In QW. This was attributed to the different electric field strengths across the QWs due to the different In fractions: in the lowest electric field case (10 % In), the electron ground states were mostly weakly localised near the QWWFs, while for the strongest electric field (25 % In) they were mostly strongly localised at the QWWFs. For the intermediate

case (15 % In), the electron ground states were found to be either strongly or weakly localised at the QWWFs depending on the particular atomic configuration. This was supported by the experimental results of Graham *et al.* [56], who compared PL spectra from QWs with In fractions ranging from 5–25 %, where the broadest emission peak was observed for the 15 % In QW. This further confirmed the important effect of the electric fields across InGaN/GaN QWs on electron localisation. Tanner *et al.* [78] also calculated the wavefunction extents of higher energy electron and hole states in the same atomic configurations as the ground states. The wavefunction overlaps among different electron or hole states were then used to calculate the likelihood of a carrier transferring from one state to another. The less likely a carrier is to transfer to another energy state, the more strongly localised it is. It was found that hole states are strongly localised over an energy range of ∼100 meV even when the QW In fraction is as low as 10 %, and that therefore holes are strongly localised at alloy composition fluctuations up to room temperature. This energy range was found to increase with increasing QW In fraction. On the other hand, electron states were found to be comparatively weakly localised. This would mean that low temperature QW PL peak width, and the temperature dependence of the peak emission energy, described above, are dominated by localised holes [39, 41]. The model developed in the works of Schulz *et al.* [77] and Tanner *et al.* [78] provides a detailed explanation for the donor-acceptor pair-like recombination suggested by Morel *et al.* [57, 58], where the "nanotexture" to which the latter group refer is provided by In composition fluctuations and QWWFs for holes and electrons, respectively. Conceptually similar models for such a "localisation landscape" have since been developed by other groups [79–82], as it is now clear that a simple 1-dimensional model is insufficient when attempting to calculate the emission energies of InGaN/GaN QWs due to the disorder.

In the work featured in this thesis, electrons and holes are treated as being localised in polar InGaN/GaN QWs as predicted by the fully atomistic model of Schulz *et al.* [77] and Tanner *et al.* [78].

2.6 References

[1] D. Ehrentraut *et al.* "High quality, low cost ammonothermal bulk GaN substrates". *Japanese Journal of Applied Physics* **52**, 8 Part 2 (2013), 1. DOI: 10.7567/JJAP.52.08JA01 (Cited on page 28).

[2] E. R. Dobrovinskaya *et al.* "Properties of Sapphire". *Sapphire*. Boston, MA: Springer US, 2009, 55. DOI: 10.1007/978-0-387-85695-7_2 (Cited on page 28).

[3] I. Vurgaftman and J. R. Meyer. "Band parameters for nitrogen-containing semiconductors". *Journal of Applied Physics* **94**, 6 (2003), 3675. DOI: 10.1063/1.1600519 (Cited on pages 29, 30, 31, 32, 33, 34, 35).

[4] S. D. Lester *et al.* "High dislocation densities in high efficiency GaN-based light-emitting diodes". *Applied Physics Letters* **66**, 10 (1995), 1249. DOI: 10.1063/1.113252 (Cited on page 30).

[5] F. A. Ponce *et al.* "Characterization of dislocations in GaN by transmission electron diffraction and microscopy techniques". *Applied Physics Letters* **69**, 6 (1996), 770. DOI: 10.1063/1.117886 (Cited on page 30).

[6] B. Heying *et al.* "Role of threading dislocation structure on the x-ray diffraction peak widths in epitaxial GaN films". *Applied Physics Letters* **643**, 1996 (1995), 643. DOI: 10.1063/1.116495 (Cited on page 30).

[7] W. A. Brantley *et al.* "Effect of dislocations on green electroluminescence efficiency in GaP grown by liquid phase epitaxy". *Journal of Applied Physics* **46**, 6 (1975), 2629. DOI: 10.1063/1.321941 (Cited on page 30).

[8] R. J. Roedel *et al.* "The Effect of Dislocations in GaAlAs:Si Light-Emitting Diodes". *Journal of Electrochemical Society* **126**, 15 (1979), 637 (Cited on page 30).

[9] T. Mukai *et al.* "Characteristics of InGaN-Based UV/Blue/Green/Amber/Red Light-Emitting Diodes". *Japanese Journal of Applied Physics* **38**, Part 1, No. 7A (1999), 3976. DOI: 10.1143/JJAP.38.3976 (Cited on pages 30, 40, 41).

[10] S. Nakamura. "The Roles of Structural Imperfections in InGaN-Based Blue Light-Emitting Diodes and Laser Diodes". *Science* **281**, 5379 (1998), 956. DOI: 10.1126/science.281.5379.956 (Cited on pages 30, 40).

[11] Q. Dai *et al.* "Internal quantum efficiency and nonradiative recombination coefficient of GaInN/GaN multiple quantum wells with different dislocation densities". *Applied Physics Letters* **94**, 11 (2009), 1. DOI: 10.1063/1.3100773 (Cited on page 30).

[12] Y. Varshni. "Temperature dependence of the energy gap in semiconductors". *Physica* **34**, 1 (1967), 149. DOI: 10.1016/0031-8914(67)90062-6 (Cited on pages 30, 41).

[13] F. Bernardini and V. Fiorentini. "Non-linear macroscopic polarization in III-V nitride alloys". *Physical Review B* **64** (2001), 085207. DOI: 10.1103/PhysRevB.64.085207 (Cited on pages 31, 34, 35).

[14] J. Wu *et al.* "Universal bandgap bowing in group-III nitride alloys". *Solid State Communications* **127**, 6 (2003), 411. DOI: 10.1016/S0038-1098(03)00457-5 (Cited on pages 31, 32).

[15] J. Wu *et al.* "Temperature dependence of the fundamental band gap of InN". *Journal of Applied Physics* **94**, 7 (2003), 4457. DOI: 10.1063/1.1605815 (Cited on pages 31, 32).

[16] F. Bernardini *et al.* "Accurate calculation of polarization-related quantities in semiconductors". *Physical Review B* **63** (2001), 193201. DOI: 10.1103/PhysRevB.63.193201 (Cited on pages 34, 35).

[17] V. Fiorentini *et al.* "Effects of macroscopic polarization in III-V nitride multiple quantum wells". *Physical Review B* **60**, 12 (1999), 8849. DOI: 10.1103/PhysRevB.60.8849 (Cited on pages 34, 36, 38).

[18] V. D. Jovanović. "Strained quantum wells". *Quantum Wells, Wires and Dots*. Ed. by P. Harrison. Chichester, UK: John Wiley & Sons, Ltd, 2016, 223. DOI: 10.1002/9781118923337.ch7 (Cited on pages 34, 35, 36).

[19] F. Della Sala *et al.* "Free-carrier screening of polarization fields in wurtzite GaN/InGaN laser structures". *Applied Physics Letters* **74**, 14 (1999), 2002. DOI: 10.1063/1.123727 (Cited on pages 34, 35).

[20] D. A. B. Miller *et al.* "Band-edge electroabsorption in quantum well structures: the quantum-confined Stark effect". *Physical Review Letters* **53**, 22 (1984), 2173 (Cited on page 37).

[21] M. Fox. *Optical Properties of Solids*. 2nd ed. Oxford University Press, 2010, 160 (Cited on page 37).

[22] T. Takeuchi *et al.* "Quantum-Confined Stark Effect due to Piezoelectric Fields in GaInN Strained Quantum Wells". *Japanese Journal of Applied Physics* **36**, Part 2, No. 4A (1997), L382. DOI: 10.1143/JJAP.36.L382 (Cited on page 38).

[23] T. Takeuchi *et al.* "Determination of piezoelectric fields in strained GaInN quantum wells using the quantum-confined Stark effect". *Applied Physics Letters* **73**, 12 (1998), 1691. DOI: 10.1063/1.122247 (Cited on page 38).

[24] M. Auf der Maur *et al.* "Efficiency Drop in Green InGaN/GaN Light Emitting Diodes: The Role of Random Alloy Fluctuations". *Physical Review Letters* **116**, 2 (2016), 027401. DOI: 10.1103/PhysRevLett.116.027401 (Cited on page 38).

[25] T. H. Ngo *et al.* "Internal quantum efficiency in yellow-amber light emitting AlGaN-InGaN-GaN heterostructures". *Applied Physics Letters* **107**, 12 (2015), 122103. DOI: 10.1063/1.4931624 (Cited on page 38).

[26] S. Yoshida *et al.* "Improvements on the electrical and luminescent properties of reactive molecular beam epitaxially grown GaN films by using AlN-coated sapphire substrates". *Applied Physics Letters* **42**, 5 (1983), 427. DOI: 10.1063/1.93952 (Cited on page 38).

[27] M. Sano and M. Aoki. "Epitaxial Growth of Undoped and Mg-Doped GaN". *Japanese Journal of Applied Physics* **15**, 10 (1976), 1943. DOI: 10.1143/JJAP.15.1943 (Cited on page 38).

[28] H. Amano *et al.* "Metalorganic vapor phase epitaxial growth of a high quality GaN film using an AlN buffer layer". *Applied Physics Letters* **48**, 5 (1986), 353. DOI: 10.1063/1.96549 (Cited on page 38).

[29] S. Nakamura *et al.* "Highly P-Typed Mg-Doped GaN Films Grown with GaN Buffer Layers". *Japanese Journal of Applied Physics* **30**, Part 2, No. 10A (1991), L1708. DOI: 10.1143/JJAP.30.L1708 (Cited on page 38).

[30] F. Scholz *et al.* "In incorporation efficiency and composition fluctuations in MOVPE grown GaInN/GaN hetero structures and quantum wells". *Materials Science and Engineering: B* **50**, 1-3 (1997), 238. DOI: 10.1016/S0921-5107(97)00184-0 (Cited on page 38).

[31] M. Bosi and R. Fornari. "A study of Indium incorporation efficiency in InGaN grown by MOVPE". *Journal of Crystal Growth* **265**, 3-4 (2004), 434. DOI: 10.1016/j.jcrysgro.2004.02.103 (Cited on page 38).

[32] R. A. Oliver *et al.* "The impact of gross well width fluctuations on the efficiency of GaN-based light emitting diodes". *Applied Physics Letters* **103**, 14 (2013), 141114. DOI: 10.1063/1.4824193 (Cited on pages 38, 39).

[33] N. K. Van Der Laak *et al.* "Characterization of InGaN quantum wells with gross fluctuations in width". *Journal of Applied Physics* **102** (2007), 013513. DOI: 10.1063/1.2751401 (Cited on page 39).

[34] F. C.-P. Massabuau *et al.* "Investigation of unintentional indium incorporation into GaN barriers of InGaN/GaN quantum well structures". *physica status solidi (b)* **252**, 5 (2015), 928. DOI: 10.1002/pssb.201451543 (Cited on page 39).

[35] C. Weisbuch *et al.* "The efficiency challenge of nitride light-emitting diodes for lighting". *physica status solidi (a)* **212**, 5 (2015), 899. DOI: 10.1002/pssa.201431868 (Cited on page 40).

[36] T. Sano *et al.* "High Internal Quantum Efficiency Blue-Green Light-Emitting Diode with Small Efficiency Droop Fabricated on Low Dislocation Density GaN Substrate". *Japanese Journal of Applied Physics* **52**, 8S (2013), 08JK09. DOI: 10.7567/JJAP.52.08JK09 (Cited on page 40).

[37] S. Chichibu *et al.* "Luminescences from localized states in InGaN epilayers". *Applied Physics Letters* **70**, 21 (1997), 2822. DOI: 10.1063/1.119013 (Cited on page 40).

[38] Q. Li *et al.* "Thermal redistribution of localized excitons and its effect on the luminescence band in InGaN ternary alloys". *Applied Physics Letters* **79**, 12 (2001), 1810. DOI: 10.1063/1.1403655 (Cited on page 40).

[39] S. Hammersley *et al.* "The consequences of high injected carrier densities on carrier localization and efficiency droop in InGaN/GaN quantum well structures". *Journal of Applied Physics* **111**, 8 (2012), 083512. DOI: 10.1063/1.3703062 (Cited on pages 40, 48).

[40] D. Watson-Parris *et al.* "Carrier localization mechanisms in InGaN/GaN quantum wells". *Physical Review B* **83**, 11 (2011), 115321. DOI: 10.1103/PhysRevB.83.115321 (Cited on pages 40, 44, 45).

[41] P. Dawson *et al.* "The nature of carrier localisation in polar and nonpolar InGaN/GaN quantum wells". *Journal of Applied Physics* **119**, 18 (2016), 181505. DOI: 10.1063/1.4948237 (Cited on pages 40, 43, 48).

[42] S. Nakamura *et al.* "High-brightness InGaN blue, green and yellow light-emitting diodes with quantum well structures". *Japanese Journal of Applied Physics* **34**, 7 (1995), L797. DOI: 10.1143/JJAP.34.L797 (Cited on page 40).

[43] K. P. O'Donnell *et al.* "Optical linewidths of InGaN light emitting diodes and epilayers". *Applied Physics Letters* **70**, 14 (1997), 1843. DOI: 10.1063/1.118728 (Cited on page 40).

[44] Y. D. Qi *et al.* "Comparison of blue and green InGaN/GaN multiple-quantum-well light-emitting diodes grown by metalorganic vapor phase epitaxy". *Applied Physics Letters* **86**, 10 (2005), 101903. DOI: 10.1063/1.1866634 (Cited on page 40).

[45] E. Jung *et al.* "Electrical and optical characteristics of GaN-based light-emitting diodes fabricated with emission wavelengths of 429-467nm". *Current Applied Physics* **12**, 3 (2012), 885. DOI: 10.1016/j.cap.2011.12.002 (Cited on page 40).

[46] T. Li *et al.* "Carrier localization and nonradiative recombination in yellow emitting InGaN quantum wells". *Applied Physics Letters* **96**, 3 (2010), 031906. DOI: 10.1063/1.3293298 (Cited on page 40).

[47] Y.-H. Cho *et al.* "S-shaped temperature-dependent emission shift and carrier dynamics in InGaN/GaN multiple quantum wells". *Applied Physics Letters* **73**, 10 (1998), 1370. DOI: 10.1063/1.122164 (Cited on page 40).

[48] R. Pecharromán-Gallego *et al.* "Investigation of the unusual temperature dependence of InGaN/GaN quantum well photoluminescence over a range of emission energies". *Journal of Physics D: Applied Physics* **37**, 21 (2004), 2954. DOI: 10.1088/0022-3727/37/21/003 (Cited on page 40).

[49] P. G. Eliseev *et al.* "Band-tail model and temperature-induced blue-shift in photoluminescence spectra of InxGa1-xN grown on sapphire". *Journal of Elec-*

tronic Materials **29**, 3 (2000), 332. DOI: 10.1007/s11664-000-0073-9 (Cited on page 40).

[50] P. G. Eliseev. "The red $\sigma 2$/kT spectral shift in partially disordered semiconductors". *Journal of Applied Physics* **93**, 9 (2003), 5404. DOI: 10.1063/1.1567055 (Cited on page 40).

[51] O. Rubel *et al.* "Quantitative description of disorder parameters in (GaIn)(NAs) quantum wells from the temperature-dependent photoluminescence spectroscopy". *Journal of Applied Physics* **98**, 6 (2005), 063518. DOI: 10.1063/1.2058192 (Cited on page 40).

[52] O. Rubel *et al.* "Model of temperature quenching of photoluminescence in disordered semiconductors and comparison to experiment". *Physical Review B* **73**, 23 (2006), 233201. DOI: 10.1103/PhysRevB.73.233201 (Cited on page 40).

[53] S. Chichibu *et al.* "Spontaneous emission of localized excitons in InGaN single and multiquantum well structures". *Applied Physics Letters* **69**, 27 (1996), 4188. DOI: 10.1063/1.116981 (Cited on pages 41, 43).

[54] S. F. Chichibu *et al.* "Localized quantum well excitons in InGaN single-quantum-well amber light-emitting diodes". *Journal of Applied Physics* **88**, 9 (2000), 5153. DOI: 10.1063/1.1314906 (Cited on page 41).

[55] S. Kalliakos *et al.* "Large size dependence of exciton-longitudinal-optical-phonon coupling in nitride-based quantum wells and quantum boxes". *Applied Physics Letters* **80**, 3 (2002), 428. DOI: 10.1063/1.1433165 (Cited on pages 41, 42).

[56] D. M. Graham *et al.* "Optical and microstructural studies of InGaN/GaN single-quantum-well structures". *Journal of Applied Physics* **97**, 10 (2005), 103508. DOI: 10.1063/1.1897070 (Cited on pages 41, 42, 43, 44, 47, 48).

[57] A. Morel *et al.* "Donor-acceptor-like behavior of electron-hole pair recombinations in low-dimensional (Ga,In)N/GaN systems". *Physical Review B* **68**, 4

(2003), 045331. DOI: 10.1103/PhysRevB.68.045331 (Cited on pages 41, 43, 48).

[58] A. Morel *et al.* "Two-dimensional pseudo-donor-acceptor-pairs model of recombination dynamics in InGaN/GaN quantum wells". *Physica E: Low-dimensional Systems and Nanostructures* **17** (2003), 64. DOI: 10.1016/S1386-9477(02)00762-2 (Cited on pages 41, 43, 48).

[59] K. Huang and A. Rhys. "Theory of Light Absorption and Non-Radiative Transitions in F-Centres". *Proceedings of the Royal Society A: Mathematical, Physical and Engineering Sciences* **204**, 1078 (1950), 406. DOI: 10.1098/rspa.1950.0184 (Cited on page 42).

[60] R. Pecharromán-Gallego *et al.* "Investigations of phonon sidebands in InGaN/GaN multi-quantum well luminescence". *Materials Science and Engineering: B* **93**, 1-3 (2002), 94. DOI: 10.1016/S0921-5107(02)00024-7 (Cited on page 42).

[61] J. A. Davidson *et al.* "Photoluminescence studies of InGaN/GaN multi-quantum wells". *Semiconductor Science and Technology* **15**, 6 (2000), 497. DOI: 10.1088/0268-1242/15/6/302 (Cited on page 42).

[62] J. Wagner *et al.* "Effect of strain and associated piezoelectric fields in InGaN/GaN quantum wells probed by resonant Raman scattering". *Applied Physics Letters* **74**, 25 (1999), 3863. DOI: 10.1063/1.124205 (Cited on page 42).

[63] D. M. Graham. "Optical Studies of III-Nitride Quantum Well Structures". PhD thesis. University of Manchester, 2005 (Cited on page 43).

[64] M. Shahmohammadi *et al.* "Enhancement of Auger recombination induced by carrier localization in InGaN/GaN quantum wells". *Physical Review B* **95**, 12 (2017), 125314. DOI: 10.1103/PhysRevB.95.125314 (Cited on page 43).

[65] Y. Narukawa *et al.* "Role of self-formed InGaN quantum dots for exciton localization in the purple laser diode emitting at 420 nm". *Applied Physics Letters* **70**, 8 (1997), 981. DOI: 10.1063/1.118455 (Cited on page 43).

[66] D. Gerthsen *et al.* "Composition Fluctuations in InGaN Analyzed by Transmission Electron Microscopy". *physica status solidi (a)* **177**, 1 (2000), 145. DOI: 10.1002/(SICI)1521-396X(200001)177:1<145::AID-PSSA145>3.0.CO;2-0 (Cited on page 43).

[67] K. O'Donnell *et al.* "Origin of Luminescence from InGaN Diodes". *Physical Review Letters* **82**, 1 (1999), 237. DOI: 10.1103/PhysRevLett.82.237 (Cited on page 43).

[68] T. M. Smeeton *et al.* "Electron-beam-induced strain within InGaN quantum wells: False indium cluster detection in the transmission electron microscope". *Applied Physics Letters* **83**, 26 (2003), 5419. DOI: 10.1063/1.1636534 (Cited on page 43).

[69] T. M. Smeeton *et al.* "Analysis of InGaN/GaN single quantum wells by X-ray scattering and transmission electron microscopy". *physica status solidi (b)* **240**, 2 (2003), 297. DOI: 10.1002/pssb.200303262 (Cited on page 43).

[70] T. M. Smeeton *et al.* "The impact of electron beam damage on the detection of indium-rich localisation centres in InGaN quantum wells using transmission electron microscopy". *Journal of Materials Science* **41**, 9 (2006), 2729. DOI: 10.1007/s10853-006-7876-x (Cited on page 43).

[71] J. P. O'Neill *et al.* "Electron-beam-induced segregation in InGaN/GaN multiple-quantum wells". *Applied Physics Letters* **83**, 10 (2003), 1965. DOI: 10.1063/1.1606105 (Cited on page 43).

[72] M. J. Galtrey *et al.* "Three-dimensional atom probe studies of an InxGa1-xN/GaN multiple quantum well structure: Assessment of possible indium clus-

tering". *Applied Physics Letters* **90**, 6 (2007), 2005. DOI: 10.1063/1.2431573 (Cited on page 44).

[73] L.-W. Wang. "Calculations of carrier localization in InxGa1-xN". *Physical Review B* **63**, 24 (2001), 245107. DOI: 10.1103/PhysRevB.63.245107 (Cited on page 44).

[74] M. J. Galtrey *et al.* "Three-dimensional atom probe analysis of green- and blue-emitting InGaN/GaN multiple quantum well structures". *Journal of Applied Physics* **104**, 1 (2008), 013524. DOI: 10.1063/1.2938081 (Cited on page 44).

[75] O. Mayrock *et al.* "Influence of Internal Polarization Fields on the Disorder Broadening of Excitons in (In,Ga)N/GaN Quantum Wells". *physica status solidi (b)* **216**, 1 (1999), 419. DOI: 10.1002/(SICI)1521-3951(199911)216:1<419::AID-PSSB419>3.0.CO;2-G (Cited on page 44).

[76] A. Hangleiter *et al.* "Optical Properties of Nitride Quantum Wells: How to Separate Fluctuations and Polarization Field Effects". *physica status solidi (b)* **216**, 1 (1999), 427. DOI: 10.1002/(SICI)1521-3951(199911)216:1<427::AID-PSSB427>3.0.CO;2-K (Cited on page 44).

[77] S. Schulz *et al.* "Atomistic analysis of the impact of alloy and well-width fluctuations on the electronic and optical properties of InGaN/GaN quantum wells". *Physical Review B* **91**, 3 (2015), 035439. DOI: 10.1103/PhysRevB.91.035439 (Cited on pages 45, 46, 47, 48).

[78] D. S. P. Tanner *et al.* "Random alloy fluctuations and structural inhomogeneities in c-plane InGaN quantum wells: theory of ground and excited electron and hole states". *RSC Advances* **6**, 69 (2016), 64513. DOI: 10.1039/C6RA07540A (Cited on pages 47, 48).

[79] C. M. Jones *et al.* "Impact of carrier localization on recombination in InGaN quantum wells and the efficiency of nitride light-emitting diodes: Insights from

theory and numerical simulations". *Applied Physics Letters* **111**, 11 (2017), 113501. DOI: 10.1063/1.5002104 (Cited on page 48).

[80] M. Filoche *et al.* "Localization landscape theory of disorder in semiconductors. I. Theory and modeling". *Physical Review B* **95**, 14 (2017), 144204. DOI: 10.1103/PhysRevB.95.144204 (Cited on page 48).

[81] M. Piccardo *et al.* "Localization landscape theory of disorder in semiconductors. II. Urbach tails of disordered quantum well layers". *Physical Review B* **95**, 14 (2017), 144205. DOI: 10.1103/PhysRevB.95.144205 (Cited on page 48).

[82] C.-K. Li *et al.* "Localization landscape theory of disorder in semiconductors. III. Application to carrier transport and recombination in light emitting diodes". *Physical Review B* **95**, 14 (2017), 144206. DOI: 10.1103/PhysRevB.95.144206 (Cited on page 48).

Chapter 3

Experimental Techniques

In this Chapter, the experimental techniques used for the work in this thesis are outlined along with some of the underlying physics. The technique of photoluminescence spectroscopy is described, followed by an explanation of the time-correlated single photon counting system that was used in time-resolved experiments.

3.1 Photoluminescence Spectroscopy

Photoluminescence (PL) spectroscopy concerns the collection and analysis of the light emitted from materials following excitation by a light source. It is a non-destructive technique, and careful interpretation of the collected spectrum or spectra can provide valuable information about the recombination processes in semiconductors.

In PL spectroscopy, light from a monochromatic source is focused onto a sample of the material. The photon energy of this light is usually greater than the bandgap energy of the material in question, and the absorption of photons creates electron-hole pairs. The electrons and holes cool rapidly to potential minima in the conduction band (CB) and the valence band (VB) respectively, or are trapped by impurities or defects, and then recombine. When this recombination is radiative, the resultant emitted photons are collected by a detector.

In the work described in this thesis, the excitation sources used were: a continuous-wave (CW) He-Cd laser, providing excitation photons at a wavelength of 325 nm (corresponding to an energy of 3.815 eV) with a maximum power of 30 mW; a laser diode emitting at 405 nm (energy 3.061 eV) with a maximum power of 40 mW; or a frequency-tripled pulsed Ti:sapphire laser (described in more detail in Section 3.2.1), with a final photon wavelength of 266 nm (energy 4.661 eV) and a maximum pulse energy of $\sim$0.1 nJ. The excitation light was modulated using a mechanical chopper before being focused onto the sample. The sample was held on the cold finger of a temperature-controlled closed-cycle He cryostat, allowing measurements to be performed at temperatures ranging from 10–300 K. The light emitted by the sample was focused onto the entrance slit of either a 0.75 m single grating monochromating spectrometer with dispersion 16 Å mm^{-1}, or a 0.85 m double grating monochromating spectrometer with dispersion 8 Å mm^{-1}. The angle of the diffraction grating in the spectrometer, and so the detection wavelength, was controlled by a personal computer (PC). A long-pass filter was placed at the slit entrance to prevent the collection of scattered excitation light. The dispersed PL was detected by a cooled GaAs photomultiplier tube (PMT) and the generated signal passed through a lock-in amplifier with the reference frequency set to that of the chopper, so that only the component of the detected signal that was in phase with the frequency of the chopped laser light would be amplified. This amplitude of this signal was recorded by the PC as the detection wavelength was varied. A schematic diagram of the experimental set-up for PL spectroscopy is shown in Figure 3.1.

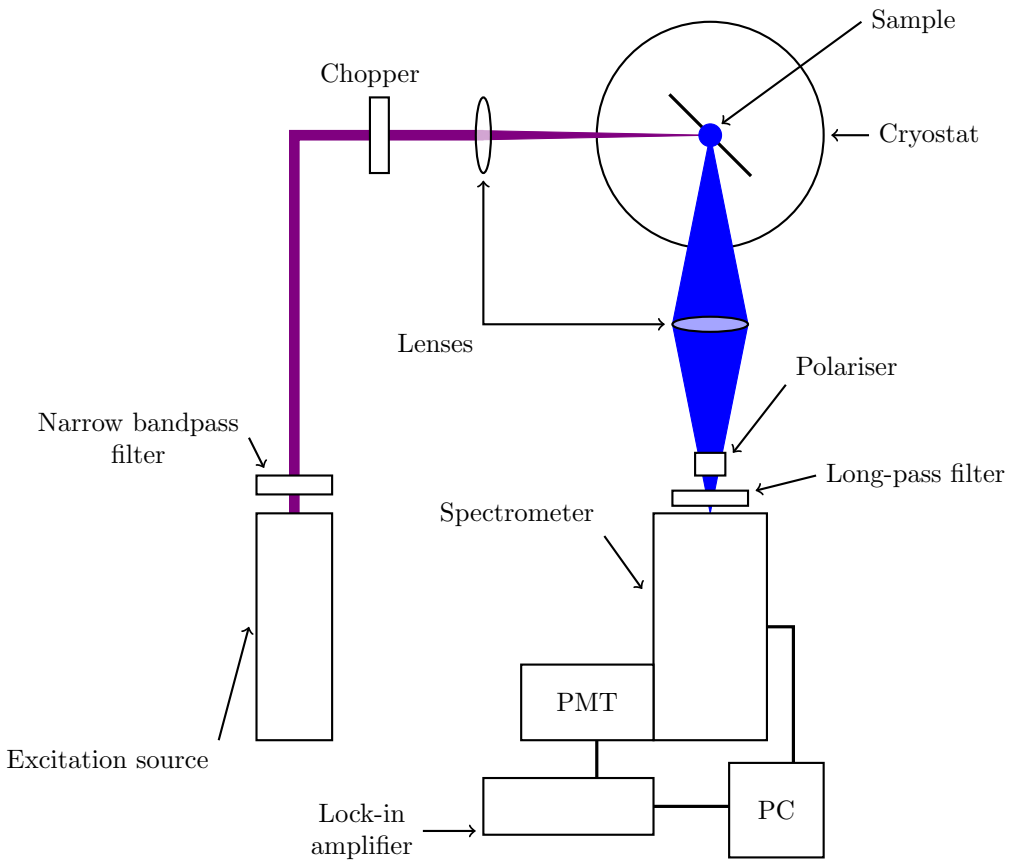

Figure 3.1: Schematic diagram of the PL experimental set-up. The labelled components are described in the text.

A narrow bandpass filter was placed at the output of the He-Cd laser to attenuate spontaneous emission which is emitted from the plasma additionally to the laser line, which would otherwise be scattered off the sample and into the detector, giving rise to features on the spectrum which do not originate from the PL.

In the cases where the pulsed laser source was used to excite the sample for basic PL spectroscopy, the spectra are referred to as time-integrated photoluminescence (TIPL) spectra as the signal detected at a given detection energy is integrated over many laser pulses as well as over the time between laser pulses when no excitation is taking place.

The power of the laser excitation was controlled by placing a series of discrete neutral density filters at the output of the laser.

The wavelength resolution of the spectrum was determined by the width of the

entrance and exit slits of the spectrometer, as well as the step size selected for the signal acquisition over a particular spectral range. The time constant of the lock-in amplifier could also be varied, with longer time constants used when acquiring weaker signals to reduce the impact of random noise on the spectrum. In some cases, multiple accumulations were performed at each detection wavelength and then averaged, also to reduce noise on the spectrum.

3.1.1 Brewster Angle Geometry

The reflectivity, R, of normally incident light on an interface between two media with different refractive indices, n_1 and n_2, is given by

$$R = \left(\frac{n_1 - n_2}{n_1 + n_2}\right)^2. \tag{3.1}$$

The refractive index of GaN for light of wavelength 400 nm is 2.565 [1]. From Eqution 3.1, this gives a value of R for the GaN/air interface of 19.3 %. The refractive index of sapphire is 1.787 at this wavelength [2], so R is 3.2 % at the GaN/sapphire interface. The non-zero reflectivity values at opposite interfaces result in multiple reflections of the light emitted from a sample between the GaN/air and GaN/sapphire interfaces, analogous to a point source in a cavity. This results in Fabry-Pérot interference oscillations across the PL spectrum [3–5] which are undesirable as they hinder spectral analysis. Therefore, for the experiments described in this thesis, samples were orientated in the horizontal plane at the Brewster angle, θ_B, relative to the optical axis for the GaN/air interface. This is illustrated schematically in Figure 3.2. At this angle, the horizontal component of the emitted light from the sample experiences no reflection at this interface. A Glan-Thompson prism was placed in front of the spectrometer entrance slit to select only the horizontal component, and the Fabry-Pérot interference was suppressed in the collected spectra as a result [3, 4]. Using the

formula,

$$\theta_{\mathrm{B}} = \arctan\left(\frac{n_{\mathrm{air}}}{n_{\mathrm{GaN}}}\right), \tag{3.2}$$

θ_{B} is calculated as 21.3° for emission at 400 nm.

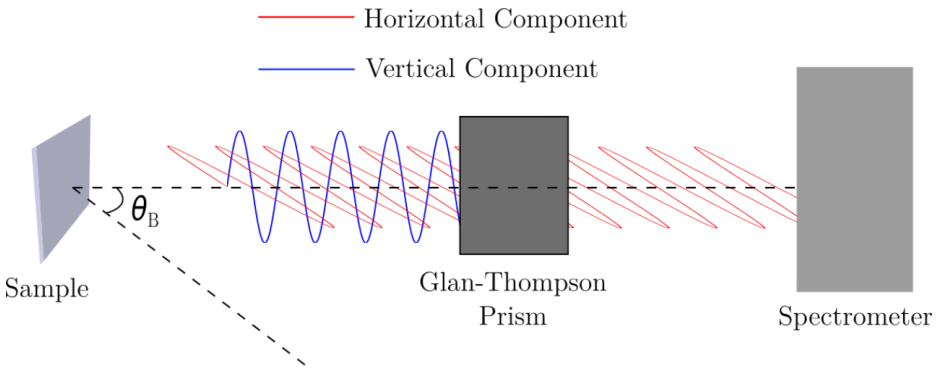

Figure 3.2: Schematic diagram of the Brewster angle geometry.

3.2 Photoluminescence Time Decay Spectroscopy

Studying the PL decay dynamics can provide useful information about the recombination processes taking place. One method for producing PL time decay spectra is time-correlated single photon counting (TCSPC). This technique involves determining the time elapsed between a pulse from the excitation source and the detection of a photon of a particular energy emitted from the sample in the resultant PL. By repeating this process many times, a histogram of the frequency of single photon detection events at different times following excitation is built up which is equivalent to the PL decay transient at the specified detection energy. The details of this method are outlined below and illustrated in Figure 3.3.

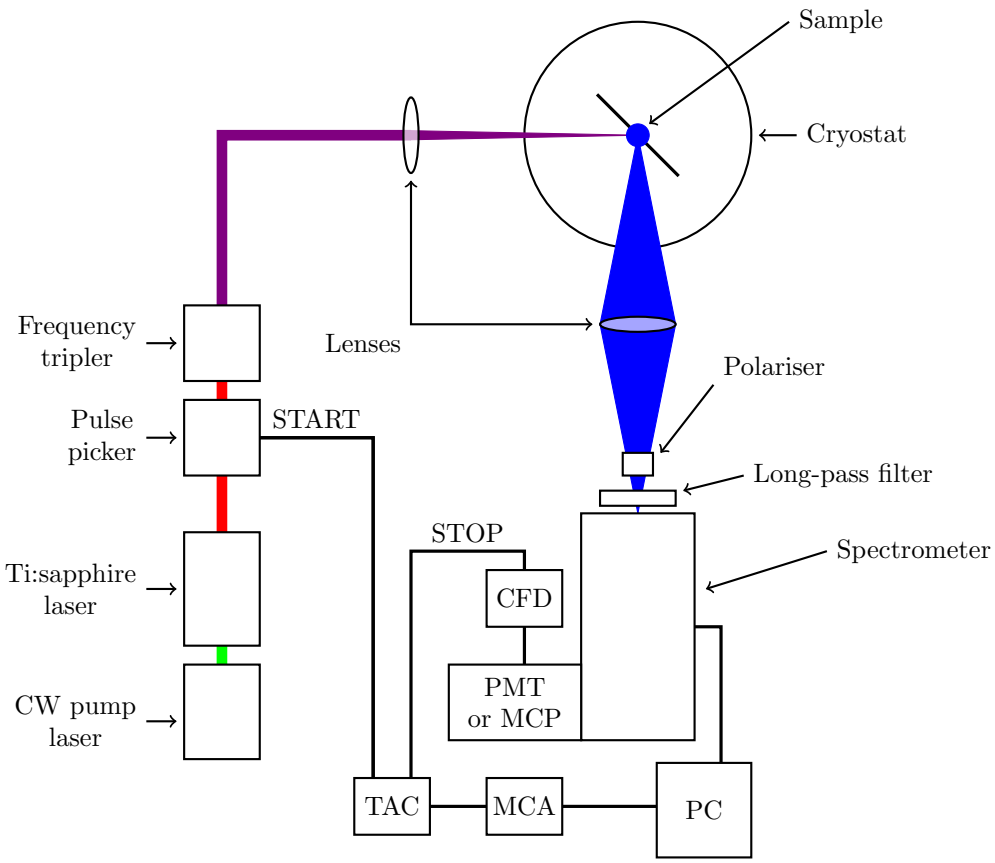

Figure 3.3: Schematic diagram of the TCSPC experimental set-up. The labelled components are described in the text.

3.2.1 Excitation

The excitation pulses originated from a mode-locked Ti:sapphire laser, pumped by a CW diode-pumped solid state laser, at a wavelength of 800 nm, a pulse duration of 100 fs and repetition rate of 80 MHz resulting in a temporal spacing of 12.5 ns. This was passed through a pulse picker, which reduced the pulse frequency to a fraction of the laser repetition rate set so that the time between pulses was sufficient to allow the entirety of the PL spectrum to decay before the sample was excited by another pulse.

Finally, the pulse was passed through two non-linear crystals (second and third harmonic generators) in a frequency tripler to give a final pulse wavelength as 266 nm, equivalent to a photon energy of 4.661 eV.

The excitation pulses described here were also used for TIPL, described in Section 3.1.

3.2.2 Timing and Detection of Photoluminescence

A signal (START) from the pulse picker was sent to a time-to-amplitude converter (TAC), which initiated a linear voltage ramp from 0–1 V. The time over which the voltage ramp occurred was set by the user to a value between 50 ns and 2 ms. A series of delay lines were employed to ensure that the START pulse arrived at the TAC at the same time as the laser pulse arrived at the sample. The desired photon detection energy was selected using the PC-controlled spectrometer, and the voltage output from the PMT following a photon detection event was passed through an amplifier and into a constant fraction discriminator (CFD). The CFD performed two functions. The first was to filter out any signals with amplitudes below a user-set threshold level. This reduced detection events caused by random electronic noise. The second function of the CFD was to eliminate timing errors caused by leading edge detection: signals arriving at the same time but with different amplitudes would be detected at different times as a signal with a large amplitude would reach a given voltage threshold for detection before one with a smaller amplitude. To prevent this, the CFD split the incoming signal into two components which passed down two delay lines of different lengths. One of these components was then subtracted from the other, resulting in a signal that crossed zero at a time independent of its amplitude, illustrated in Figure 3.4. When this occurred, the CFD would output a signal (STOP) that was sent to the TAC to end the voltage ramp. A counter was connected to the CFD to monitor the rate of detected photon counts. The voltage from the TAC was then sorted into one of up to 16 384 channels by a multi-channel analyser (MCA). Each channel corresponded to a narrow voltage range, and therefore a time range. This process was repeated over many START-STOP cycles, and the detection events

were recorded as a histogram on the PC. In the work presented in this thesis, PL decays were typically accumulated until a single MCA channel reached 1000 detected photon counts.

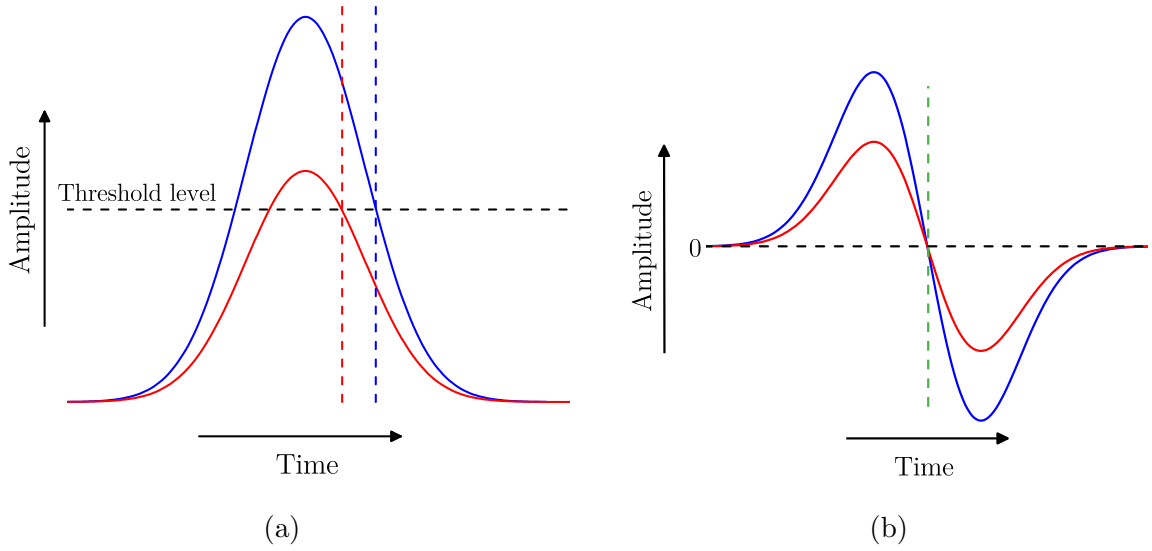

Figure 3.4: Signals with and without processing by a CFD. (a): Signals of different amplitudes cross a pre-defined threshold level at different times (shown by the red and blue dashed lines corresponding to the respective signals of the same colours), even though they are centred on the same point in time. (b): Signals following processing by the CFD. Both cross zero at the point marked by the green dashed line.

Temporal Resolution

In a PMT, a photon incident on the photocathode results in the emission of an electron by the photoelectric effect. This electron is accelerated down the tube by an applied voltage until it encounters a dynode. This event results in the emission of multiple electrons by the dynode which are then accelerated towards another dynode. This multiplication process occurs several times until the final set of electrons reaches the anode, resulting in the detected voltage signal pulse. As the electrons can take any path between the dynodes, the time between the arrival of a photon at the photocathode and the detection of the signal pulse varies by an amount referred to as the transit time spread. This determines the temporal resolution of the TCSPC system [6]. The transit time spread of the GaAs PMT used in the experiments

described in this thesis was ∼200 ps. The transit time spread can be reduced by decreasing the distance between dynodes and thus the variation in possible path lengths for the electrons. This is the case in a micro-channel plate (MCP) detector [6]. For some of the work in this thesis, an MCP with a transit time spread of ∼70 ps was used.

Pulse Pile-Up

Following the detection of a photon by a TCSPC system, no further detection events will be recorded until the next START pulse is received. This means that any additional photons which arrive at the detector between the STOP pulse and the START pulse are rejected. Statistically, these rejected events are most likely to correspond to longer times following excitation. This distorts the measured PL decay transient, leading to an artificial reduction in the measured decay time. This is known as pulse pile-up, and its effect on the PL time decay measurements presented in this thesis was made statistically insignificant by maintaining the rate of detected photons at around 1 % of the repetition rate of the excitation source [6]. This was achieved by attenuating the light collected at the spectrometer using a series of neutral density filters.

3.3 Time-Resolved Photoluminescence Spectroscopy

In time-resolved photoluminescence (TRPL) spectroscopy, the temporal evolution of the entire spectrum is studied. For the work described in this thesis, the same TCSPC system as described in Section 3.2 for PL time decay spectroscopy was employed except that the time over which the TAC voltage ramp occurred, and the START signal delay time, remained fixed. PL decay transients were recorded at regularly

spaced detection energies across the region of the spectrum under investigation. Decay intensity values were averaged over a given time window and then plotted as a function of detection energy, giving PL spectra for the different time windows.

3.4 References

[1] G. Yu *et al.* "Optical properties of wurtzite structure GaN on sapphire around fundamental absorption edge (0.78-4.77 eV) by spectroscopic ellipsometry and the optical transmission method". *Applied Physics Letters* **70**, 24 (1997), 3209. DOI: 10.1063/1.119157 (Cited on page 63).

[2] I. H. Malitson. "Refraction and Dispersion of Synthetic Sapphire". *Journal of the Optical Society of America* **52**, 12 (1962), 1377. DOI: 10.1364/JOSA.52.001377 (Cited on page 63).

[3] D. M. Graham *et al.* "Optical and microstructural studies of InGaN/GaN single-quantum-well structures". *Journal of Applied Physics* **97**, 10 (2005), 103508. DOI: 10.1063/1.1897070 (Cited on page 63).

[4] D. M. Graham. "Optical Studies of III-Nitride Quantum Well Structures". PhD thesis. University of Manchester, 2005 (Cited on page 63).

[5] R. W. Martin *et al.* "Light emission ranging from blue to red from a series of InGaN/GaN single quantum wells". *Journal of Physics D: Applied Physics* **35**, 7 (2002), 604. DOI: 10.1088/0022-3727/35/7/306 (Cited on page 63).

[6] W. Becker. *Advanced Time-Correlated Single Photon Counting Techniques*. Ed. by A. W. Castleman *et al.* Springer Series in Chemical Physics. Springer Berlin Heidelberg, 2005 (Cited on pages 67, 68).

Chapter 4

Effects of a Si-doped InGaN Underlayer on the Optical Properties of InGaN/GaN Multiple Quantum Well Structures

4.1 Introduction

There have been several recent investigations [1–15] into the effects of the inclusion of layers grown prior to the first QW in InGaN/GaN LEDs and in structures studied in PL experiments. These layers, referred to as underlayers (ULs), are often layers of n-doped InGaN and their inclusion has been reported to give rise to a variety of improvements including increased PL or electroluminescence (EL) intensity at low temperature [1–4] and at room temperature [5–7] as well as increased room temperature IQE [1, 2, 8, 9, 11, 14]. However, the precise mechanism(s) for these improvements remain the subject of debate.

As discussed in Chapter 2, it has been demonstrated [15–18] that the spontaneous polarisation in group III-nitrides leads to a depletion field that is in the opposite sense

to the fields across the QWs due to the piezoelectric polarisation. It has been shown that the Fermi level pinning caused by n-type doping can be used to manipulate the strength of this field close to the surface of a structure [12–15, 17, 18], and that this affects the emission properties of QWs grown in this region through modifications to the QCSE [12–15, 18]. It has been suggested that the efficiency improvements reported for structures containing ULs are therefore due to the increased electron-hole wavefunction overlap leading to an increased radiative recombination rate following an increase in the strength of this surface polarisation field [12–14].

Unrelated studies have been carried out on the effect of varying the number of QWs in a MQW structure [19, 20]. It has been shown that thermionic emission of carriers from QWs can be the dominant non-radiative process in single GaAs/AlGaAs QW structures [21]. It was later suggested that this effect occurs in single InGaN/GaN QWs and that it is reduced in MQW structures due to the recapturing of these carriers by other QWs in the system [19]. It has alternatively been proposed that the addition of QWs to a structure leads to a reduced impurity incorporation at interfaces during growth [20]. The introduction of additional QWs to the surface depletion field region will modify the depth of this region and therefore the strength of the field, so it is necessary to investigate the relationship between the efficiency improvements that have been reported as being due to the inclusion of an UL and to the addition of QWs. In this chapter, investigations into the effects of Si-doped ULs are reported for MQW samples where the number of QWs was varied between 1 and 15. Experimental results are compared to calculated CB and VB energy profiles.

4.2 Proposed Effects of Underlayers

There are many mechanisms that have been proposed for the improvements due to the inclusion of ULs. These include a reduction in the impurity or defect incorporation in the active region [1, 2, 8, 9, 22], reduced strain [5, 6, 10], the promotion of so-called

V-pits around threading dislocations [7], the injection of additional electrons into the QW region [3, 4], and the increased strength of the surface depletion field [12–14]. These are each discussed in more detail in this section.

4.2.1 Defect Density Reduction

It has been suggested that the inclusion of an UL leads to a reduction in the incorporation of impurities into QWs or other structures. Dawson and Woodridge [22] reported that the minority carrier lifetime was improved in MBE-grown GaAs/AlGaAs double heterostructures by the inclusion of a 25 nm thick GaAs UL, or a 5-period GaAs/AlGaAs superlattice UL, when compared with samples grown with no UL or with a superlattice grown after rather than before the active region. A reduction in the PL lifetime was reported for the structures including the GaAs and the superlattice ULs, and for structures where the UL was separated from the active region by 10 or 100 nm. The authors attributed the improvements to a reduction in the recombination velocity at GaAs/AlGaAs interfaces, and it was suggested that this was caused by the increased number of growth interfaces, which act as gettering centres for impurities, prior to the active region interfaces. In capacitance-voltage measurements performed by Rimmer *et al.* [23] on the same structures, it was found that the density of interface defect states decreased successively with the growth of additional layers, with the lowest density reported for the structure containing the superlattice UL. The interface recombination velocities determined from TRPL measurements were reported to be proportional to the interface defect state densities, confirming the conclusion reached by Dawson and Woodridge [22].

Akasaka *et al.* [1] studied two 3-period $In_{0.12}Ga_{0.88}N/In_{0.04}Ga_{0.96}N$ QW structures containing 50 nm thick ULs consisting of Si-doped $In_{0.04}Ga_{0.96}N$ grown at 780 °C and GaN grown at 780 °C, respectively. A third structure was grown with an UL region consisting of GaN grown at 1000 °C. The growth temperature of this layer in the

latter structure matched that of the templates on which all of the structures were grown and so that structure was considered equivalent to one with no UL. The room temperature IQE was determined using temperature dependent PL measurements to be higher in the two structures containing ULs compared with the sample with no UL. The highest IQE was reported for the sample with the Si-doped $In_{0.04}Ga_{0.96}N$ UL. The IQE improvements were attributed to the increased separation of the QWs from the growth interruption interface between the high and low temperature growth regions, where it was claimed that non-radiative centres such as nitrogen vacancies or impurity atoms are incorporated via desorption or absorption processes, respectively. The separation of the active region from these defects by a large distance reduces their influence on the QW carrier dynamics. The additional increased IQE for the sample with the Si-doped $In_{0.04}Ga_{0.96}N$ UL was related to work by Kumano *et al.* [24], who reported a reduced threshold excitation power density for stimulated emission in low In fraction InGaN films compared with pure GaN films. Longer carrier lifetimes were also reported for the low In fraction films, and the authors attributed this to reduced incorporation of impurity atoms due to the inclusion of In as a surfactant to modify the growth kinetics [25]. Akasaka *et al.* [2] also reported that the PL decay time decreased with increasing temperature for the samples with GaN ULs, but not for the sample with the Si-doped $In_{0.04}Ga_{0.96}N$ UL, which was concluded to be due to the much reduced density of non-radiative recombination centres in the QWs leading to a reduction in the non-radiative recombination rate.

Son *et al.* [8] reported a room temperature IQE of 43 % for a 3-period $In_{0.08}Ga_{0.92}N$/ $In_{0.02}Ga_{0.98}N$ QW structure containing a 100 nm thick $In_{0.02}Ga_{0.98}N$ UL, compared to 14 % for an identical 3 QW structure without an UL. The room temperature PL lifetimes of the structures were measured to be 65 and 13 ns, respectively. This was concluded to be as a result of the increased separation of the active region from the growth interruption interface.

Armstrong *et al.* [9] performed EL measurements on two $In_{0.16}Ga_{0.84}N$/GaN sin-

gle QW LEDs, one containing a Si-doped $In_{0.03}Ga_{0.97}N$ UL and one without. An approximately 5 times greater peak EQE was reported for the UL-containing LED compared with the LED with no UL, as well as a reduction in the rate of non-radiative recombination by a factor of 3.9. Optical measurements were performed with a varying excitation energy to probe defect states within the bandgap. The presence of an absorption band at 1.62 eV below the CB was found to be reduced by 3.4 times in the sample with the UL, and so a defect state associated with that energy was concluded to be the main non-radiative recombination centre in the LEDs studied. The authors claimed additionally that In atoms arriving on the growth surface are incorporated at that interface and so "bury" impurities at the growth interruption interface when the UL growth is commenced.

4.2.2 Strain Reduction

The large difference in lattice parameter between InN and GaN means that compressive strain is induced when InGaN QWs are grown on GaN barriers [5, 6, 10]. This strain leads to a large piezoelectric polarisation field across the QW region, as described in Chapter 2, resulting in a reduction of the radiative recombination rate due to the QCSE. These effects are particularly detrimental in LEDs and QW structures which emit light in the green region of the visible spectrum due to the higher QW In fractions compared with blue light emitters. Some authors have claimed that InGaN ULs (or InGaN/GaN superlattices) act to relieve strain in InGaN/GaN QW structures by improved lattice matching of the QW material to the UL than to pure GaN [5, 6, 10].

Blue shifted emission was reported for InGaN/GaN MQW structures and LEDs containing InGaN ULs, relative to structures without ULs, in work carried out separately by Nanhui *et al.* [5] and Törmä *et al.* [6]. In both cases, this was assigned to a reduction in the strain in the QW leading to a reduced QCSE. Nanhui *et al.* [5] also

reported a reduced blue shift with increasing injection current for LEDs containing ULs. This was claimed to be a result of reduced strain-induced electric fields across the QWs, meaning that less charge carrier screening of these electric fields occurred. Both groups also performed atomic force microscopy (AFM) measurements on their samples and demonstrated a reduced density of V-pits on the surface of the structures containing ULs. V-pits, which are inverted hexagonal pyramid-shaped pits (Figure 4.1), have been shown to occur at the surface of layers of InGaN grown on GaN as a result of threading dislocations which propagate through the entire structure [26, 27]. Nanhui *et al.* [5] and Törmä *et al.* [6] claimed that strain relaxation occurred in their high In fraction QWs, leading to the formation of threading dislocations. The reduced V-pit density was therefore concluded to be caused by reduced strain in the structures with ULs, resulting in a reduced threading dislocation density in the QWs.

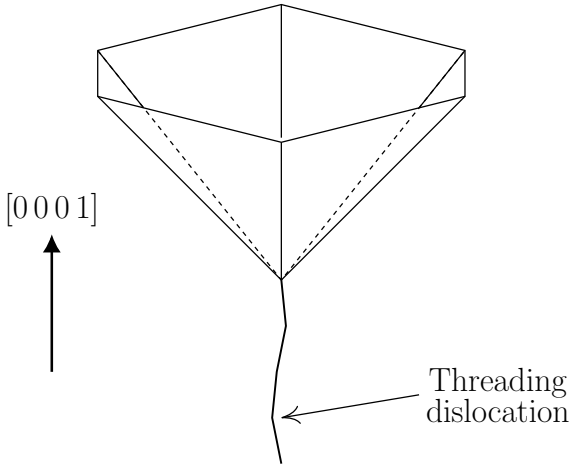

Figure 4.1: Schematic diagram of a V-pit shown at the top of a threading dislocation. The growth direction ([0 0 0 1], or *c*) is labelled. Adapted from Chen *et al.* [26].

Recently, Shan *et al.* [10] demonstrated an improvement in the conversion efficiency of an InGaN/GaN MQW solar cell following the inclusion of a 10-period $In_{0.04}Ga_{0.96}N$/GaN superlattice grown before the active region. Raman spectroscopy measurements gave a small reduction in wavenumber for the E_2 LO phonon peak for the InGaN/GaN structure with the superlattice UL compared to the one without. This was related to

a reduction in strain in the layers, which was given as the reason for the improved efficiency.

4.2.3 Promotion of V-Pits

Takahashi *et al.* [7] compared the optical and structural properties of several single InGaN/GaN QW structures with various threading dislocation densities grown in pairs with and without a GaN UL. The structures were capped with AlGaN layers. The UL was grown at a lower temperature than the QWs and barriers and was intended to lead to the formation of V-pits that were large enough to penetrate the QW due to the increased total thickness of the structure. This was based on the work of Chen *et al.* [26], who reported that the density of V-pits on the surface of layers of InGaN grown on GaN increased with increasing In composition fraction in InGaN layers, and the pit diameter was observed to increase as the total thickness of the grown InGaN/GaN QW structure was increased. The PL peak intensity at room temperature was consistently found to decrease as the threading dislocation density increased, and was said to be due to non-radiative recombination at these defects. However, the PL peak intensity of structures containing ULs was always higher than for the equivalent structure without an UL for a given threading dislocation density and excitation power density. The PL peak intensity at 77 K showed little variation between equivalent structures with and without ULs, and so it was concluded that the differences in PL intensity observed at room temperature must be due to a reduction in the number of carriers reaching threading dislocations. It was claimed that the AlGaN cap layer fills the V-pit and reduces the number of threading dislocations in contact with the QW. Large V-pits were therefore said to be beneficial to the emission properties of InGaN/GaN QWs, and it was the inclusion of an UL that promoted their creation.

4.2.4 Electron Reservoir Layer

In work by Takahashi *et al.* [3] and Otsuji *et al.* [4], InGaN/GaN MQW LEDs with and without an $In_{0.18}Ga_{0.82}N$ UL were investigated. The UL was doped with Si at a density of $\sim 10^{19}\,cm^{-3}$. It was found that the turn-on voltage was lower for the LED with the UL compared to the one without at both 20 and 300 K. An emission band on the high energy side of the MQW emission spectrum was attributed to recombination in larger bandgap semipolar material around defects based on work by Hangleiter *et al.* [28]. The intensity of this band relative to the main MQW emission was observed to be reduced in the sample with the UL. These results were said to be because the *n*-type UL acts as an "electron reservoir layer", leading to improved electron capture by the QWs and so reducing the proportion of carriers that recombine both radiatively and non-radiatively at defects.

4.2.5 Surface Depletion Field

As shown in Chapter 2, the group III-nitrides feature large spontaneous polarisation fields in the [0 0 0 1] crystal direction [16]. In the case of InGaN/GaN QWs grown along this direction, the spontaneous polarisation field acts in the opposite direction to the piezoelectric polarisation fields caused by strain in the InGaN QW layers grown on GaN [16]. It was shown by Fiorentini *et al.* [16] that a potential drop exists across a bulk layer of a homogeneous, unstrained group III-nitride material due to the spontaneous polarisation charges formed at the opposite interfaces of the layer, which are terminated by group III and N atoms, respectively. This potential drop increases linearly with layer thickness, d, resulting in a constant electric field, $|\mathbf{F}|$, referred to as the surface depletion field. When this potential drop approaches the bandgap potential at a certain critical thickness, d_c, the Fermi level approaches the VB and CB edges at the group III and N atom terminated interfaces, respectively, leading to the generation of a large density of holes and electrons in these respective

regions. These carriers partially screen the polarisation charges, which means that the potential drop is limited to the bandgap potential. This means that, for $d > d_c$, the electric field due to the spontaneous polarisation is given by [16]

$$|\mathbf{F}| = \frac{E_{\mathrm{G}}}{d}, \tag{4.1}$$

where E_{G} is the bandgap energy of the material.

Mayrock *et al.* [17] demonstrated that the background n-type doping usually present in group III-nitrides leads to an additional pinning of E_{F}. When the n-type dopant density is sufficiently high, E_{F} is pinned at the CB edge and $|\mathbf{F}|$ is effectively zero in this region. The resultant band bending confines the surface depletion field to the extreme edges of the structure, and so the magnitude of the electric field close to the group III atom-terminated surface can be manipulated by varying the n-type dopant density as shown for a bulk GaN layer in Figure 4.2 from Mayrock *et al.* [17].

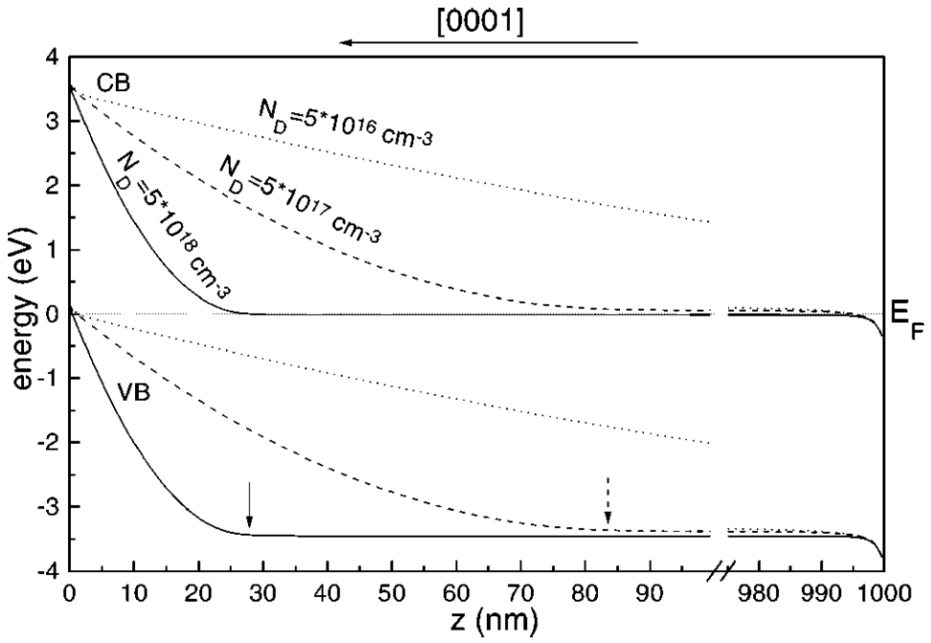

Figure 4.2: CB and VB varying with position, z, within a bulk GaN layer. The Ga-terminated layer is at $z = 0$ while the N-terminated layer is at $z = 1000\,\text{nm}$. Bands are calculated for different n-type doping densities, N_D. Arrows indicate the edge of the surface depletion field region for different values of N_D. The energy scale is defined with the Fermi level, E_F, at zero. Reprinted figure with permission from Mayrock *et al.* [17]. Copyright 2000 by the American Physical Society.

The effect of this band bending on QW structures was investigated experimentally by Monemar *et al.* [18], who performed PL spectroscopy measurements on GaN/ AlGaN MQWs with different Si doping densities in the QW barriers. The MQW PL emission peak was reported to broaden with increasing Si doping density. This was attributed to some of the QWs being well within the surface depletion region and some being in the region with flatter bands. This would mean that the total electric fields would vary between different QWs in one structure, resulting in different recombination energies due to the different magnitudes of the QCSE. The observed broad emission was therefore due to emission from several QWs with different peak energies.

Evidence of the surface depletion field was also observed by Netzel *et al.* [15], who performed PL spectroscopy measurements on a single $In_{0.08}Ga_{0.92}N/In_{0.02}Ga_{0.98}N$ QW structure grown on top of a 300 nm thick GaN UL which was doped with Si to

a density of $5 \times 10^{17}\,\mathrm{cm}^{-3}$. On top of the QW, a 100 nm thick undoped GaN cap layer was grown. Part of this layer was then etched with a sloping etch depth profile, shown schematically in Figure 4.3. PL spectra were recorded at room temperature for various positions of the excitation beam along the sloping surface of the structure. The QW PL emission energy was reported to increase by 95 meV as the thickness of the GaN capping layer was reduced from 30 nm to zero. The FWHM of the emission peak also fell by 60 meV over this region. Both of these effects were concluded to be due to the decreasing total electric field across the QW as the strength of the surface depletion field increases with decreasing capping layer thickness. In the case of the reduction of the peak FWHM, this conclusion was based on work that showed that QWWFs lead to a broadened PL emission peak and that their effect is enhanced by the piezoelectric fields across the QWs [29, 30].

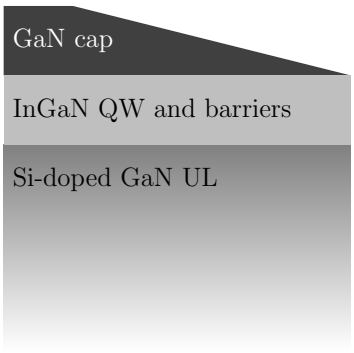

Figure 4.3: Schematic diagram of the QW structure containing a Si-doped GaN UL and a GaN cap layer with a sloping etch depth profile investigated by Netzel *et al.* [15].

It was proposed by Davies *et al.* [12] that the main effect of *n*-type ULs in InGaN/GaN QW structures is to provide the Fermi level pinning that leads to the surface depletion field effects described above. To investigate this, the authors compared four $In_{0.16}Ga_{0.84}N$/GaN single QW structures: one structure featured a 24 nm thick $In_{0.05}Ga_{0.95}N$ UL doped with Si to a density of $5 \times 10^{18}\,\mathrm{cm}^{-3}$, two structures featured GaN ULs doped with Si to the same density and grown at 770 °C and 1020 °C, respectively, and one had no UL. In PL spectroscopy measurements performed at 10 K,

the QW peak emission energies for the structures with ULs were blue shifted relative to the structure without an UL. The largest blue shift was observed for the structure with the $In_{0.05}Ga_{0.95}N$ UL. PL time decay measurements showed that the time taken for the peak PL intensity to fall by one order of magnitude was 101 ns faster for the structure with the GaN ULs, and 111 ns faster for the structure with the $In_{0.05}Ga_{0.95}N$ UL, compared with the structure with no UL. Since the PL emission peak energies and decay times of the structures with GaN ULs were essentially the same, effects due to V-pit propagation caused by the lower growth temperature for the UL in one of the structures were ruled out. The blue shifted QW peak emission energy and shorter PL lifetime were instead attributed to the reduced QCSE in the structures with ULs caused by the *n*-type doping in the ULs leading to an enhanced surface depletion field. An additional reduction in the total electric field across the QW was identified in the sample with the $In_{0.05}Ga_{0.95}N$ UL as being due to the polarisation discontinuity between the top layer of $In_{0.05}Ga_{0.95}N$ in the UL and the bottom layer of GaN in the bottom QW barrier. The charged interface formed here would be of opposite sense to the one formed at the bottom interface of the QW and so the resultant electric field across the QW was reduced further than in the structures with Si-doped GaN ULs. This additional reduction in the QCSE accounted for the additional blue shift and shorter lifetime of the PL peak for the structure with the $In_{0.05}Ga_{0.95}N$ UL. Later studies by the same authors demonstrated that the additional effect of In in the UL only affects the bottom QW, closest to the UL, in a 10 QW structure [13, 14]. A reduced QCSE would lead to an increased radiative recombination rate, and so it was concluded that the surface depletion field would lead to the increased IQE observed in QW structures with ULs.

The effects of the surface depletion field described in this section do not apply to LEDs under bias. An LED features a *p*-type layer grown on top of the topmost QW-barrier period. Under zero bias, this leads to a Fermi level pinning close to the VB edge in the *p*-type region and so a depletion field similar to that described above

is present across the QW stack (the Fermi level is pinned at the CB edge in the n-type layer as in the case of n-type ULs) [18, 31]. The band bending occurs here because the Fermi level is constant across the structure when it is in equilibrium. However, when the LED is under bias, the system is no longer in equilibrium and the Fermi levels for electrons and holes shift relative to each other, removing the depletion field. Despite this, the effect of the surface depletion field remains an important factor to consider in investigations where PL measurements are performed, and should not be discounted in favour of other mechanisms for IQE improvements due to ULs since this parameter is often determined by optical excitation.

4.3 Effects of Number of Quantum Wells on Internal Quantum Efficiency

The works described in Section 4.2.5 suggest that, in order to maximise the increase in radiative recombination rate due to the reduced net electric field across a QW, the depth of the surface depletion region (that is, the depth of the UL in the structure) must be minimised. A lower limit will therefore be placed on the depth of the surface depletion region for a given number of QWs.

It was shown by Thucydides *et al.* [21] that the rate of thermionic emission of carriers from a GaAs/AlGaAs single QW increases with increasing temperature. Hurst *et al.* [19] observed that the room temperature IQE of a series of InGaN/GaN MQW structures increased with increasing number of QWs, and suggested that carriers which escape from a QW by thermionic emission can subsequently be recaptured by other QWs. The rate of carrier escape by thermionic emission from the entire MQW system therefore decreases with increasing number of QWs, leading to higher overall efficiencies. An increasing IQE with increasing number of QWs was also reported by Minsky *et al.* [20], who suggested an alternative explanation to that of Hurst *et al.* [19].

The authors observed that the PL decay time of a single InGaN/GaN QW decreased rapidly with increasing temperature, but that this effect was reduced as the number of QWs was increased, and suggested that impurity incorporation at interfaces was reduced with the growth of successive layers (as reported in GaAs/AlGaAs QWs by Dawson and Woodridge [22] and Rimmer *et al.* [23], described in Section 4.2.1). The weakening temperature dependence of the PL decay time as the number of QWs was increased was therefore attributed to the gettering of thermally activated interface states, leading to an increasing IQE.

Varying the number of QWs in a structure should therefore have the competing effects of increasing the net electric field across the QWs, resulting in a reduced electron-hole wavefunction overlap, and reducing non-radiative carrier losses due to thermionic emission and/or recombination at interface defect states. This competition is the subject of study in this chapter, in which the results of PL investigations into MQW structures with different numbers of QWs are presented with the aim of establishing which parameter (electron-hole wavefunction overlap or number of QWs) has the dominant effect on the room temperature IQE of a structure.

4.4 Sample Details

Six InGaN/GaN QW samples containing ULs were grown for these investigations by colleagues at the Department of Materials Science and Metallurgy, University of Cambridge, using the 2T growth method [32]. The samples were grown on top of 5 µm thick GaN pseudo-substrates on sapphire. For all of the samples, a 2 µm thick GaN:Si template with nominal doping density $5 \times 10^{18}\,\mathrm{cm}^{-3}$ was grown followed by a 23 nm $In_{0.05}Ga_{0.95}N$:Si UL with the same nominal doping density. On top of the UL, a 3 nm layer of undoped GaN was grown followed by the QW(s) and barriers(s). The number of QW-barrier periods was varied between 1 and 15. The QW widths, In fractions and barrier thicknesses were determined by X-ray diffraction (XRD) measurements.

AFM measurements showed no systematic variation in the density of V-pits on the surfaces of the samples. All structural characterisation was performed at Cambridge. All of the QW widths in all of the samples were measured to be (2.3 ± 0.1) nm. The other sample parameters are summarised in Table 4.1.

Table 4.1: Summary of the number of QWs, In composition and barrier thicknesses of each of the samples containing ULs.

Sample Number	Number of QWs	QW In Fraction (%)	QW Barrier Thickness (nm)
C5978A	1	8 ± 1	7.0 ± 0.1
C5977A	3	11 ± 1	7.2 ± 0.1
C5976A	5	12 ± 1	7.0 ± 0.1
C5980A	7	12 ± 1	7.0 ± 0.1
C5979A	10	12 ± 1	7.0 ± 0.1
C5983A	15	12 ± 1	6.9 ± 0.1

4.5 Simulation of the Conduction and Valence Band Profiles

The modelling of the energy bands for the samples was performed using the commercially available device simulator nextnano^3 [33]. An input file was created for each structure which contained the experimentally determined details of the materials and their widths for each layer in the structure. The nextnano^3 package includes a database of parameters for many materials, including the group III-nitrides. From these parameters the homogeneous strain, followed by the spontaneous and piezoelectric polarisation fields, were calculated for the structure specified in the input file using the theory described in Chapter 2.

In the sample input files, it was specified that the lattice temperature was 10 K and that the structures were grown pseudomorphically (that is, fully strained) on a GaN template. Si was included as an impurity at the nominal concentration $(5 \times 10^{18}\,\mathrm{cm}^{-3})$

by specifying an n-type dopant with an activation energy of 30 meV [34] in the input files.

It is important to consider the limitations of this type of model: the QWs are treated as 1-dimensional structures where the In atoms are uniformly distributed in the InGaN alloy. The model therefore neglects alloy disorder and QWWFs which are known to have many important effects on the absorption and emission properties of InGaN/GaN QWs, as described in Chapter 2. For this reason, the CB and VB profiles calculated using nextnano^3 should only be interpreted as a guide to any relative differences in observations between samples and not relied on to match experimentally determined parameters such as the PL emission energy of a QW. Fully atomistic models which take into account the microstructural properties of these systems are unnecessary for the conclusions drawn in this chapter.

4.6 Results and Discussion

4.6.1 Simulation Results

The simulated CB and VB profiles for the sample series, calculated using nextnano^3 using the parameters given in Section 4.4, are shown in Figure 4.4. The position axis is defined with the positive (growth) direction towards the sample surface where zero is set at the interface between the UL and the bottom QW barrier. The energy axis is defined with the Fermi level at zero.

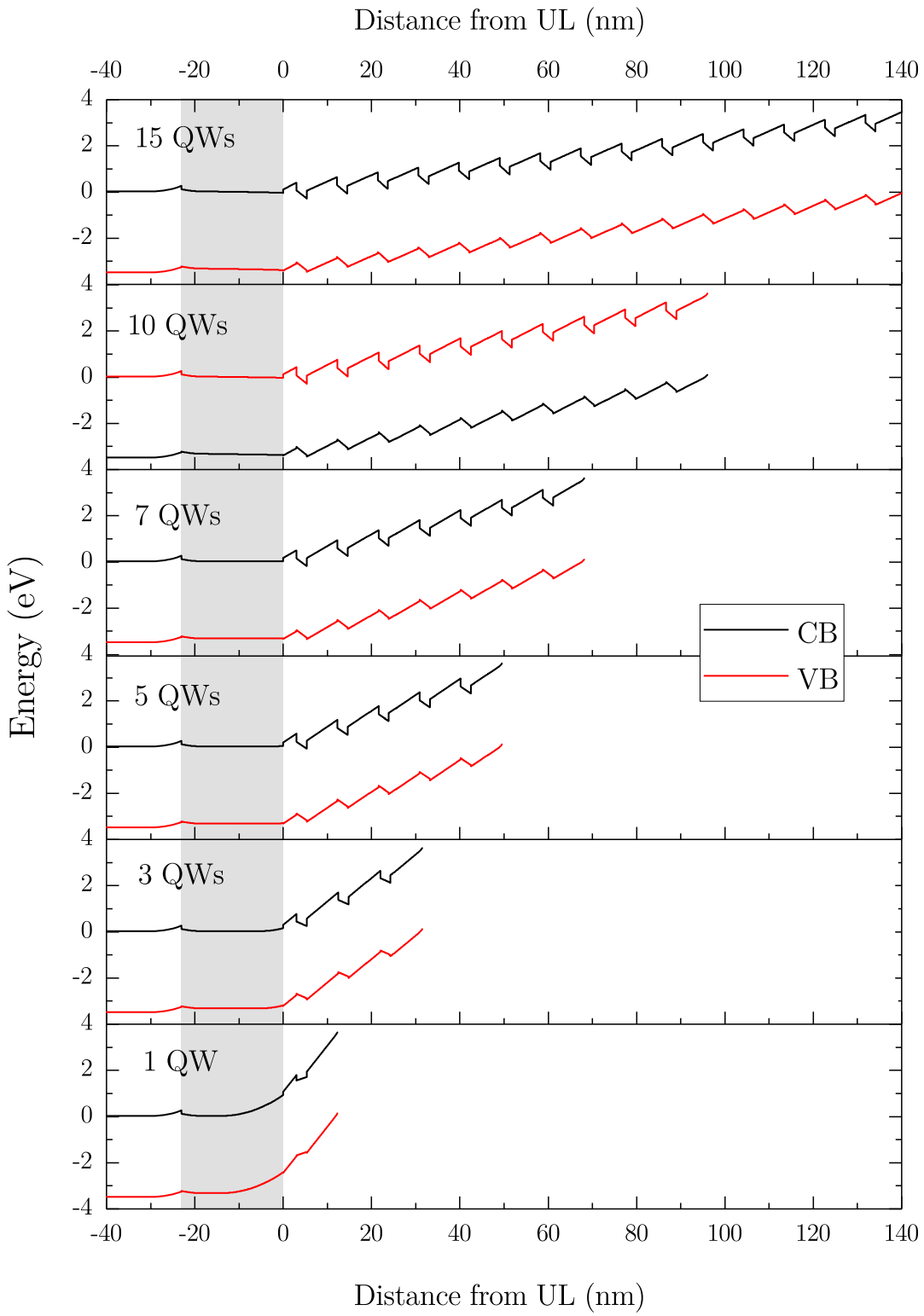

Figure 4.4: Calculated CB and VB profiles for the structures containing ULs with the number of QWs indicated. The UL is marked by the shaded area.

As was reported by Davies *et al.* [12–14], the Fermi level is pinned at the CB edge in the region of the UL and at the VB edge at the sample surface for the reasons described in Section 4.2.5. The strength of the resulting surface depletion field, corresponding to the overall gradient between these points, decreases with increasing number of QWs. The electric fields across each QW for each of the samples were measured from the simulated band profiles and are plotted in Figure 4.5, where the QW number increases with distance from the UL. The electric field for the 1 QW sample is negative to indicate that it is in the opposite direction to that in the rest of the samples.

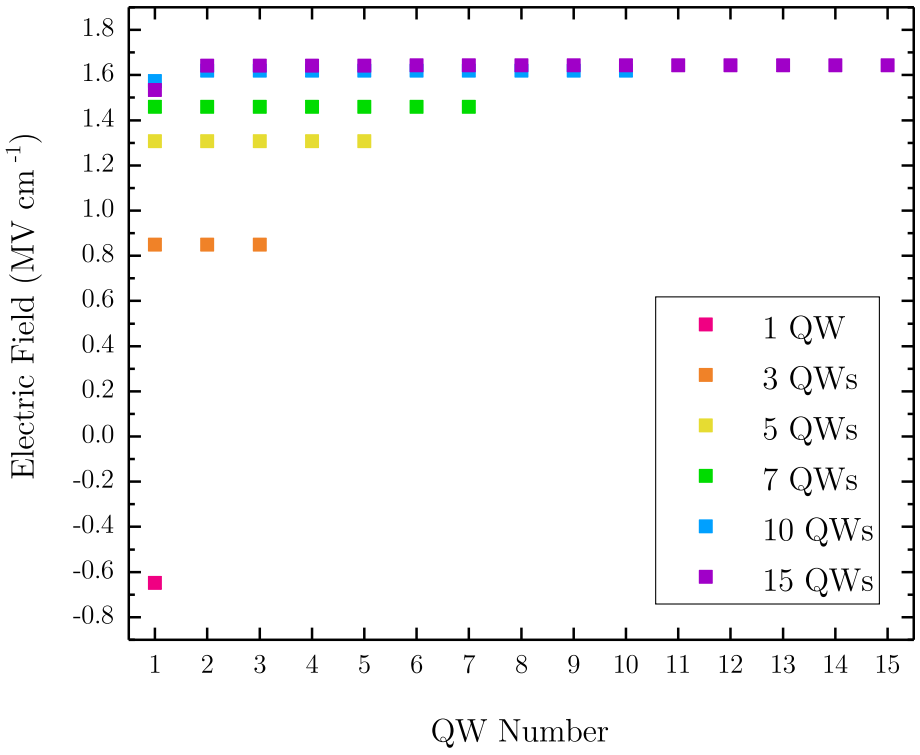

Figure 4.5: Electric fields across individual QWs for each of the samples containing ULs, determined from the simulated band profiles.

The mean electric field across the QWs increases sub-linearly with increasing number of QWs (Figure 4.6), varying from $-0.608\,\mathrm{MV\,cm^{-1}}$ for the 1 QW sample to $1.64\,\mathrm{MV\,cm^{-1}}$ for the 15 QW sample. For all of the QWs in all of the samples with more than 1 QW, apart from the first QW in the 10 and 15 QW samples, the electric field strength varies by less than 1 % between the QWs for a particular sample. For

the 10 QW and 15 QW samples, the electric field across the first QW in the stack is reduced relative to the second QW by 0.0468 and 0.108 $\mathrm{MV\,cm^{-1}}$, or 2.9 and 6.6 %, respectively. This is due to an additional sheet charge that occurs at the $In_{0.05}Ga_{0.95}N$/GaN interface between the UL and the first QW barrier due to the large polarisation discontinuity between the two layers, and which is of opposite sense to the sheet charge formed at the GaN/InGaN interface at the bottom of the first QW in the stack [12–14]. In the cited works, a 10 QW structure with a Si-doped InGaN UL was reported to exhibit a high energy-broadened PL spectrum when compared to a similar structure with no UL. This broadening was shown in PL excitation measurements to be due to a feature with a higher absorption energy than the main QW peak. The temperature dependence of the PL decay time across the emission spectrum was also reported to be different for the high energy side of the QW peak for the structure with the UL. This feature was therefore attributed to the QW closest to the UL which would have a higher emission energy and shorter PL decay time compared with the other QWs in the sample due to the reduced QCSE as a result of the effect described above. No obvious feature was observed on the high energy side of the PL emission spectra for the 10 and 15 QW samples in this chapter, but PL excitation experiments and temperature dependent PL time decay measurements would be necessary to investigate this further. The reduction in electric field strength for the bottom QW was reduced by approximately 12 % relative to the other QWs for the 10 QW sample studied by Davies *et al.* [13, 14], which is a larger reduction than that calculated for the 15 QW sample studied in this work. It may be that a smaller difference in emission energy for 1 QW is not resolvable from the total emission from the other 14 QWs in the PL experiments reported in this thesis.

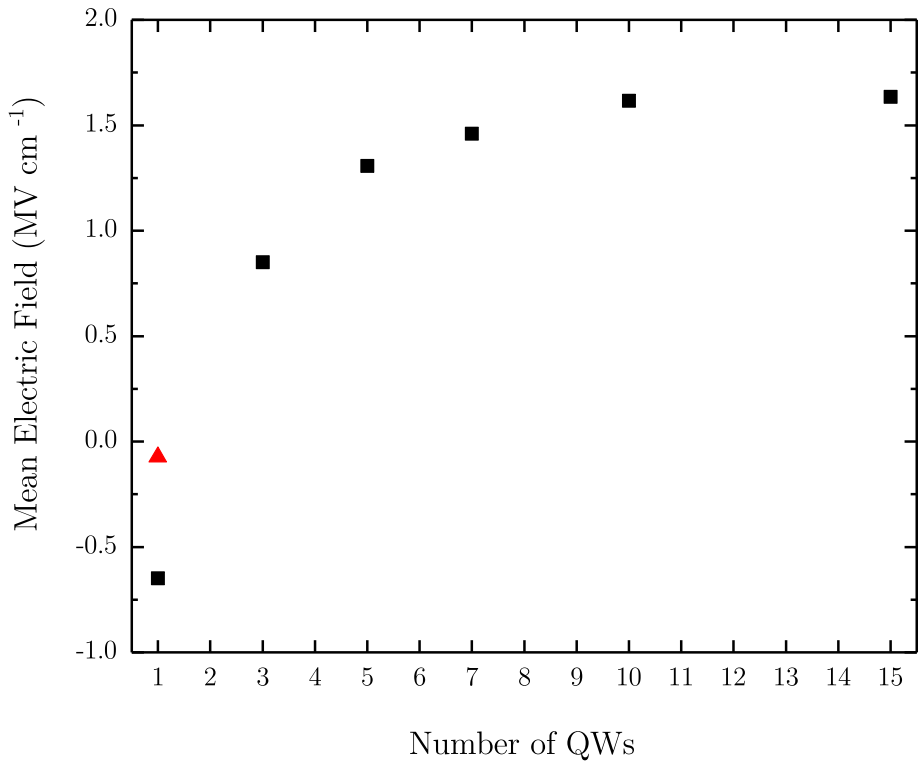

Figure 4.6: Mean electric fields across the QWs for all of the samples containing ULs, measured from the simulated band profiles. The red triangle corresponds to the electric field for a hypothetical 1 QW sample where the QW In fraction has been matched to that of the 3 QW sample.

The In composition fraction of the QW in the 1 QW sample is significantly reduced compared with the rest of the samples in the series; as shown in Section 4.4, the measured In fractions of the QWs in the 1 QW and 3 QW samples are $(8 \pm 1)\,\%$ and $(11 \pm 1)\,\%$, respectively. The reduced In fraction in the 1 QW sample means that a reduced contribution from the strain-induced piezoelectric field can be expected across the QW as a result of better lattice matching of the lower In fraction InGaN to the GaN barriers. This would be in addition to the net field reduction effect provided by the surface depletion field. To be sure that the reduced QW In fraction does not provide the dominant contribution to the net electric field reduction for the 1 QW sample relative to the 3 QW sample, energy band profiles were calculated using nextnano[3] for a hypothetical structure identical to the 1 QW sample but with the alloy composition modified to match that of the QWs in the 3 QW sample. The CB energy

profile for this hypothetical structure is shown along with that of the real sample in Figure 4.7. From this, the electric field across the 11 % In QW was determined to be $-0.074\,\mathrm{MV\,cm^{-1}}$. This value is plotted in Figure 4.6 as a red triangle. The change in the magnitude of the QW electric field strength between this value and the mean value for the 3 QW sample is $0.776\,\mathrm{MV\,cm^{-1}}$. (The change in the magnitude of the electric field strength is important as the QCSE is present regardless of the sign of the field.) This is greater than the change between the 3 QW sample and the 5 QW sample ($0.458\,\mathrm{MV\,cm^{-1}}$). These results show that the UL provides a major contribution to the change in net electric field between the 1 and 3 QW samples and that it must be accounted for in the interpretation of experimental results.

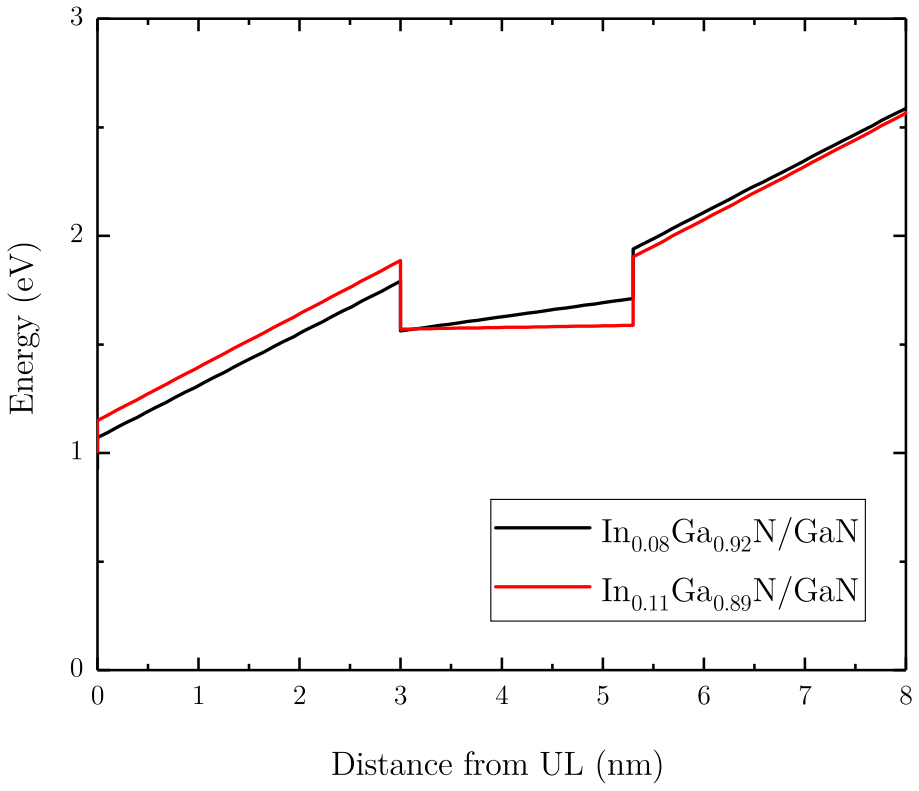

Figure 4.7: Comparison between the nextnano[3] calculated CB energy profiles for the real 8 % In 1 QW sample and the hypothetical 11 % In structure.

4.6.2 Low Temperature Photoluminescence Spectroscopy

PL spectra obtained at 10 K using CW excitation at 3.185 eV, with a power density at the sample of 15 W cm^{-2}, are shown for each sample in Figure 4.8. Two main spectral peaks are identified for all of the samples in this detection range: one with a peak energy at around 3.28–3.29 eV and another in the range 2.74–2.79 eV. The FWHM of the lower energy peak, attributed to radiative recombination in the QW(s), is between 110–160 meV for all of the samples. An additional peak with lower intensity is observed on its low energy side at an energy separation of ∼90 meV and is attributed to LO phonon-assisted recombination of electrons and holes [35–37]. The higher energy peak is due to the $In_{0.05}Ga_{0.95}N$:Si UL, as its emission energy lies just below the expected bandgap of $In_{0.05}Ga_{0.95}N$, which was calculated using Vergard's law to be 3.307 eV at 0 K. The PL intensities in Figure 4.8 have been normalised to the peak of the QW emission feature. Residual Fabry-Pérot oscillations are visible across all of the spectra.

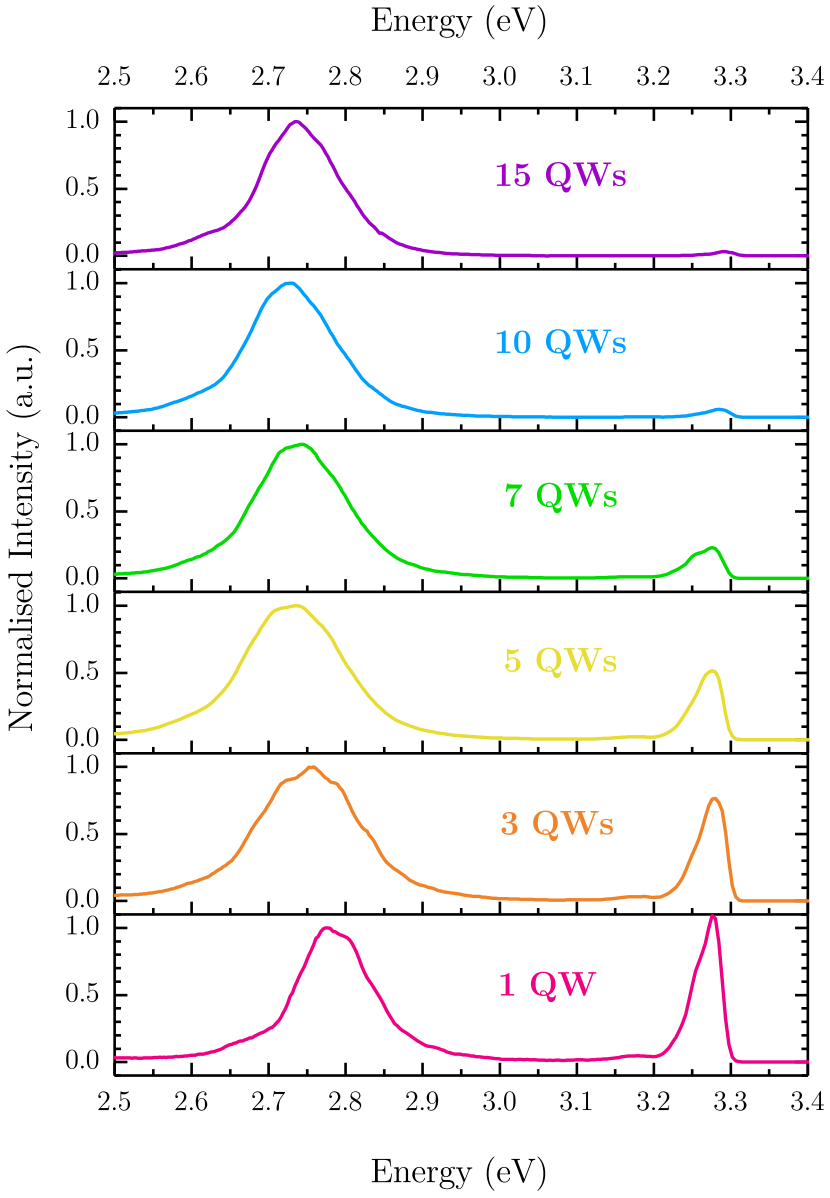

Figure 4.8: Normalised PL spectra at 10 K for the samples containing ULs. PL intensities are normalised to the peak of the QW emission feature. The number of QWs is as indicated on each spectrum.

The integrated intensity of the UL emission peak relative to that of the QW peak decreases exponentially as the number of QWs in the sample is increased, as shown in the semi-logarithmic plot in Figure 4.9. This observation is attributed to the fact that the total amount of absorbing material (specifically GaN) between the point at which the excitation beam enters the sample (the surface) and the UL increases as the number of QWs is increased. The number of photons per second arriving in the

region of the UL therefore decreases as the depth of the UL increases, in accordance with the Beer-Lambert law. This assumes no carrier transfer between the QWs and the UL in a particular sample.

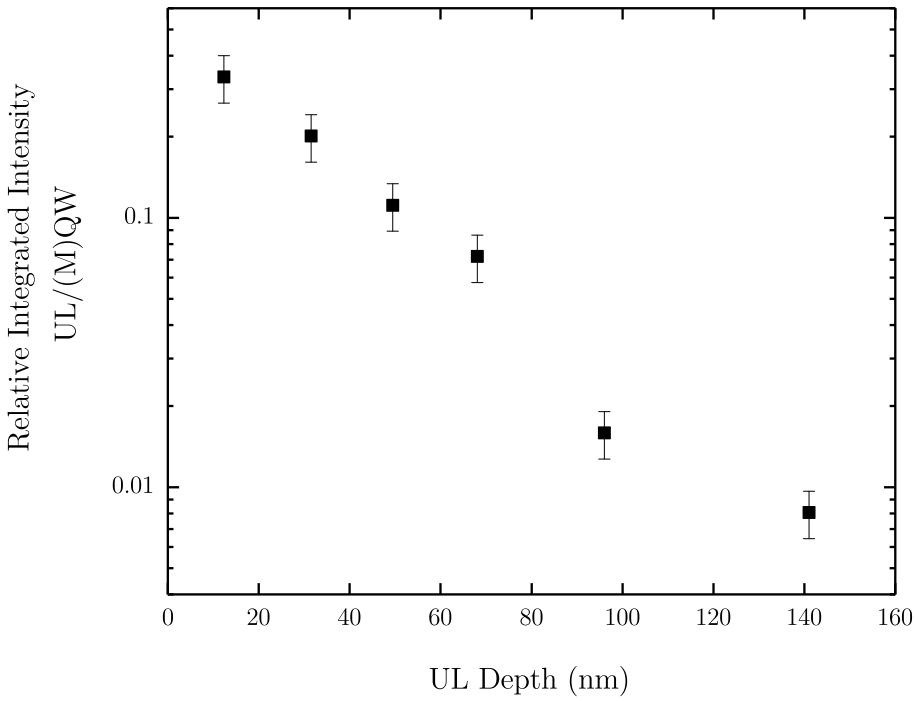

Figure 4.9: Relative integrated intensity of the UL emission peak to that of the QW peak varying with UL depth.

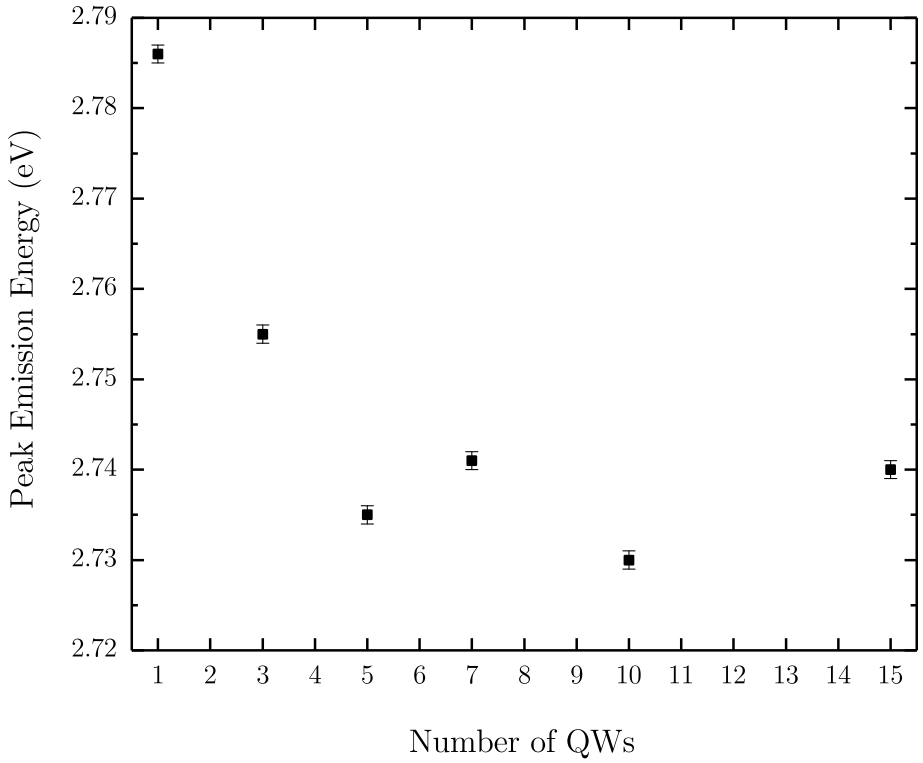

Figure 4.10: QW peak PL emission energy varying with number of QWs.

Overall, the peak PL emission energy of the QW feature at 10 K, plotted in figure 4.10, red shifts by (56 ± 2) meV as the number of QWs is increased from 1 to 10. As the magnitude of the electric field strength across the QWs decreases with increasing number of QW periods, this red shift is attributed to the increasing magnitude of the QCSE as the strength of the surface depletion field decreases. The red shift between the peak emission energies of the 1 QW and 3 QW samples is partly due to the change in bandgap energy between the two samples. The lower In fraction of the 1 QW sample results in a larger bandgap and so a higher energy emission peak. However, as shown in Section 4.6.1, the change in net electric field between the 1 and 3 QW samples would be larger than that between the 3 and 5 QW samples even if the In fractions were identical. Therefore, a red shift in emission peak energy between the 1 and 3 QW samples would still be expected if this were the case.

The peak emission energy for the 15 QW sample was measured to be (10 ± 2) meV higher than that for the 10 QW sample. From the simulated band profiles, which were

calculated for fully strained QWs, a lower energy emission peak for the 15 QW sample relative to the 10 QW sample would be expected due to the slightly higher mean electric field across the QWs. It has been shown that strain relaxation can occur in low In fraction InGaN/GaN MQW structures with around 10 or more QWs [38, 39]. It is therefore possible that strain relaxation has occurred in the 15 QW sample, in which case the mean electric field across the QWs would be reduced. This would lead to a reduced QCSE giving a higher emission peak energy than for the fully strained case. The reason for the higher energy emission from the 7 QW sample relative to the 5 QW sample is currently unclear.

4.6.3 Photoluminescence Time Decay Measurements

PL time decay measurements were performed on each of the samples. Assuming that one electron-hole pair was generated for each photon incident on the sample, the excited carrier density was estimated to be $\sim 10^{12}\,\mathrm{cm}^{-2}\,\mathrm{pulse}^{-1}$. The PL time decay curves detected at the peak of the QW emission for each sample are shown in Figure 4.11. As discussed in Chapter 2, PL decay curves for polar InGaN/GaN QWs are non-exponential at low temperatures. Therefore, the time taken for the PL intensity to reach $1/e$ of its peak value, denoted by $\tau_{1/e}$, is used as an arbitrary measure of the decay time and is shown varying with the number of QWs in Figure 4.12. At 10 K, the value of $\tau_{1/e}$ is assumed to be governed entirely by radiative recombination [40].

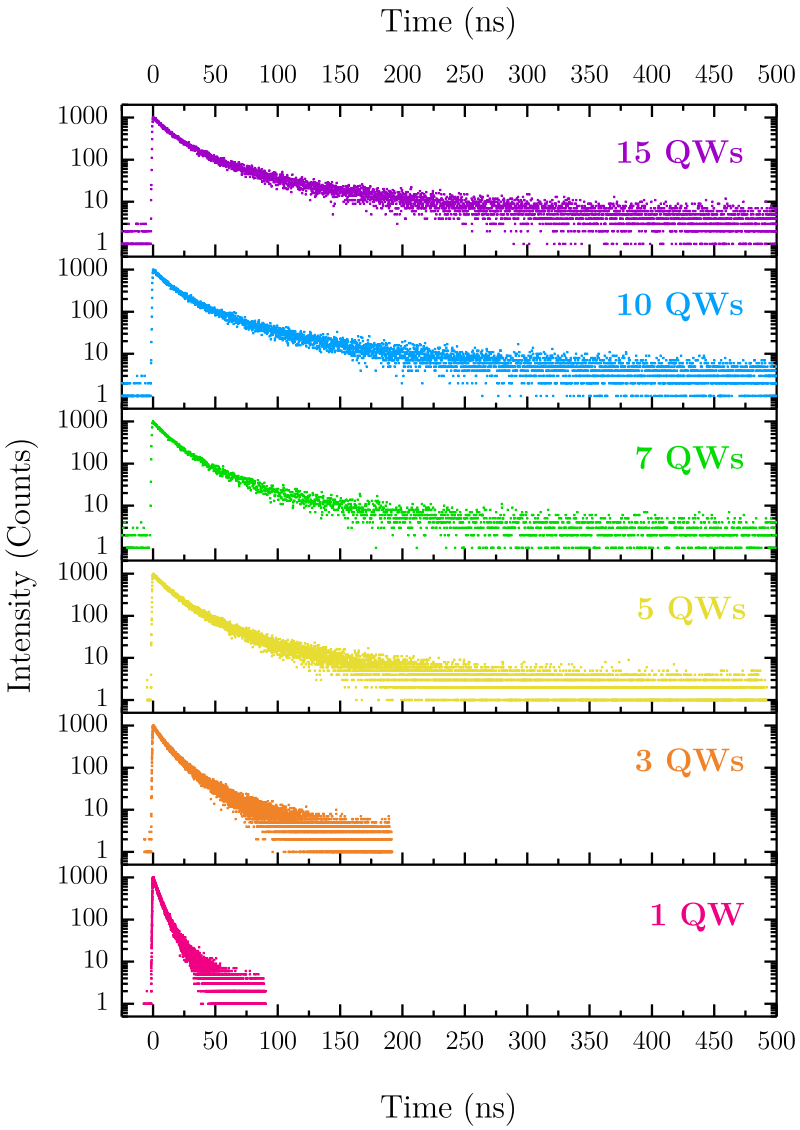

Figure 4.11: PL decay curves detected at the QW peak emission energy for the samples containing ULs. The number of QWs is as indicated.

In general, a trend of sub-linearly increasing PL decay time with increasing number of QWs is observed. This agrees with the variation in electric field strength across the QWs determined from the calculated energy band profiles. That is, the mean strength of the electric field across the QWs increases with increasing number of QW periods as the strength of the surface depletion field is reduced. This causes the electron-hole wavefunction overlap to decrease, resulting in a decreasing radiative recombination rate. The reason for the lack of an increase in $\tau_{1/e}$ between the 5 and 7 QW samples

is unclear. It may be related to the anomalous peak emission energy shift described in Section 4.6.2.

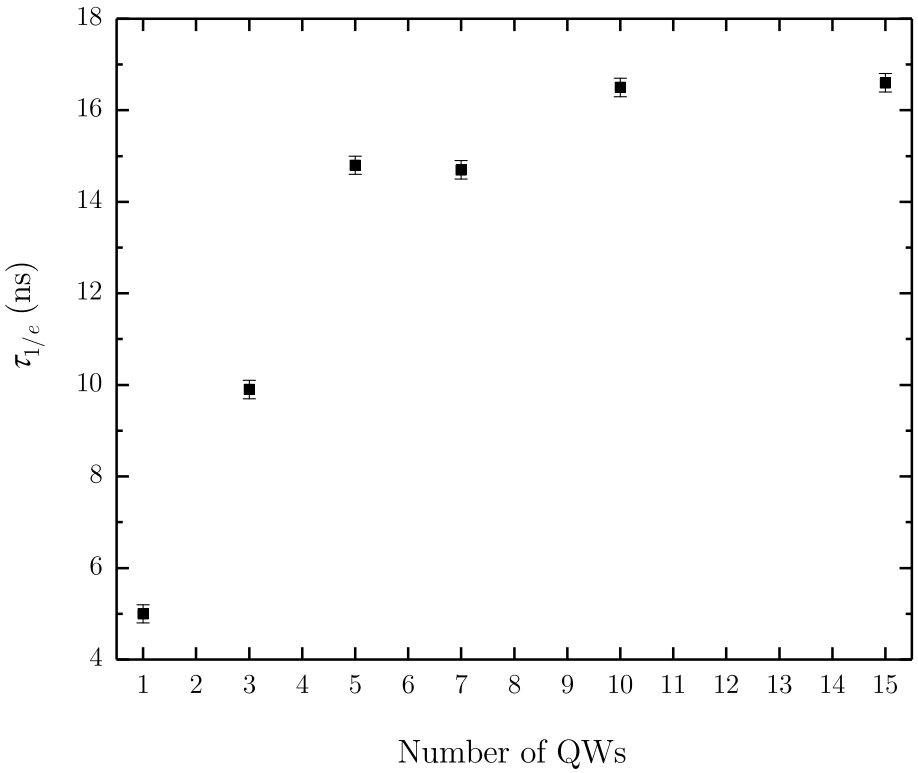

Figure 4.12: Variation of $\tau_{1/e}$ with number of QWs.

4.6.4 Temperature Dependent Photoluminescence Spectroscopy

Temperature dependent PL spectroscopy was performed using CW excitation above the bandgap energy of the GaN barriers for each of the samples at an excitation power density of $15\,\mathrm{W\,cm^{-2}}$. A selection of the PL spectra taken over the temperature range 10–300 K are shown for the 1 QW sample in Figure 4.13. The detection range was selected to include both the QW and the UL peaks for all of the samples. These peaks are labelled in Figure 4.13.

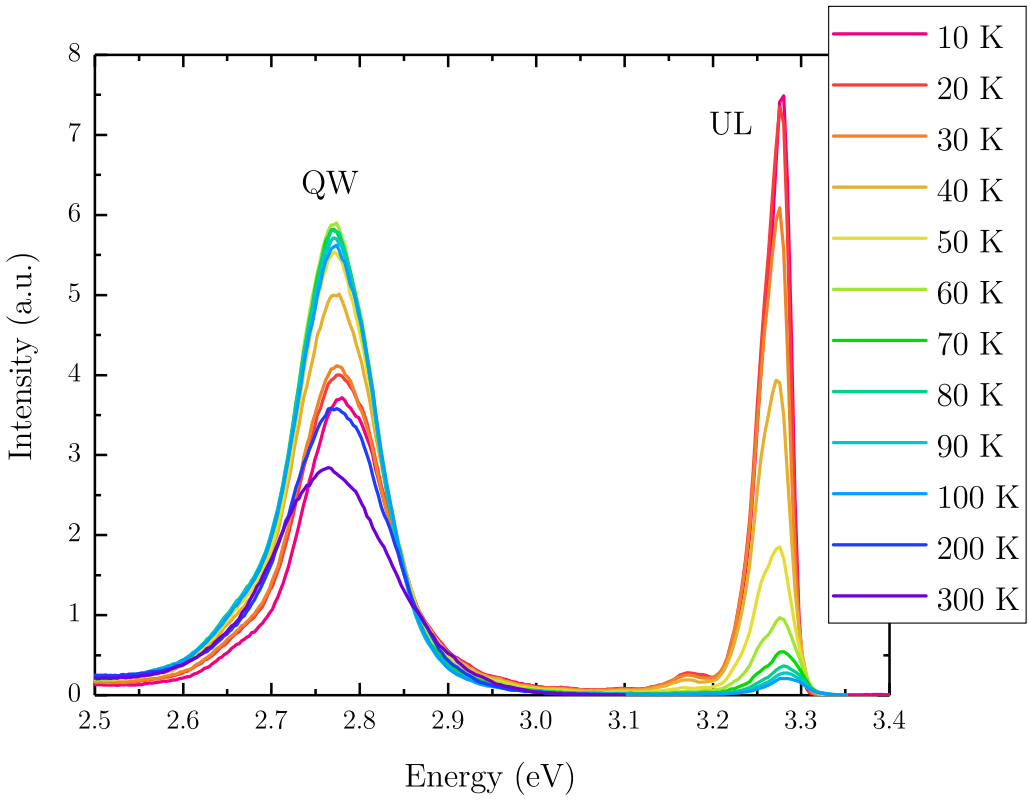

Figure 4.13: Temperature dependent PL spectra for the 1 QW sample containing an UL. The QW and UL emission peaks are as indicated.

The temperature dependences of the QW and UL peak emission energies are shown for the 1 QW sample in Figure 4.14. The QW emission peak clearly exhibits the well-known S-shaped temperature dependence [41–45], and it is possible that similar behaviour occurs for the UL emission peak. However, it was not possible to extract UL peak energies for temperatures above 100 K due to the quenching of the emission. The difference in energy, ΔE, between the minimum in the peak emission energy low temperatures, and the maximum that occurs before the temperature dependence of the bandgap [46] begins to dominate, has been linked to the "depth of localisation" or the energy width of the tail of localised states [41–45]. The QW peak emission energy red shifts by (13 ± 2) meV over the temperature range 10–70 K, before blue shifting by $\Delta E_{\mathrm{QW}} = (4 \pm 2)$ meV over the range 70–180 K. The UL peak red shifts by (6 ± 2) meV as the temperature is raised from 10–40 K and then blue shifts by $\Delta E_{\mathrm{UL}} = (12 \pm 2)$ meV over the range 40–100 K. Similar, or slightly higher, values of

ΔE_{UL} were obtained for the other samples over the temperature range up to 100 K, summarised in Figure 4.15. Large errors are present on the ΔE_{UL} values for the 7, 10 and 15 QW samples due to the very weak UL emission from these samples. The Fabry-Pérot interference fringes prevented the observation of a well-defined S-shape in the temperature dependences of the MQW emission peak energies for the other samples, so no other values of ΔE_{QW} were extracted. Assuming that the UL peak emission energy would eventually reach a maximum before the bandgap shrinkage begins to dominate, the values of ΔE_{UL} are lower limits. Even so, for the 1 QW sample ΔE_{UL} is three times the value of ΔE_{QW} and might indicate that carrier localisation occurs in the highly doped random $In_{0.05}Ga_{0.95}N$ alloy. Further investigations are necessary to determine the nature of carrier recombination in the UL.

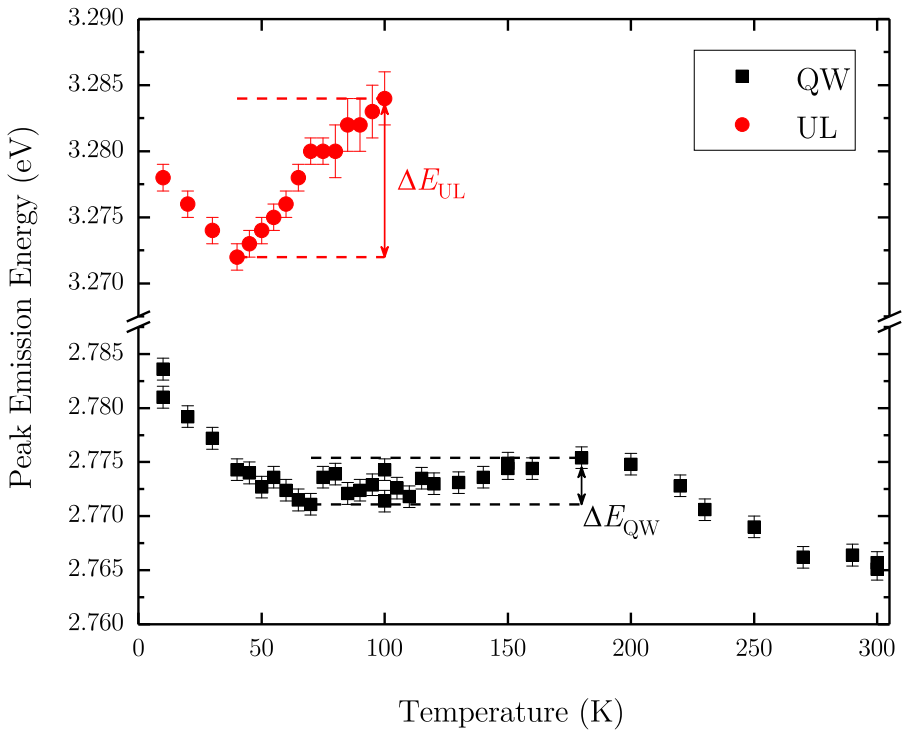

Figure 4.14: Temperature dependences of the QW and UL peak emission energies for the 1 QW sample. The energy spacing between the sets of black and red dashed lines give ΔE_{QW} and ΔE_{UL}, respectively.

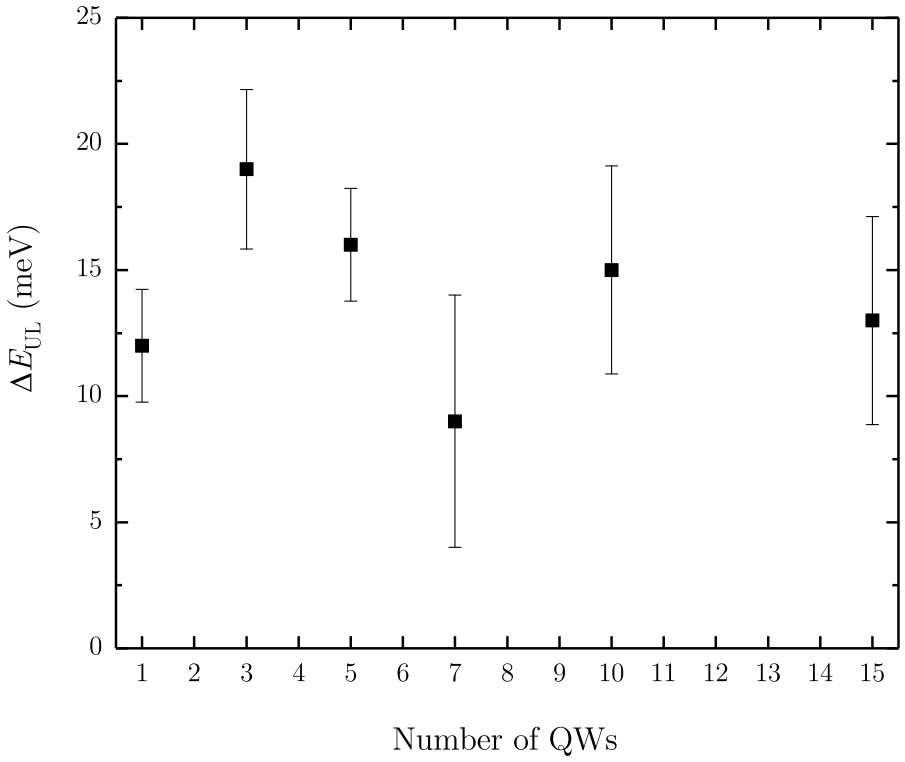

Figure 4.15: ΔE_{UL} values varying with number of QWs.

The temperature dependences of the integrated intensities of the QW and UL emission peaks for the 1 QW sample are shown in Figure 4.16. The integrated intensity values are normalised to that of the QW peak at 10 K. The integrated intensity of the UL emission peak falls rapidly from (0.55 ± 0.05) a.u. to zero as the temperature is increased from 10–100 K. However, the integrated intensity of the QW emission peak increases by (0.45 ± 0.05) a.u. over this temperature range. The integrated intensity of the QW peak reaches a maximum around the temperature where the UL emission is quenched, and then it decreases monotonically up to 300 K to arrive at a value that is 10–20 % less than its value at 10 K. The fact that the intensity increase and decrease for the QW and the UL emission peaks, respectively, are similar over the 10–100 K temperature range may indicate that carriers that are captured or excited in the UL are transferred to the QW.

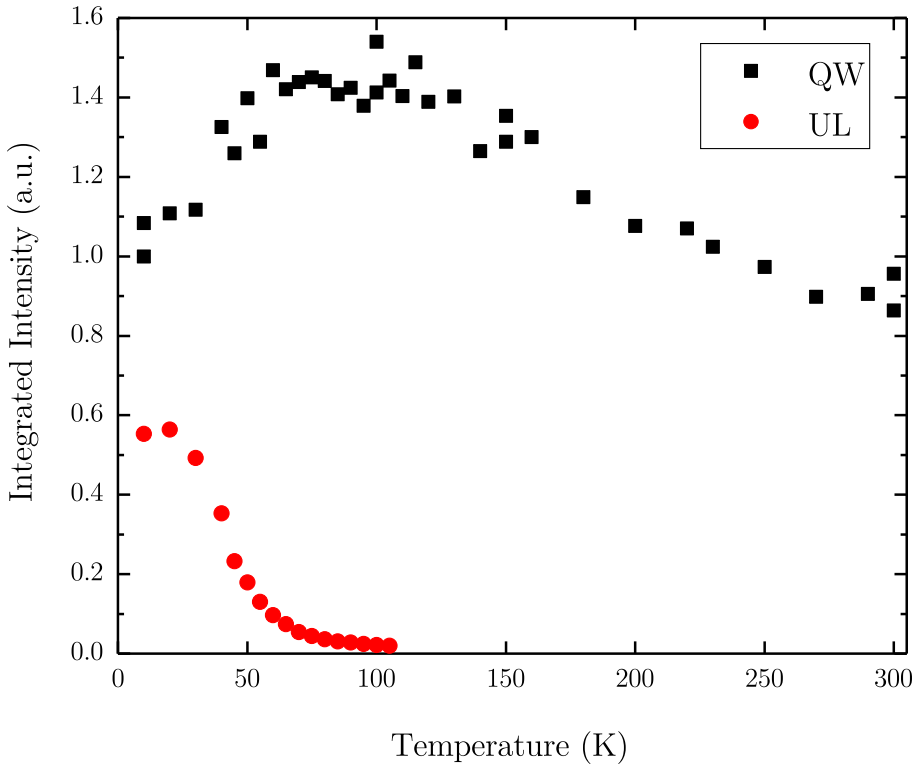

Figure 4.16: Temperature dependences of the integrated intensities of the QW and UL emission peaks for the 1 QW sample.

To investigate whether the inclusion of an UL is responsible for the increase in the QW peak integrated intensity with temperature over the range 10–100 K, temperature dependent PL spectroscopy was performed on the 1 QW sample using a laser diode with an emission energy of 3.061 eV as the excitation source. This energy is below the bandgap of both the GaN QW barriers and the $In_{0.05}Ga_{0.95}N$ UL. Therefore, carriers were only excited in the QW. The integrated intensity of the QW emission peak is shown as a function of temperature in Figure 4.17 for an excitation power density of 30 W cm^{-2}. The integrated intensity decreases monotonically with temperature over the temperature range 10–250 K. This is dramatically different from the behaviour observed in the previous experiment. Since here it is expected that carriers have not been excited in the QW barriers and so could not be captured by the UL, the temperature dependent behaviour of the QW emission intensity when the sample is excited above the GaN band gap must be caused by a process which involves the

presence of carriers in the UL, such as the transfer of carriers from the UL to the QW.

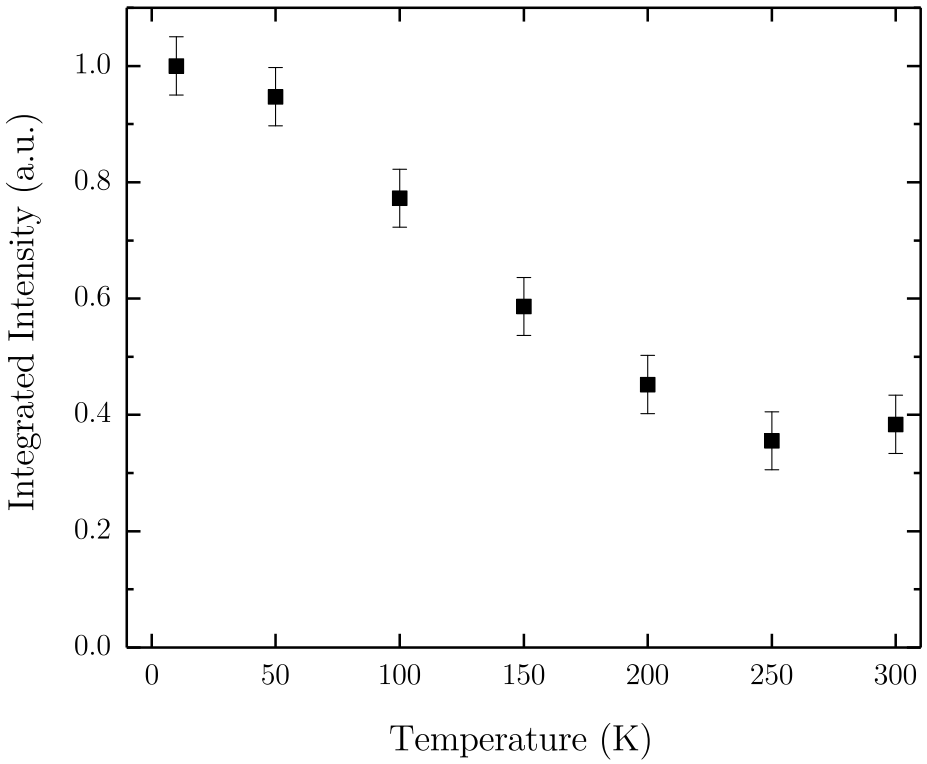

Figure 4.17: Integrated intensity as a function of temperature of the QW emission peak for the 1 QW sample, excited at an energy below the bandgap of the QW barriers and the UL.

The dependence of the integrated intensity, $I(T)$, on the temperature, T, of the UL emission peak was fitted by the Arrhenius equation,

$$I(T) = \frac{I(0)}{1 + Ce^{-\frac{E_A}{k_B T}}}, \tag{4.2}$$

where k_B is the Boltzmann constant, C is a constant and E_A is an activation energy. The fitting is shown in a plot of the integrated intensity varying with $1/T$ in Figure 4.18. A value of (21 ± 1) meV was extracted for E_A. This is close to the barrier height, H, of 23.6 meV for holes to escape from the UL, determined from the calculated VB profiles. This suggests that holes which are excited or captured in the UL are susceptible to thermionic emission, which would leave them free to be captured by the

QW. However, for the electrons in the CB, H is much larger at 142 meV. The rate of thermionic emission of carriers over an energy barrier is proportional to $\left(\frac{1}{m^*}\right)^{\frac{1}{2}} e^{-\frac{H}{k_B T}}$ [47], where m^* is the effective mass of the carrier in question. (For simplicity, any carrier localisation effects that may occur in the UL have been ignored.) This will result in a much lower rate of thermionic emission for electrons than for holes. On the other hand, if holes are transferred to the QW and electrons remain in the UL, the build-up of opposing charges in different regions of the structure would likely lead to band bending which could modify the effective barrier height. Therefore, it is possible that the simultaneous increase and decrease of the QW and UL emission peak integrated intensities, respectively, are due to the transfer of carriers from the UL following thermionic emission. The decreasing integrated intensity of the QW peak with temperature above 100 K can be attributed to the increasing rate of defect-related non-radiative recombination processes, or possibly that of thermionic emission of carriers from the QW.

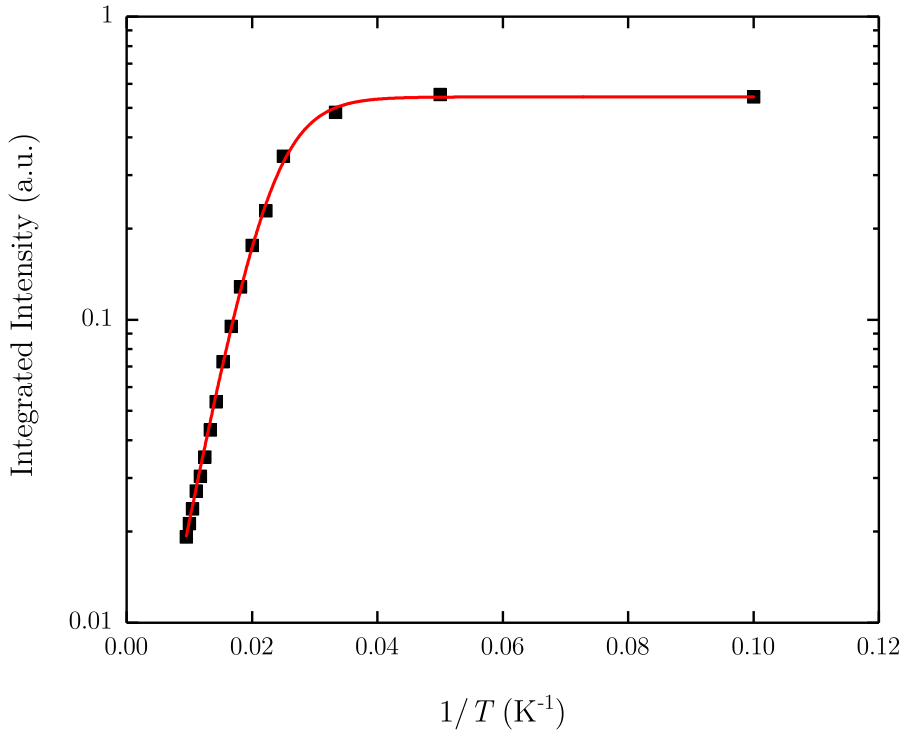

Figure 4.18: Arrhenius plot showing the integrated intensity as a function of $1/T$ for the UL emission peak for the 1 QW sample. The red line shows a fitting of Equation 4.2 from which an activation energy was extracted.

To investigate how the effects of an UL on the radiative recombination rate compete with the effects of additional QWs on IQE, described in Section 4.3, the efficiencies of the MQW samples with ULs were investigated. The temperature dependence of the integrated intensity is shown for the samples with 3–15 QWs in Figure 4.19. For clarity, the scale for the MQW peaks is shown on the left axis, while for the UL peaks it is shown on the right. For each sample, all integrated intensity values were normalised to that of the MQW peak at 10 K. In all cases, the emission from the UL was quenched at temperatures above 100 K. It is common to assume an IQE of 100 % at low temperatures in PL experiments, justified in group III-nitride QW structures by the fact that non-radiative recombination processes are thermally activated [40]. The room temperature IQE would then be calculated as the ratio of the integrated PL intensity at room temperature (300 K) to that at low temperature (10 K). However, the evident effect of the UL on the temperature dependence of the QW emission in-

tensity between 10–100 K means that assumption of a 100 % IQE at 10 K is not valid here. Therefore, the ratio of the (M)QW peak integrated intensity measured at 300 K to that at 100 K, $\eta_{100\,\mathrm{K}}$, was used to compare the efficiencies of the samples as well as the 300 K to 10 K value, $\eta_{10\,\mathrm{K}}$. Both measures of efficiency are shown to decrease monotonically with increasing number of QWs in Figure 4.20.

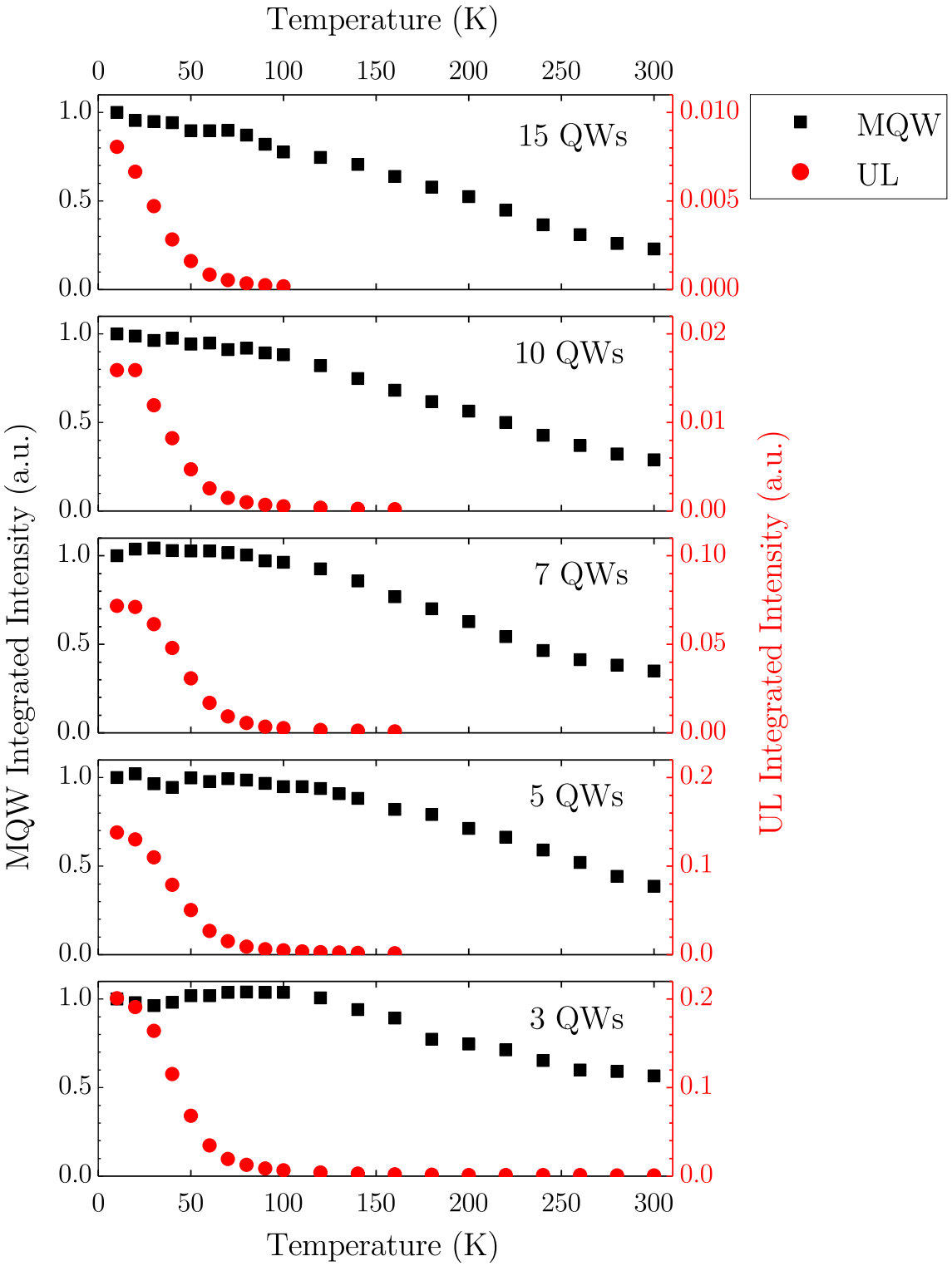

Figure 4.19: Temperature dependences of the integrated intensities of the MQW and UL emission peaks for the 3, 5, 7, 10 and 15 QW samples. The number of QWs is as indicated. All integrated intensities are relative to that for the MQW peak at 10 K. The UL integrated intensities are shown on a magnified scale (right-hand axis) for clarity.

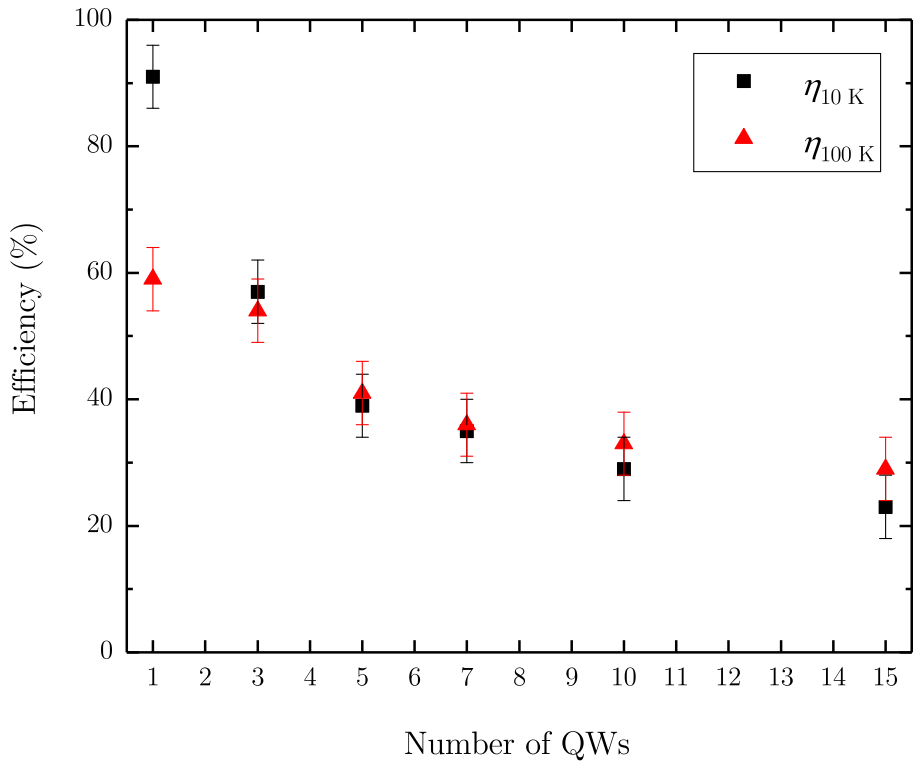

Figure 4.20: $\eta_{10\,\mathrm{K}}$ and $\eta_{100\,\mathrm{K}}$ efficiency values varying with number of QWs.

The room temperature IQE of the 1 QW sample determined from the temperature dependent sub-barrier energy excitation experiment is $(38 \pm 5)\,\%$. The value of $\eta_{100\,\mathrm{K}}$ for the same sample when excited above the GaN bandgap is $(59 \pm 5)\,\%$. Since in the former case carriers were only generated in the InGaN QW, for which the total material thickness is much smaller than that of the GaN in the sample, the expected carrier density in the QW is considerably lower than for excitation above the bandgap of GaN due to the reduced absorption of radiation from the excitation source. For low excited carrier densities, the efficiency of InGaN/GaN QW structures and LEDs has been observed to increase with increasing carrier density [48–52], which has been attributed to the saturation of non-radiative recombination pathways [48]. Therefore, the IQE measured using sub-barrier excitation can be considered to be in reasonable agreement with $\eta_{100\,\mathrm{K}}$ determined using above-barrier excitation. If carrier transfer between the UL and the QW does take place, sub-barrier excitation would indicate that the reduced QCSE due to the surface depletion field is more important than

carrier transfer effects from ULs when determining the mechanism for efficiency improvements in structures such as these. However, a full study of the excitation power dependence of the efficiencies of the full set of MQW samples using excitation radiation energies both above and below the bandgap of the GaN barriers (accounting fully for the different absorption efficiencies) would be necessary to determine conclusively the validity of using the $\eta_{100\,\mathrm{K}}$ efficiency values.

4.6.5 Comparison to MQW Structures Without ULs

Five InGaN/GaN QW samples without ULs were studied for comparison. These were grown using the Q2T growth method. All of the QW widths in all of these samples were measured as $(2.4 \pm 0.1)\,\mathrm{nm}$. The number of QWs was varied between 1 and 10. The QW In fractions and barrier thicknesses for these samples are summarised in Table 4.2.

Table 4.2: Summary of the number of QWs, In composition and barrier thicknesses of each of the samples without ULs.

Sample Number	Number of QWs	QW In Fraction (%)	QW Barrier Thickness (nm)
C4496A	1	20 ± 1	7.4 ± 0.1
C4497A	3	21 ± 1	7.2 ± 0.1
C4494A	5	19 ± 1	7.1 ± 0.1
C4498A	7	20 ± 1	7.1 ± 0.1
C4495A	10	20 ± 1	7.1 ± 0.1

Temperature dependent PL spectroscopy was performed on the series of MQW structures without ULs, described in Section 4.4, at an excitation power density of $15\,\mathrm{W\,cm^{-2}}$. The integrated PL intensity decreased monotonically for all of these structures and so the room temperature IQEs were determined as $\eta_{10\,\mathrm{K}}$. These are shown in Figure 4.21. The room temperature IQE increases with increasing number of QWs. This effect has previously been attributed to the recapture of thermionically emitted carriers by other QWs [19], or to impurity gettering by the increasing number

of interfaces in a structure leading to improved crystal quality [20]. The fact that the efficiency, as determined for the structures containing ULs, displays the opposite behaviour with increasing number of QWs suggests that the increase in the radiative recombination rate due to the reduced QCSE is sufficient to compete with these non-radiative processes. That is, the non-radiative loss of carriers by thermionic emission or recombination at interfaces is more effectively reduced by the increased electron-hole wavefunction overlap in the 1 QW sample than by the carrier recapture or impurity gettering effects in MQWs, respectively. However, it must be noted that the structures containing ULs were grown by the 2T method while those without ULs were grown by the Q2T method (described in Section 2.4 of Chapter 2). QW structures grown by the Q2T method have been shown to have a lower IQE than those grown by the 2T method [32]. This is in agreement with the overall much lower IQEs measured for the structures without ULs compared to those with them. The QW In fractions are also significantly higher in the structures without ULs. The efficiency of InGaN/GaN QW structures has been shown to decrease with increasing QW In fraction [49, 53]. For these reasons, only a qualitative comparison can be made between the dependences on the number of QWs of the IQE for the two sets of structures. To enable a quantitative study of the competition between the efficiency improvements that are due to the inclusion of a UL and those due to increasing the total number of QWs, comparisons to a series of MQW structures which are identical to the series with ULs in growth method and structural parameters but which do not contain ULs would be necessary.

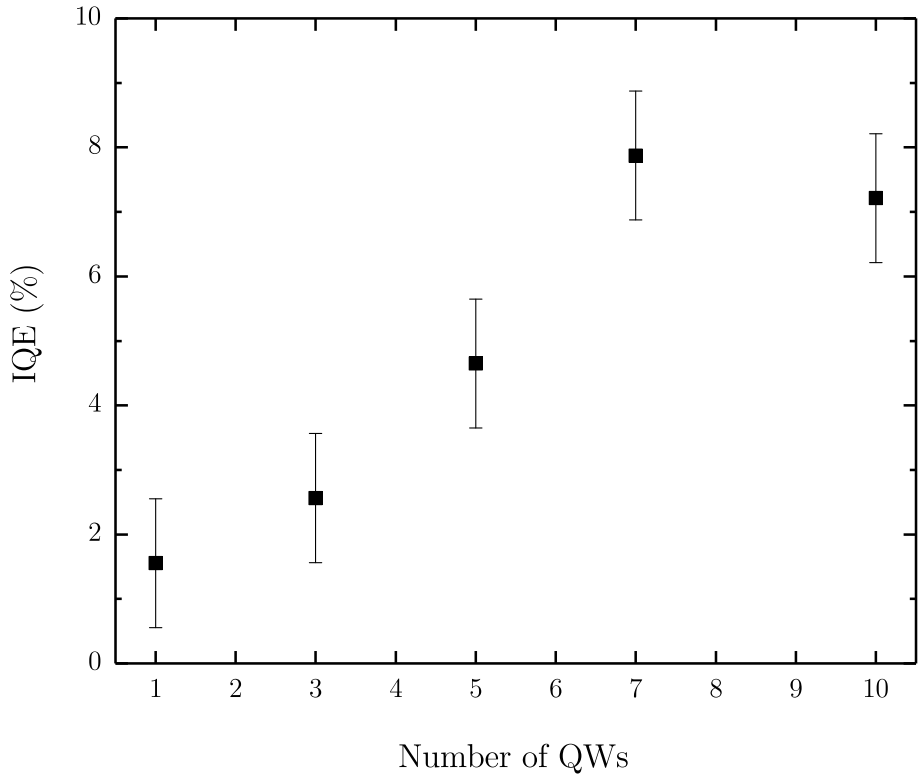

Figure 4.21: Variation of the room temperature IQE with number of QWs for the sample series without ULs.

4.7 Summary and Conclusions

The PL emission properties of InGaN/GaN MQW structures containing Si-doped $In_{0.05}Ga_{0.95}$ ULs, with varying number of QWs, were investigated and compared to simulated CB and VB profiles. From the band profiles, the magnitude of the mean resultant electric field across the QWs was found to increase as the number of QWs increased. This was due to the reduction in the strength of the surface depletion field, which acts in the opposite sense to the strain-induced polarisation fields across the QWs, as the total distance between the n-type layer and the sample surface was increased. At low temperature, the peak PL emission energy of the samples was observed to red shift with increasing number of QWs. Similarly, the peak $\tau_{1/e}$ increased with increasing number of QWs. Both the energy shift and the variation

in $\tau_{1/e}$ were attributed to the increasing magnitude of the QCSE due to the reducing strength of the surface depletion field, leading to a stronger net electric field across the QWs and hence a larger QCSE.

The simulated CB and VB profiles showed a sub-linear increase in the strength of the electric field across the QWs with increasing number of QW periods. This was reflected in the variation of the QW PL peak energy and $\tau_{1/e}$, which decreased and increased sub-linearly with increasing number of QW periods, respectively. For samples with large numbers of QW periods, there was little variation in the mean electric fields across the QWs between samples. This indicates that the magnitude of the surface depletion field becomes negligible compared to the piezoelectric polarisation fields across the QWs when n-type UL is more than 141 nm from the sample surface (this is the nominal depth of the UL in the 15 QW sample).

It was noted that, as the QW In fraction of the 1 QW sample was significantly lower than for the other samples, its blue shifted PL peak energy is partly due to a larger bandgap energy of the QW compared with the other samples as well as the reduced QCSE resulting from the improved lattice matching between the lower In fraction InGaN QW layer and the GaN barrier layer. The latter effect is also expected to be partly responsible for the reduced $\tau_{1/e}$ for this sample relative to the others. However, simulated band profiles for a hypothetical sample with the same parameters as the real 1 QW sample, but with the QW In fraction matched to that of the 3 QW sample, showed that a significant change in electric field strength across the QWs still occurred between that sample and the 3 QW sample. Therefore, the shift in PL peak emission energy and change in $\tau_{1/e}$ would still be expected if the QW In fractions were the same across all of the samples.

The integrated intensity of the QW PL emission peak for the 1 QW sample increased as the temperature was increased from 10–100 K. The gain in absolute intensity was similar to the intensity of the UL emission peak at 10 K, which was itself quenched at 100 K. In temperature dependent PL spectra of the 1 QW sample excited

below the bandgap energy of the barriers and the UL, no initial increase in integrated intensity was observed. Instead, the integrated intensity decreased monotonically. This is evidence that the temperature dependent observations at higher excitation energy are a result of a process involving carriers captured in the UL. Thermionic emission of carriers captured in the UL, leading to their being recaptured by the QW, was suggested as a possible mechanism for carrier transfer between the UL and the QW which could bring about the initial increase in the integrated intensity of the QW emission.

The efficiencies of the samples were compared by calculating $\eta_{10\,\mathrm{K}}$ and $\eta_{100\,\mathrm{K}}$, defined as the ratios of the QW emission integrated intensity at 300 K to those at 10 K and 100 K, respectively. The fact that the UL causes an increase in the integrated intensity of the QW emission prevented the extraction of an IQE value. $\eta_{100\,\mathrm{K}}$ was used to compare the efficiencies of the (M)QWs at temperatures above which the QW integrated intensity decreased monotonically. Both $\eta_{10\,\mathrm{K}}$ and $\eta_{100\,\mathrm{K}}$ were observed to decrease monotonically with increasing number of QWs. Since the mean net electric field across the QWs increases with increasing number of QWs, this suggests that the increased radiative recombination rate due to the reduced QCSE is sufficient to overcome non-radiative carrier losses due to thermionic emission and/or non-radiative recombination at surface states that would otherwise be compensated by the addition of QWs to a structure. Evidence for the latter point was provided in the increasing room temperature IQE with increasing number of QWs for a series of MQW structures without ULs. However, these structures were grown under very different conditions and so only limited comparisons can be made to the structures containing ULs. The IQE determined for the 1 QW UL sample from the temperature dependent PL spectroscopy performed using sub-barrier excitation was similar to the value of $\eta_{100\,\mathrm{K}}$ for that sample, accounting for the lower excited carrier density in the QW due to the reduced absorption of the excitation light. This suggests that $\eta_{100\,\mathrm{K}}$ is a valid measure of efficiency for comparing the samples. Further study which includes an identical se-

ries of samples without ULs is necessary to investigate fully the competition between the effects of the UL and the number of QWs.

4.8 References

[1] T. Akasaka *et al.* "High luminescent efficiency of InGaN multiple quantum wells grown on InGaN underlying layers". *Applied Physics Letters* **85**, 15 (2004), 3089. DOI: 10.1063/1.1804607 (Cited on pages 70, 71, 72).

[2] T. Akasaka *et al.* "Blue-purplish InGaN quantum wells with shallow depth of exciton localization". *Applied Physics Letters* **86**, 19 (2005), 191902. DOI: 10.1063/1.1925314 (Cited on pages 70, 71, 73).

[3] Y. Takahashi *et al.* "Enhanced radiative efficiency in blue (In,Ga)N multiple-quantum-well light-emitting diodes with an electron reservoir layer". *Physica E: Low-dimensional Systems and Nanostructures* **21**, 2-4 (2004), 876. DOI: 10.1016/j.physe.2003.11.142 (Cited on pages 70, 72, 77).

[4] N. Otsuji *et al.* "Electroluminescence efficiency of blue InGaN/GaN quantum-well diodes with and without an n-InGaN electron reservoir layer". *Journal of Applied Physics* **100**, 11 (2006), 113105. DOI: 10.1063/1.2398690 (Cited on pages 70, 72, 77).

[5] N. Nanhui *et al.* "Enhanced luminescence of InGaN/GaN multiple quantum wells by strain reduction". *Solid-State Electronics* **51**, 6 (2007), 860. DOI: 10.1016/j.sse.2007.04.007 (Cited on pages 70, 71, 74, 75).

[6] P. T. Törmä *et al.* "Effect of InGaN underneath layer on MOVPE-grown InGaN/GaN blue LEDs". *Journal of Crystal Growth* **310**, 23 (2008), 5162. DOI: 10.1016/j.jcrysgro.2008.07.031 (Cited on pages 70, 71, 74, 75).

[7] H. Takahashi *et al.* "Effect of Intentionally Formed 'V-Defects' on the Emission Efficiency of GaInN Single Quantum Well". *Japanese Journal of Applied Physics* **39**, Part 2, No. 6B (2000), L569. DOI: 10.1143/JJAP.39.L569 (Cited on pages 70, 72, 76).

[8] J. K. Son *et al.* "Enhanced optical properties of InGaN MQWs with InGaN underlying layers". *Journal of Crystal Growth* **287** (2006), 558. DOI: 10.1016/j.jcrysgro.2005.10.071 (Cited on pages 70, 71, 73).

[9] A. M. Armstrong *et al.* "Defect-reduction mechanism for improving radiative efficiency in InGaN/GaN light-emitting diodes using InGaN underlayers". *Journal of Applied Physics* **117**, 13 (2015), 134501. DOI: 10.1063/1.4916727 (Cited on pages 70, 71, 73).

[10] H. Shan *et al.* "The performance enhancement of an InGaN/GaN multiple-quantum-well solar cell by superlattice structure". *Japanese Journal of Applied Physics* **56**, 11 (2017), 110305. DOI: 10.7567/JJAP.56.110305 (Cited on pages 70, 71, 74, 75).

[11] M. J. Davies *et al.* "Effects of an InGaN prelayer on the properties of InGaN/GaN quantum well structures". *physica status solidi (c)* **11**, 3-4 (2014), 710. DOI: 10.1002/pssc.201300451 (Cited on page 70).

[12] M. J. Davies *et al.* "The effects of Si-doped prelayers on the optical properties of InGaN/GaN single quantum well structures". *Applied Physics Letters* **105**, 9 (2014), 092106. DOI: 10.1063/1.4894834 (Cited on pages 70, 71, 72, 80, 87, 88).

[13] M. J. Davies *et al.* "A study of the inclusion of prelayers in InGaN/GaN single- and multiple-quantum-well structures". *physica status solidi (b)* **252**, 5 (2015), 866. DOI: 10.1002/pssb.201451535 (Cited on pages 70, 71, 72, 81, 87, 88).

[14] M. J. Davies *et al.* "A comparison of the optical properties of InGaN/GaN multiple quantum well structures grown with and without Si-doped InGaN prelayers". *Journal of Applied Physics* **119**, 5 (2016), 055708. DOI: 10.1063/1.4941321 (Cited on pages 70, 71, 72, 81, 87, 88).

[15] C. Netzel *et al.* "Experimental method for scanning the surface depletion region in nitride based heterostructures". *physica status solidi (c)* **6**, S2 (2009), S691. DOI: 10.1002/pssc.200880793 (Cited on pages 70, 71, 79, 80).

[16] V. Fiorentini *et al.* "Effects of macroscopic polarization in III-V nitride multiple quantum wells". *Physical Review B* **60**, 12 (1999), 8849. DOI: 10.1103/PhysRevB.60.8849 (Cited on pages 70, 77, 78).

[17] O. Mayrock *et al.* "Polarization charge screening and indium surface segregation in (In,Ga)N/GaN single and multiple quantum wells". *Physical Review B* **62**, 24 (2000), 16870. DOI: 10.1103/PhysRevB.62.16870 (Cited on pages 70, 71, 78, 79).

[18] B. Monemar *et al.* "Influence of polarization fields and depletion fields on photoluminescence of AlGaN/GaN multiple quantum well structures". *physica status solidi (b)* **237**, 1 (2003), 353. DOI: 10.1002/pssb.200301782 (Cited on pages 70, 71, 79, 82).

[19] P. Hurst *et al.* "Temperature Dependent Optical Properties of InGaN/GaN Quantum Well Structures". *physica status solidi (b)* **228**, 1 (2001), 137. DOI: 10.1002/1521-3951(200111)228:1<137::AID-PSSB137>3.0.CO;2-R (Cited on pages 71, 82, 108).

[20] M. S. Minsky *et al.* "Characterization of high-quality InGaN/GaN multiquantum wells with time-resolved photoluminescence". *Applied Physics Letters* **72**, 9 (1998), 1066. DOI: 10.1063/1.120966 (Cited on pages 71, 82, 109).

[21] G. Thucydides *et al.* "Picosecond photoluminescence studies of carrier escape processes in a single quantum well". *Semiconductor Science and Technology* **11**, 3 (1996), 331. DOI: 10.1088/0268-1242/11/3/010 (Cited on pages 71, 82).

[22] P. Dawson and K. Woodridge. "Effects of prelayers on minority-carrier lifetime in GaAs/AlGaAs double heterostructures grown by molecular beam epitaxy". *Applied Physics Letters* **45**, 1984 (1984), 1227. DOI: 10.1063/1.95107 (Cited on pages 71, 72, 83).

[23] J. S. Rimmer *et al.* "Correlation between optical spectroscopy and capacitance-voltage profile simulation applied to interface states in multilayer GaAs/AlGaAs heterostructures". *Journal of Applied Physics* **73**, 10 (1993), 5032. DOI: 10.1063/1.353773 (Cited on pages 72, 83).

[24] H. Kumano *et al.* "Effect of indium doping on the transient optical properties of GaN films". *Applied Physics Letters* **75**, 19 (1999), 2879. DOI: 10.1063/1.125178 (Cited on page 73).

[25] M. Copel *et al.* "Surfactants in epitaxial growth". *Physical Review Letters* **63**, 6 (1989), 632. DOI: 10.1103/PhysRevLett.63.632 (Cited on page 73).

[26] Y. Chen *et al.* "Pit formation in GaInN quantum wells". *Applied Physics Letters* **72**, 6 (1998), 710. DOI: 10.1063/1.120853 (Cited on pages 75, 76).

[27] I. H. Kim *et al.* "Formation of V-shaped pits in InGaN/GaN multiquantum wells and bulk InGaN films". *Applied Physics Letters* **73**, 12 (1998), 1634. DOI: 10.1063/1.122229 (Cited on page 75).

[28] A. Hangleiter *et al.* "Suppression of nonradiative recombination by V-shaped pits in GaInN/GaN quantum wells produces a large increase in the light emission efficiency". *Physical Review Letters* **95**, 12 (2005), 127402. DOI: 10.1103/PhysRevLett.95.127402 (Cited on page 77).

[29] O. Mayrock *et al.* "Influence of Internal Polarization Fields on the Disorder Broadening of Excitons in (In,Ga)N/GaN Quantum Wells". *physica status solidi (b)* **216**, 1 (1999), 419. DOI: 10.1002/(SICI)1521-3951(199911)216:1<419::AID-PSSB419>3.0.CO;2-G (Cited on page 80).

[30] A. Hangleiter *et al.* "Optical Properties of Nitride Quantum Wells: How to Separate Fluctuations and Polarization Field Effects". *physica status solidi (b)* **216**, 1 (1999), 427. DOI: 10.1002/(SICI)1521-3951(199911)216:1<427::AID-PSSB427>3.0.CO;2-K (Cited on page 80).

[31] S. Hammersley *et al.* "Effect of electron blocking layers on the conduction and valence band profiles of InGaN/GaN LEDs". *physica status solidi (c)* **13**, 5-6 (2016), 262. DOI: 10.1002/pssc.201510188 (Cited on page 82).

[32] R. A. Oliver *et al.* "The impact of gross well width fluctuations on the efficiency of GaN-based light emitting diodes". *Applied Physics Letters* **103**, 14 (2013), 141114. DOI: 10.1063/1.4824193 (Cited on pages 83, 109).

[33] S. Birner *et al.* "nextnano: General Purpose 3-D Simulations". *IEEE Transactions on Electron Devices* **54**, 9 (2007), 2137. DOI: 10.1109/TED.2007.902871 (Cited on page 84).

[34] W. J. Moore *et al.* "Magneto-optical studies of free-standing hydride-vapor-phase epitaxial GaN". *Physical Review B* **65**, 8 (2002), 081201. DOI: 10.1103/PhysRevB.65.081201 (Cited on page 85).

[35] D. M. Graham *et al.* "Optical and microstructural studies of InGaN/GaN single-quantum-well structures". *Journal of Applied Physics* **97**, 10 (2005), 103508. DOI: 10.1063/1.1897070 (Cited on page 91).

[36] R. Pecharromán-Gallego *et al.* "Investigations of phonon sidebands in InGaN/GaN multi-quantum well luminescence". *Materials Science and Engineering: B* **93**, 1-3 (2002), 94. DOI: 10.1016/S0921-5107(02)00024-7 (Cited on page 91).

[37] W. Liu *et al.* "Phonon-assisted photoluminescence in wurtzite GaN epilayer". *Semiconductor Science and Technology* **13**, 7 (1998), 769. DOI: 10.1088/0268-1242/13/7/018 (Cited on page 91).

[38] T. Wang *et al.* "Photoluminescence investigation of InGaN/GaN single quantum well and multiple quantum wells". *Applied Physics Letters* **73**, 24 (1998), 3571. DOI: 10.1063/1.122810 (Cited on page 95).

[39] H. K. Cho *et al.* "Influence of strain relaxation on structural and optical characteristics of InGaN/GaN multiple quantum wells with high indium composition". *Journal of Applied Physics* **91**, 3 (2002), 1166. DOI: 10.1063/1.1429765 (Cited on page 95).

[40] A. Hangleiter *et al.* "Towards understanding the emission efficiency of nitride quantum wells". *physica status solidi (a)* **201**, 12 (2004), 2808. DOI: 10.1002/pssa.200405051 (Cited on pages 95, 104).

[41] P. G. Eliseev *et al.* "Blue temperature-induced shift and band-tail emission in InGaN-based light sources". *Applied Physics Letters* **71**, 5 (1997), 569. DOI: 10.1063/1.119797 (Cited on page 98).

[42] Y.-H. Cho *et al.* "S-shaped temperature-dependent emission shift and carrier dynamics in InGaN/GaN multiple quantum wells". *Applied Physics Letters* **73**, 10 (1998), 1370. DOI: 10.1063/1.122164 (Cited on page 98).

[43] Q. Li *et al.* "Thermal redistribution of localized excitons and its effect on the luminescence band in InGaN ternary alloys". *Applied Physics Letters* **79**, 12 (2001), 1810. DOI: 10.1063/1.1403655 (Cited on page 98).

[44] P. G. Eliseev. "The red $\sigma 2$/kT spectral shift in partially disordered semiconductors". *Journal of Applied Physics* **93**, 9 (2003), 5404. DOI: 10.1063/1.1567055 (Cited on page 98).

[45] R. Pecharromán-Gallego *et al.* "Investigation of the unusual temperature dependence of InGaN/GaN quantum well photoluminescence over a range of emission energies". *Journal of Physics D: Applied Physics* **37**, 21 (2004), 2954. DOI: 10.1088/0022-3727/37/21/003 (Cited on page 98).

[46] Y. Varshni. "Temperature dependence of the energy gap in semiconductors". *Physica* **34**, 1 (1967), 149. DOI: 10.1016/0031-8914(67)90062-6 (Cited on page 98).

[47] H. Schneider and K. von Klitzing. "Thermionic emission and Gaussian transport of holes in a GaAs/AlGaAs multuple-quantum-well structure". *Physical Review B* **38**, 9 (1988), 6160. DOI: 10.1103/PhysRevB.38.6160 (Cited on page 103).

[48] H. Murotani *et al.* "Excitation density dependence of radiative and nonradiative recombination lifetimes in InGaN/GaN multiple quantum wells". *physica status solidi (b)* **252**, 5 (2015), 940. DOI: 10.1002/pssb.201451491 (Cited on page 107).

[49] S. Hammersley *et al.* "Effects of quantum well growth temperature on the recombination efficiency of InGaN/GaN multiple quantum wells that emit in the green and blue spectral regions". *Applied Physics Letters* **107**, 13 (2015), 132106. DOI: 10.1063/1.4932200 (Cited on pages 107, 109).

[50] M.-H. Kim *et al.* "Origin of efficiency droop in GaN-based light-emitting diodes". *Applied Physics Letters* **91**, 18 (2007), 183507. DOI: 10.1063/1.2800290 (Cited on page 107).

[51] D.-P. Han *et al.* "Nonradiative recombination mechanisms in InGaN/GaN-based light-emitting diodes investigated by temperature-dependent measurements". *Applied Physics Letters* **104**, 15 (2014), 151108. DOI: 10.1063/1.4871870 (Cited on page 107).

[52] T. Mukai *et al.* "Characteristics of InGaN-Based UV/Blue/Green/Amber/Red Light-Emitting Diodes". *Japanese Journal of Applied Physics* **38**, Part 1, No. 7A (1999), 3976. DOI: 10.1143/JJAP.38.3976 (Cited on page 107).

[53] M. Auf der Maur *et al.* "Efficiency Drop in Green InGaN/GaN Light Emitting Diodes: The Role of Random Alloy Fluctuations". *Physical Review Letters* **116**, 2 (2016), 027401. DOI: 10.1103/PhysRevLett.116.027401 (Cited on page 109).

Chapter 5

Optical Properties of *c*-Plane Single Quantum Wells as a Function of Net Electric Field Strength

5.1 Introduction

The net electric fields, resulting from contributions from the spontaneous and piezoelectric polarisations of InGaN and GaN, across *c*-plane InGaN/GaN QWs grown on sapphire are typically reported to be of the order $\sim$1 MV cm^{-1} [1–5]. Calculations [6–8] have demonstrated that these fields, in combination with QWWFs as small as one monolayer at the upper interface of the QW [9], lead to minima in the potential landscape in the plane of the QW that are sufficient to localise electrons at low temperatures.

On the other hand, such large electric fields perpendicular to the plane of the QWs lead to dramatic separations of the electron and hole wavefunctions along the growth axis, as well as lower recombination energies (the QCSE, described in Chapter

2). This reduced electron-hole wavefunction overlap results in a lowered radiative recombination rate which means that non-radiative recombination processes become more competitive. At the high QW In fractions required to produce structures which emit light in the green and longer wavelength regions of the visible spectrum, this effect is particularly prominent and is one of the main reasons that LEDs based on InGaN/GaN QW structures emitting in this spectral region are currently much less efficient than those that emit blue light (the so-called green gap) [5, 10–12].

It has also been claimed [13, 14] that these electric fields lead to reduced quantum confinement of carriers by the QWs, and that this causes a reduction in the carrier capture efficiency by the active region of LEDs. The loss of carriers through such leakage processes is one proposed mechanism for the efficiency droop in EL measurements [13–18].

Another proposed detrimental effect of the electric fields on device performance is the inhomogeneous distribution of carriers within QWs, which some groups have suggested leads to an increased rate of non-radiative carrier loss via Auger recombination due to the high local carrier densities [10, 14, 19, 20].

Reducing or eliminating the net electric fields across InGaN/GaN QWs may prove to be a necessary step towards producing efficient high brightness LEDs as well as phosphor-free white and wavelength-tunable light sources based on RGB LED designs which are currently hampered by the green gap problem. A reduced radiative lifetime resulting from the increased electron-hole wavefunction overlap would also be desirable in VLC applications where a fast switching rate is required to enable high bit rate data transfer [21]. In pursuing this, however, it is important to consider the impact that this may have on the carrier localisation effects that are known to be responsible for the high IQEs that have already been achieved in these structures. In Chapter 4 it was demonstrated that the strength of the surface depletion field, known to be present near the surface of Ga-terminated GaN [1, 2], can be manipulated by varying the distance between an n-type UL and the sample surface. The surface depletion

field, which occurs as a result of the spontaneous polarisation of the lattice, is of opposite sense to the strain-induced piezoelectric polarisation field and so QWs which are positioned in this region have reduced net electric fields. Building on that work, the samples studied in this chapter were grown with ULs positioned deliberately such that the net QW electric fields were reduced by one or two orders of magnitude below the values usually reported in the literature for standard c-plane QW structures. Their optical properties were investigated to determine the effects of having near-zero electric fields across the QWs on the carrier dynamics and PL emission properties.

5.2 Methods to Reduce or Remove Electric Fields

Because of the detrimental effects of the electric fields on QW efficiency, various methods for mitigating their impact have been proposed.

Since the electric fields occur due to the polar nature of the $[0\,0\,0\,1]$ (c), growth direction, one way to remove them is to grow QWs in a direction perpendicular to this — the $[1\,\bar{1}\,0\,0]$ (m) or $[1\,1\,\bar{2}\,2]$ (a) growth directions — where the polarisation is instead in the plane of the QW and so theoretically the QCSE should be eliminated [8, 22–24]. APT measurements have shown that the m-plane InGaN/GaN QWs can be considered to be a random alloy, or possibly to exhibit a small amount of In clustering [22], with monolayer QWWFs occurring more prominently on the upper QW interface than the lower one for structures grown by MOVPE. The latter result is similar to that reported for c-plane QWs [9]. Calculations demonstrated [8, 22] that the In composition fluctuations are sufficient to cause hole localisation, as in c-plane QWs, but that the absence of the electric field perpendicular to the plane of the QW means that carriers are much less sensitive to the localising effects of the QWWFs. Since QWWFs have been shown to be the main source of electron localisation in c-plane InGaN/GaN QWs [6–8], it was found that the lack of separate electron localisation in m-plane QWs means that the electron-hole Coulomb interaction is sufficient

that localised excitons form at In composition fluctuations [8, 22]. Evidence for this has been observed experimentally where exponential PL decays have been reported across the PL peak from non-polar *m*-plane QWs on much faster time scales than the non-exponential decays from their polar *c*-plane counterparts [8, 22, 23]. InGaN/GaN QWs grown in the zincblende crystal phase have also been suggested as promising candidates for longer wavelength LEDs because of the expected absence of spontaneous and piezoelectric polarisation resulting from the centrosymmetric unit cell of zincblende group III-nitrides [25–27].

Some groups have aimed to achieve reduced, or near-zero, net electric fields across QWs based on *c*-plane wurtzite material using specially designed doping and/or alloy profiles [10, 13, 14, 19, 20, 28].

Kim *et al.* [13] showed that perfectly square QW band profiles can theoretically be achieved by using AlGaInN barriers between InGaN QWs in an LED, where the barrier alloy composition is chosen such that the polarisation charges formed in the QW layers are matched exactly. The remaining polarisation charges formed at the bottom and top of the QW stack are compensated with *n* and *p*-type doping, respectively. Current density dependent EL measurements showed that this type of LED displayed a much less dramatic efficiency droop at high injected current densities than a reference LED for which this polarisation matching technique had not been employed. The authors claimed that this was due to improved quantum confinement by the rectangular QWs, leading to better carrier capture and so smaller current losses.

Young *et al.* [28] performed PL spectroscopy measurements on two different single InGaN/GaN QW LEDs under a range of applied biases. One of the LEDs was grown with *n* and *p*-type doping below and above the QW, respectively, such that the fixed polarisation charges formed at the QW interfaces would be fully compensated. The PL peak energy of this LED remained constant over the full range of applied biases, while the emission from the other LED blue shifted with increasing bias. The blue shift was attributed to the screening of the field across the QW by the accumulation

of electrons and holes at opposite interfaces of the QW with increasing injected carrier density, while the lack of any shift in the emission from the doped LED was said to be because the electric field was already screened by the doped layers.

Several groups have also claimed that the electron-hole wavefunction overlap can be improved by making the discontinuity between the barrier and QW material less abrupt, either through a step [10, 19, 29] or gradient [14, 20] alloy composition profile in the QWs or the barriers.

In Chapter 4 it was shown that the piezoelectric polarisation field can be compensated by varying the total distance between an n-type UL and the sample surface, meaning that the range (and therefore the strength) of the surface depletion field can be manipulated. For the single QW samples studied in this chapter, this distance was controlled by varying the thickness of the final GaN cap layer that was grown on four otherwise nominally identical structures. While not relevant to LEDs under bias, this method of varying the net electric field across c-plane QWs allows for detailed the study of the physical processes that lead to carrier localisation in these systems through PL spectroscopic measurements by varying only one parameter (cap layer thickness), and so is ideal for this purpose.

5.3 Sample Details

Four single QW samples were grown using the 1T growth method by colleagues at the Department of Materials Science and Metallurgy, University of Cambridge. This growth method prevents the loss of In atoms from the QW that otherwise occurs when the growth temperature is that which is optimal for the barrier material, while also allowing more precise control over the barrier thickness than the Q2T method in which a thin GaN layer is grown immediately after the InGaN QW but before the GaN barrier [30]. The different growth methods are described in more detail in Chapter 2. While QWs grown by the 1T method have been shown to exhibit

lower IQEs than those grown by the 2T method [30], the thicknesses of the epitaxial layers is a much more important parameter than the IQE for the purposes of this study. The samples were grown on top of 5 µm GaN pseudo-substrates on sapphire. For all of the samples, a 2 µm GaN:Si template with Si doping density $5 \times 10^{18}\,\mathrm{cm}^{-3}$ was grown followed by a $(24.1 \pm 0.3)\,\mathrm{nm}$ thick $\mathrm{In}_y\mathrm{Ga}_{1-y}\mathrm{N}$:Si ($y = 0.059 \pm 0.002$) UL with nominal Si doping density $2 \times 10^{19}\,\mathrm{cm}^{-3}$. On top of the UL a 3.5 nm thick GaN spacer layer was grown followed by a $(2.7 \pm 0.1)\,\mathrm{nm}$ thick $\mathrm{In}_x\mathrm{Ga}_{1-x}\mathrm{N}$ ($x = 0.180 \pm 0.005$) QW. Finally, a GaN cap layer was grown. The thickness of the cap layer was varied between the samples. The spacer layer, QW and cap layer were grown with no intentional doping. Determining the alloy composition of single layers by XRD is made difficult by the peak broadening caused by the thin layer [31]. For this reason, 2 structures each containing 5 QWs with nominally the same alloy composition as the single QWs were grown, with different barrier growth times. The average QW In fractions were determined by XRD for each of these structures as 0.178 ± 0.005 and 0.182 ± 0.005, respectively, and the value of x given for the single QWs was taken as the mean of these values. The measured In fractions are consistent within the experimental error, so it is assumed that sufficient control was achieved to produce single QW structures with the same alloy composition. The barrier layer thicknesses were determined by XRD for the two 5 QW structures and, with the barrier growth times known, a growth rate was calculated from which the single QW cap layer thicknesses were determined. All structural characterisation was performed by colleagues at the University of Cambridge. The different cap layer thicknesses are shown with the corresponding sample reference numbers in Table 5.1.

Table 5.1: Summary of the single QW samples grown with different GaN cap layer thicknesses.

Sample Number	Cap Thickness (nm)
C6897A	2.0
C6985A	3.0
C6898A	4.0
C6896A	5.0

5.4 Results and Discussion

5.4.1 Simulation Results

The 1-dimensional CB and VB profiles were simulated for each sample using nextnano^3 [32], as described in Section 4.5 of Chapter 4, using the experimentally determined layer thicknesses and alloy compositions and the nominal doping densities as input parameters. These are shown in Figure 5.1, where the energy scale is defined with the Fermi level at zero. Positions are defined relative to the interface between the UL and the GaN spacer layer (the layer beneath the QW).

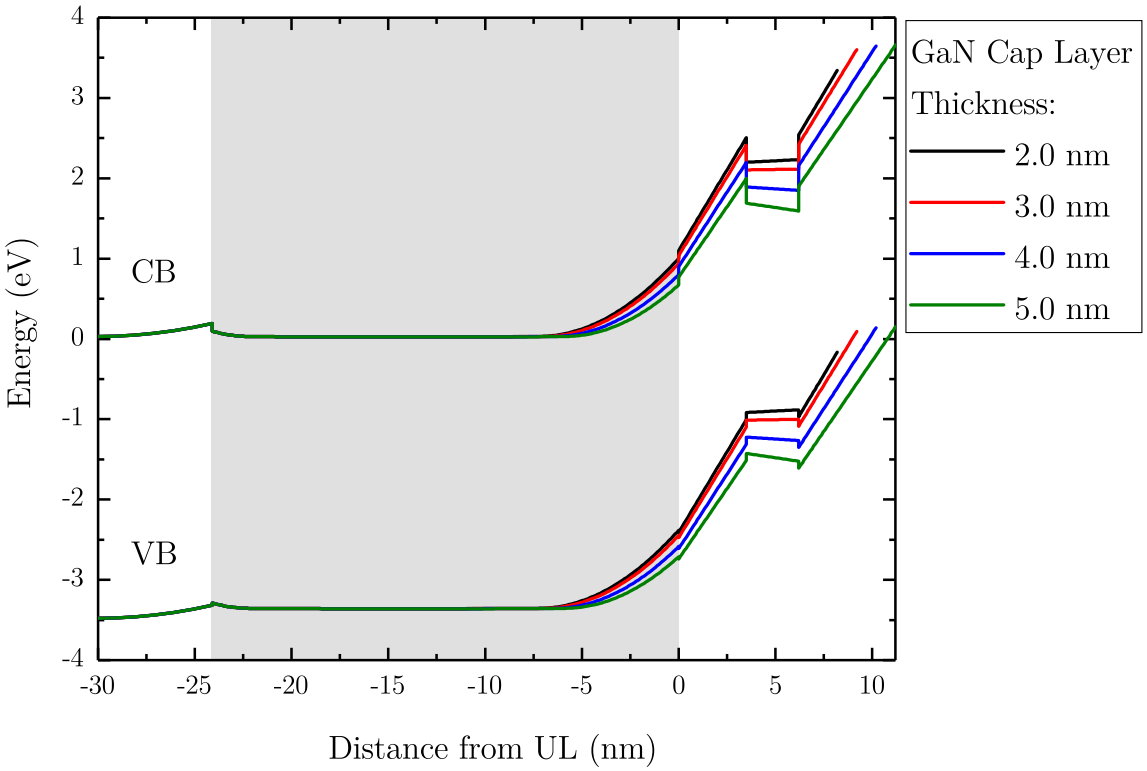

Figure 5.1: CB and VB profiles for the samples with varying GaN cap layer thicknesses. Distances are defined relative to the interface between the GaN spacer layer and energies are defined relative to the Fermi level. The UL is marked by the shaded area.

According to the simulated band profiles, the net electric field across the QWs for the samples with 4.0 and 5.0 nm thick cap layers is in the direction of the field due to the strain-induced piezoelectric polarisation. That is, the direction commonly observed for InGaN/GaN QWs without ULs [13, 28, 33]. However, the net electric field across the QWs for the samples with 2.0 and 3.0 nm thick cap layers is in the same direction as the surface depletion field. Moreover, for the sample with the 3.0 nm thick cap layer, the calculated electric field across the QW is $-0.0374\,\mathrm{MV\,cm^{-1}}$ (the sign is negative to indicate that it is in the opposite direction to fields usually calculated or measured for InGaN/GaN QWs). While all of the calculated electric fields across the samples studied in this chapter are smaller than any of those for the samples with ULs studied in Chapter 4, the magnitude of the electric field across the QW with the 3.0 nm thick cap layer is reduced by almost 100 times relative to the values usually

quoted for InGaN/GaN QWs ($\sim$1 MV cm^{-1}) [1–5]. Since the main cause of electron localisation in these structures is the combined effects of the QWWFs and the built-in electric fields [6–8, 34], it is interesting to investigate the effects of a sample that may possibly be considered to have "zero" net electric field across the QW, as well as one where the field is reversed.

The electric fields extracted from the simulated band profiles are shown varying with cap layer thickness in Figure 5.2. Since the size of the surface depletion field region (and correspondingly the surface depletion field strength) decreases with increasing cap layer thickness, the net electric field across the QW decreases and eventually changes sign as the cap layer thickness is reduced.

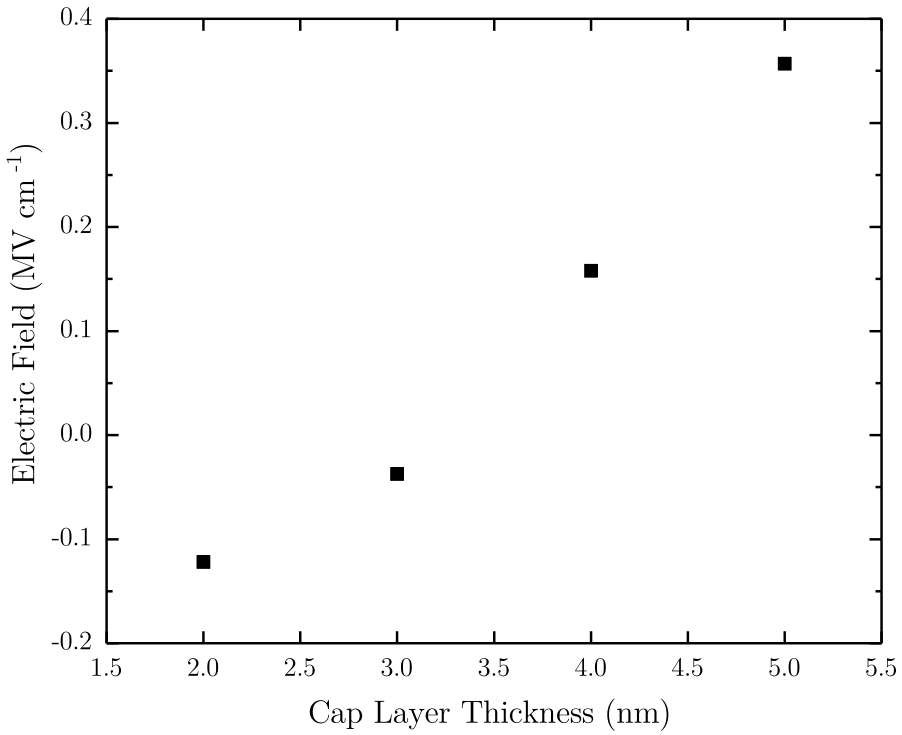

Figure 5.2: Electric fields varying with cap layer thickness, as determined from the CB and VB profiles simulated using nextnano^3.

5.4.2 Low Temperature Photoluminescence Spectroscopy

PL spectra were obtained for each of the samples using a CW laser with a photon energy of 3.815 eV as the excitation source. The excitation power density was 10 W cm^{-2} and the sample temperature was 10 K. The spectra are shown in Figure 5.3 normalised to the QW zero-phonon peak intensity. The FWHM of the QW emission peak broadens on the low energy side as the cap layer thickness increases. This broadening is shown as a function of the calculated electric field, with the corresponding cap layer thickness labelled, in Figure 5.4.

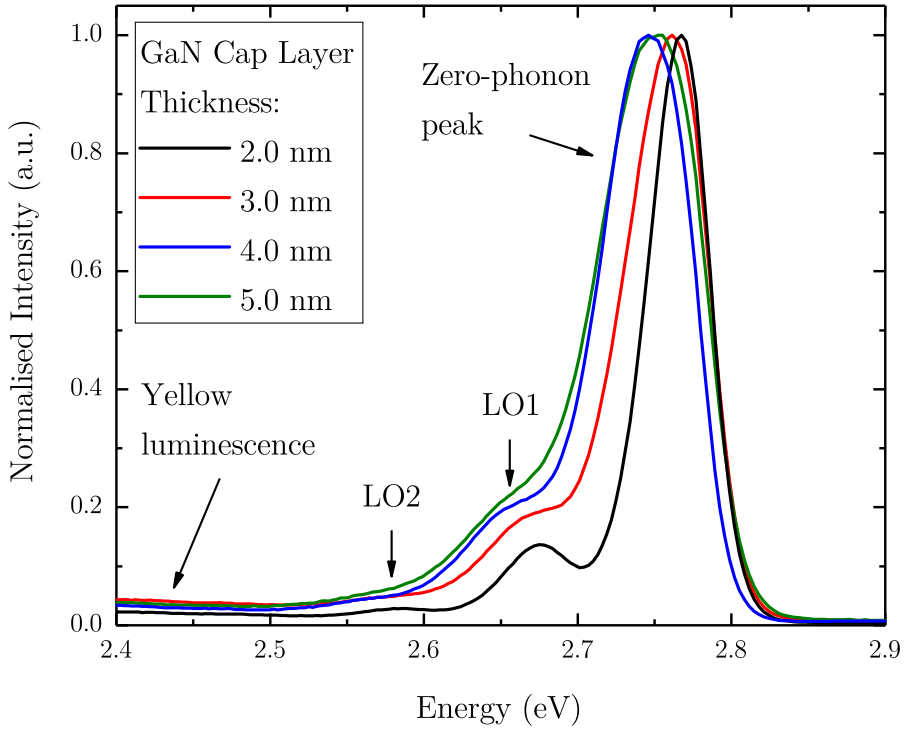

Figure 5.3: PL spectra obtained at 10 K for the samples with varying cap layer thickness. The intensities are normalised to the QW zero-phonon peak intensity for all the samples. The zero-phonon peak, first and second LO phonon replica peaks (LO1 and LO2, respectively) and the yellow luminescence band are indicated.

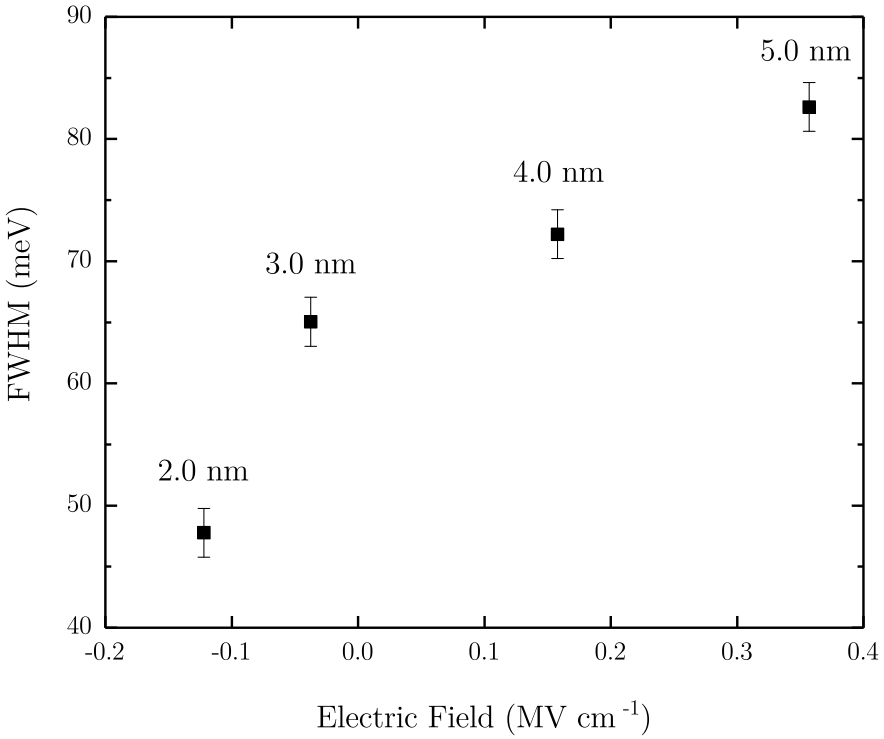

Figure 5.4: FWHM of the QW emission peak varying with electric field for the samples with varying cap layer thickness. The points are labelled with the corresponding cap layer thickness.

The FWHM of the QW emission peak increases monotonically with increasing cap layer thickness (increasing electric field strength in the direction of the strain-induced piezoelectric polarisation field). The most dramatic change in FWHM occurs between the 2 and 3 nm cap samples, where it increases by (17 ± 3) meV for a change in electric field strength of $0.0846\,\mathrm{MV\,cm^{-1}}$, compared to (7 ± 3) meV for a change of $0.0195\,\mathrm{MV\,cm^{-1}}$ (between the 3 and 4 nm cap layer samples) and (10 ± 3) meV for a change of $0.0199\,\mathrm{MV\,cm^{-1}}$ (between the 4 and 5 nm cap layer samples.

It was shown by Tanner *et al.* [6] that the amount of variation in the ground state energies of localised electrons in InGaN/GaN QWs is related to the net electric field across the QW. By comparing 3-dimensional models of InGaN QWs consisting of different random atomic configurations in the region of a QWWF, the authors reported that the electron ground state energy varies dramatically between atomic configurations where the In fraction is 15 %, while it varies much less about the mean

value for In fractions of 10 % and 25 %. For a 10 % In QW, the models showed that the electron ground state wavefunctions are generally not strongly confined to QWWFs. For a 25 % In QW, the increased piezoelectric field strength increases the confining effect of the QWWF on the electrons and they are overall more localised in these regions. For the case of the 15 % In QW, it was found that electrons were equally likely to be localised inside a QWWF as they were outside of it for a given atomic configuration. Since the recombination energy is reduced for carriers confined at these regions of increased QW width [35], this results in a broader distribution of localised electron energies and was used to explain the broader emission peak for a QW with this In fraction compared to other fractions observed experimentally by Graham *et al.* [36].

As described in Section 5.3, it is reasonable to assume that the QW In fractions are identical for all of the samples studied in this chapter. Therefore, the broadening of the emission peak shown here may be due to the localisation effects of QWWFs becoming more pronounced with increasing net electric field across the QW. The net electric fields determined by nextnano[3] for the 2 and 3 nm cap layer samples are reversed relative to the piezoelectric field (keeping in mind that this only represents the average field experienced by carriers across the QWs). It has been shown by Galtrey *et al.* [9] that the QWWFs are mainly present on the upper interfaces of InGaN/GaN QWs. The lower interface is comparatively smooth, so electrons that are drawn to this interface by a reversed electric field would still experience weaker localisation overall than for the same electric field magnitude of opposite sign.

The intensities of the LO phonon replica peaks relative to the zero-phonon peak, referred to as the Huang-Rhys factor [37], in PL spectra of InGaN/GaN QW structures are known to relate to the spatial separation of electrons and holes [36, 38]. The increasing electron-hole wavefunction separation was given as the reason for the observed increase in the Huang-Rhys factor with increasing In fraction (leading to an increasing net electric field strength) and increasing QW width in InGaN/GaN QWs

by Graham *et al.* [36] and Kalliakos *et al.* [38], respectively. The Huang-Rhys factor is therefore an informative parameter when studying variations in QW electric fields in these systems.

A multiple Gaussian function was fitted to each 10 K PL spectrum to extract the Huang-Rhys factor for each sample. The energy separations between the zero-phonon peak and the first and second LO phonon replica peaks, LO1 and LO2, respectively, as well as the FWHMs for all of the peaks, were constrained to be equal for a particular spectrum. The fitting function included a broad Gaussian peak fitted to the yellow luminescence band to account for its presence in the spectra. The fitted spectra are shown in Figure 5.5. The LO phonon replica peak energy separation was found to be (91 ± 1) meV for all of the samples. It has been shown that in QW systems where carrier localisation effects are present, the ratio, S_1, between the intensities of the zero-phonon PL peak and LO1 is not equal to that between LO1 and LO2, S_2 (or any subsequent lower energy LO phonon replica peaks) [39–41]. This is because the zero-phonon peak is caused by recombination from both strongly and weakly localised electrons and holes, while the LO phonon replica peaks originate from only strongly localised carriers. It has therefore been argued [39–41] that the true value of the Huang-Rhys factor can only be determined if at least two LO phonon replica peaks are observed. For the samples studied in this chapter, the extracted values of S_1 and S_2 are shown varying with electric field in Figure 5.6. Large errors are present on the values of S_2 due to the overlap of LO2 with the yellow luminescence band. In both cases, the sample with the 2 nm thick cap layer is found to have a significantly reduced Huang-Rhys factor compared to the other three samples; the value of S_1 lies in the range 0.18–0.21 for the samples with 3, 4 and 5 nm thick cap layers, but for the sample with the 2 nm thick cap layer the fitting gives a value for S_1 of 0.13 ± 0.01. The extracted value of S_2 is 0.08 ± 0.03 for the sample with the 2 nm thick cap layer, while the error bars give a range of 0.13–0.20 for S_2 for the other samples. As described above, and observed in InGaN/GaN QWs by Pecharromán-Gallego *et al.* [39], S_2 is

smaller than S_1 for all of the samples.

Since the QW In fractions are the same for all of the samples, the variation in Huang-Rhys factor must be caused by the changing total electric field due to the variation in cap layer thickness. This accounts for the slight overall increase in Huang-Rhys factor observed as the cap layer thickness is increased from 3–5 nm, and the dramatically reduced value for the sample with the 2 nm thick cap layer would be related to the reversal of the net electric field across that QW relative to the other samples; the primary cause of electron localisation is QWWFs [6] which mainly occur on the upper QW interface [9]. Electrons will therefore experience significantly reduced localisation effects if the electric field is reversed in some regions of the QW. This would cause a smaller average spatial separation between electrons and holes, resulting in the reduced Huang-Rhys factor.

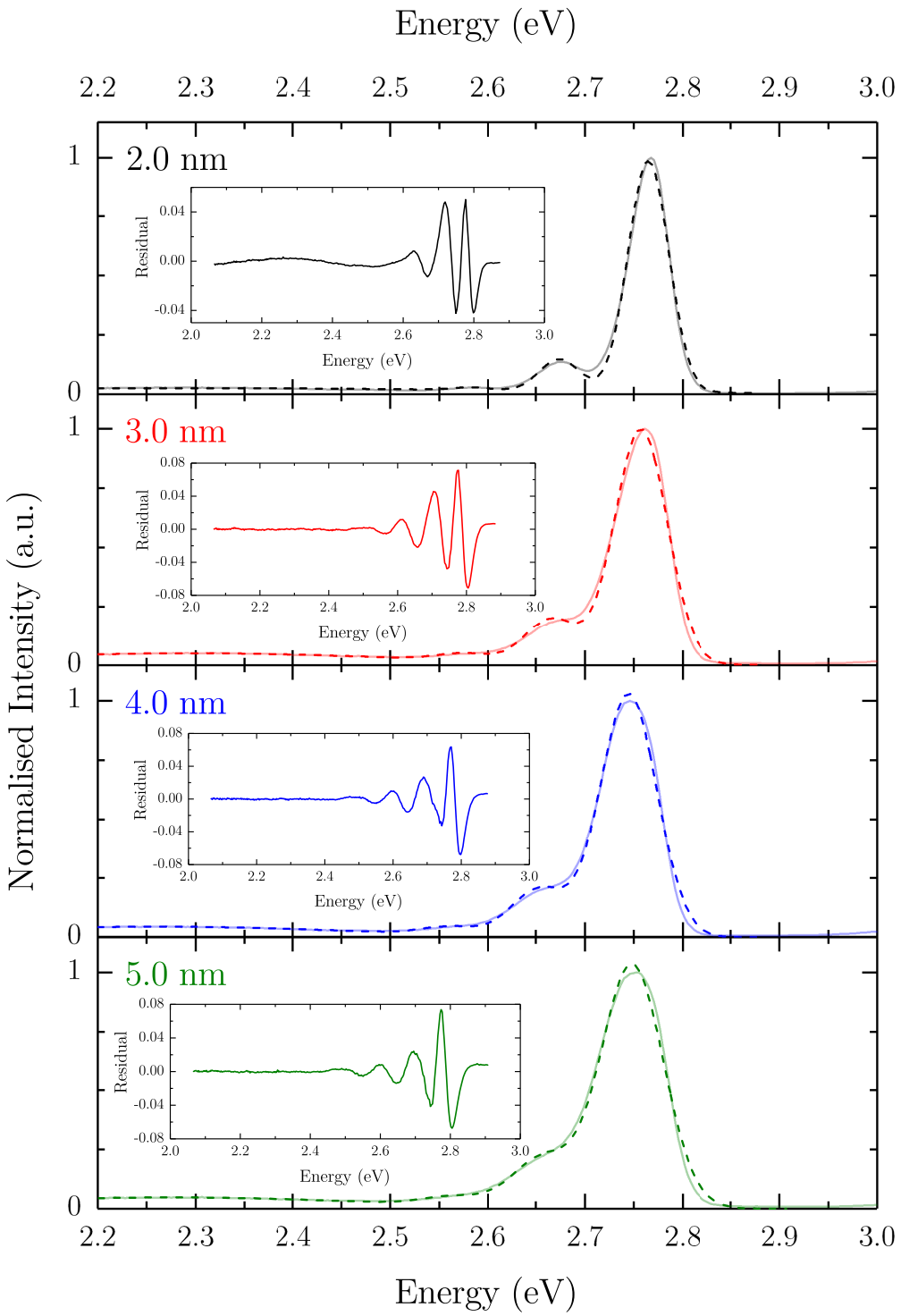

Figure 5.5: 10 K PL spectra (semi-transparent solid lines) fitted by a multiple Gaussian function (dashed lines) to extract the Huang-Rhys factors, S_1 and S_2. The cap layer thickness is as indicated on each spectrum. The fitting residuals are shown in the insets for each sample.

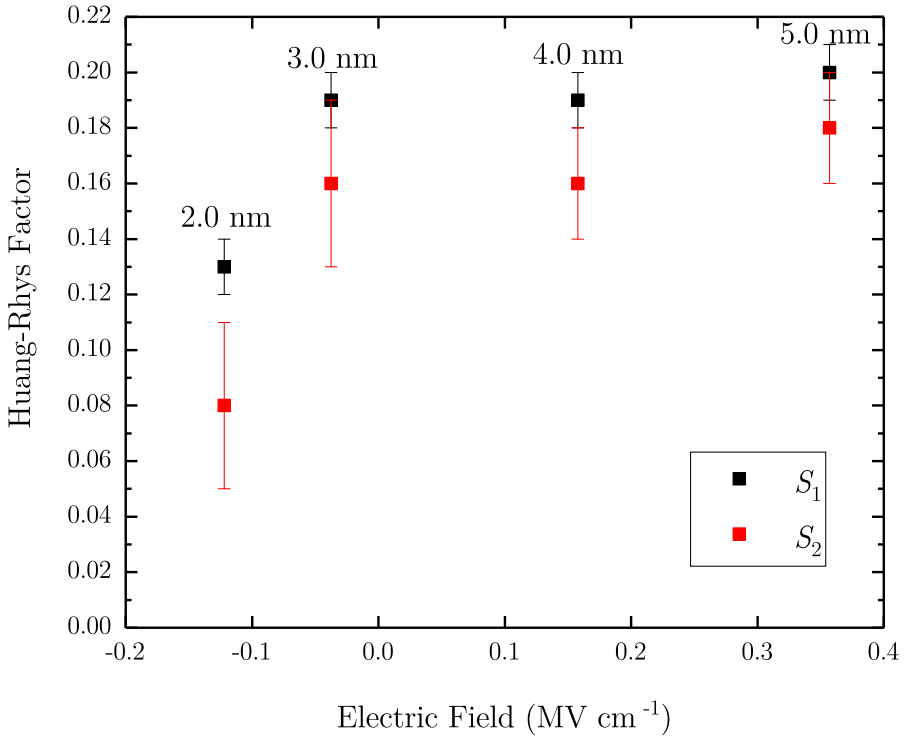

Figure 5.6: Huang-Rhys factors, S_1 and S_2, varying with the electric field across the QW. The experimental points are labelled with the corresponding cap layer thickness.

5.4.3 Photoluminescence Time Decay Measurements

The non-exponential shape of PL time decay curves measured for InGaN/GaN QWs has been related to the QW microstructural properties that give rise to separate localisation of electrons and holes by Morel *et al.* [35, 42]. PL decay curves detected at the peak emission energy, at 10 K, for the four samples with varying cap layer thickness are shown in Figure 5.7. All of the PL decay curves are non-exponential. This provides further evidence that the recombination mechanism remains fundamentally different to that reported for non-polar InGaN/GaN QWs, where exponential PL decays are attributed to the recombination of localised excitons [8, 22, 23], despite the fact that the nextnano^3 simulated band profiles suggest that the net electric fields across the QWs are very close to zero compared with other *c*-plane QWs. The time taken for the PL intensity to fall to $1/e$ of its peak value, $\tau_{1/e}$, was used as an arbitrary parameter

to compare decay times between samples at different detection energies. $\tau_{1/e}$ detected at the QW peak emission energy is shown to vary unsystematically with cap layer thickness in Figure 5.8. The longest $\tau_{1/e}$ was measured for the sample with the 2 nm thick cap layer. This can be confirmed by inspection of the PL decay curves in Figure 5.7, in which the decay curve for this sample is overall considerably longer than the others which are of relatively similar duration.

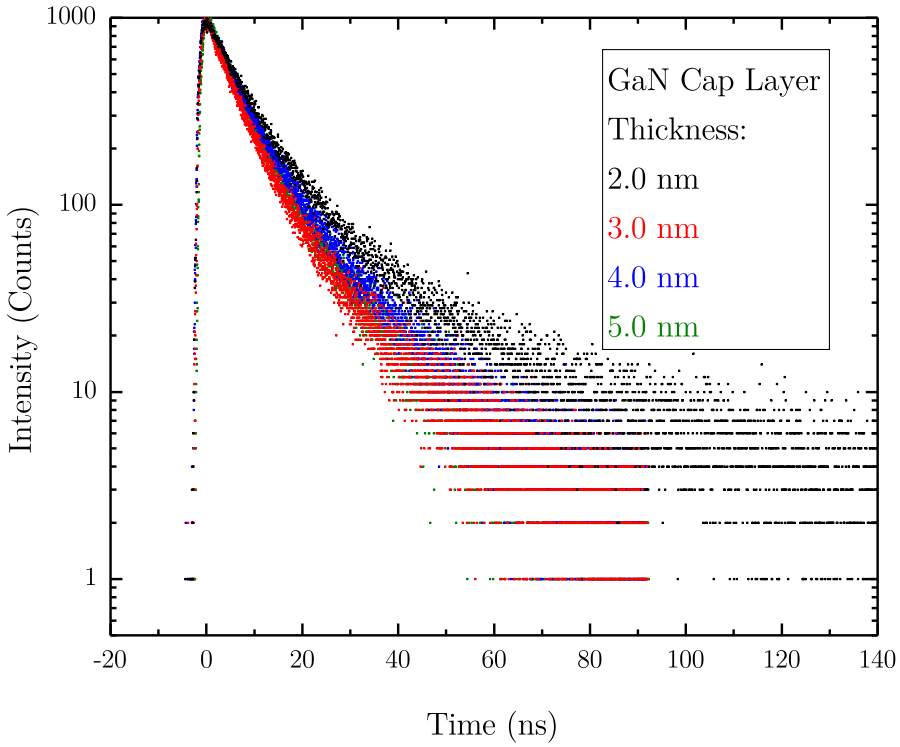

Figure 5.7: PL decay curves detected at the QW emission peak energy for the samples with varying cap layer thickness.

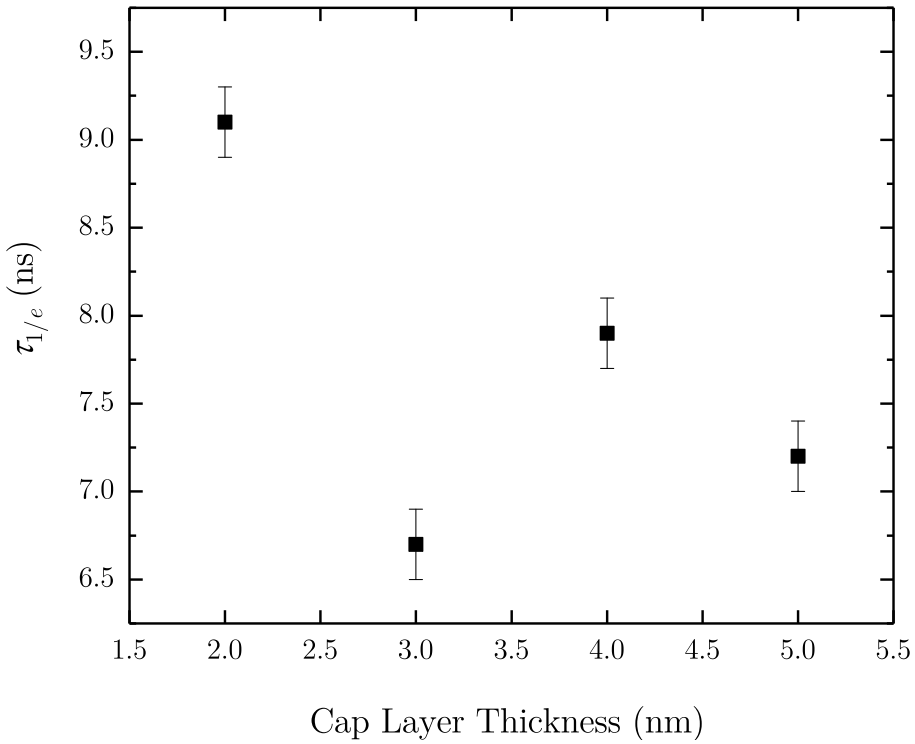

Figure 5.8: $\tau_{1/e}$ values measured at the QW peak emission energy varying with cap layer thickness.

To investigate further the effects of cap layer thickness on the PL time decay, measurements were performed varying the detection energy across the emission peaks for each sample. The variation of $\tau_{1/e}$ across the emission peak for each sample is shown in Figure 5.9. The PL spectra from Figure 5.3 have been included as a semi-transparent background for reference. For all of the samples, $\tau_{1/e}$ increases with decreasing detection energy across the QW emission peak. This is usually attributed to the locally varying QCSE where the piezoelectric polarisation field is stronger in high In content areas [35]. $\tau_{1/e}$ begins to fall as the detection energy approaches LO1 due to the overlapping high energy emission from the LO phonon replica peak [36]. The variation of $\tau_{1/e}$ is very similar between the 3, 4 and 5 nm cap layer samples, but it is much more dramatic over the same energy range for the sample with the 2 nm cap layer. At the highest detection energies, $\tau_{1/e}$ is similar for all of the samples (3.9–4.2 ns at 2.799 eV). However, it increases rapidly with decreasing detection energy for the 2 nm cap layer sample compared to the others, peaking at (11.8 ± 0.2) ns at 2.725 eV

at which detection energy $\tau_{1/e}$ lies in the range 8–9 ns for the other samples.

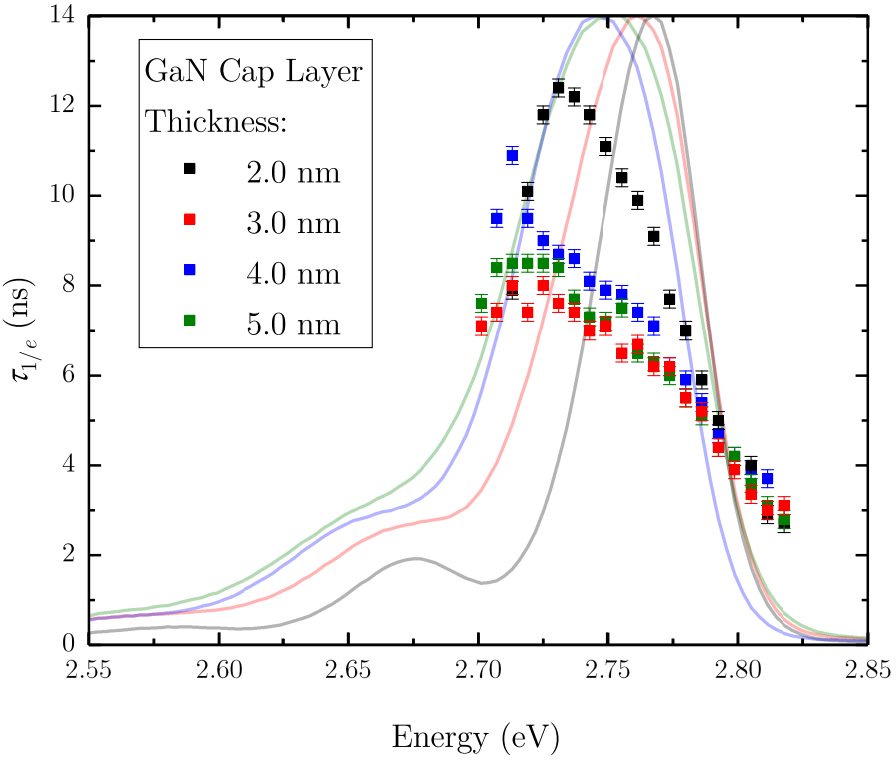

Figure 5.9: Variation of $\tau_{1/e}$ with detection energy for the samples with varying cap layer thickness. The PL spectra are included as a semi-transparent background for reference.

A possible explanation for the difference in PL decay dynamics in the 2 nm cap sample is illustrated schematically in Figure 5.10, based on the side-view isosurface plots produced from the modelling of InGaN/GaN single QWs with different QW In fractions by Tanner *et al.* [6]. The upper and lower interfaces of the QW are sketched with an exaggerated monolayer QWWF included at the top interface (the c growth direction is labelled). Red and white elliptical areas illustrate the out-of-plane ground state charge densities for electrons and holes, respectively.

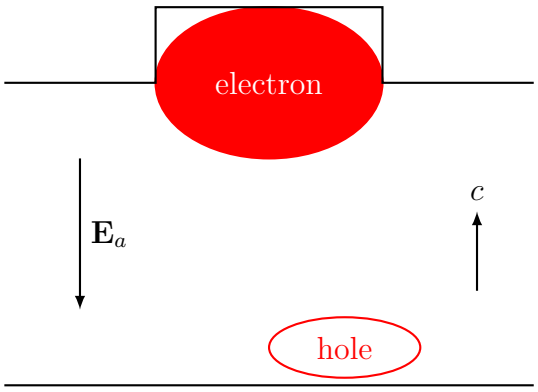

(a) Electron strongly localised at a QWWF and hole strongly localised at the opposite QW interface due to the large electric field, $\mathbf{E}_a$.

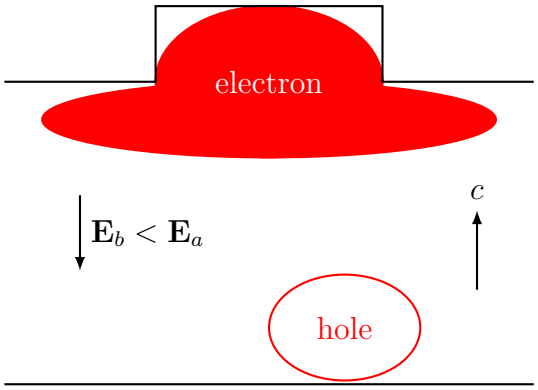

(b) Electron and hole less strongly localised at opposite interfaces due to smaller electric field, $\mathbf{E}_b$. There is a large amount of variation in the localising effect of the QWWFs, leading to a broad distribution of ground state recombination energies.

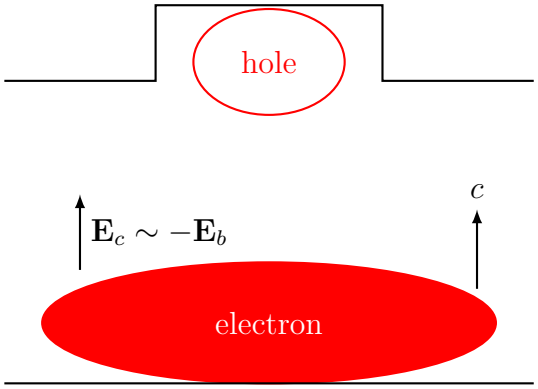

(c) Electric field, $\mathbf{E}_c$, of opposite sign leads to hole localisation at QWWF at top interface, and localisation of electron at relatively smooth bottom interface.

Figure 5.10: Schematic diagrams illustrating electron and hole localisation in the region of a QWWF for different electric fields, $\mathbf{E}_{a,b,c}$, across a QW. The directions of the electric fields and the growth direction, [0 0 0 1], are indicated. These diagrams are based on the side-view isosurface plots produced by Tanner *et al.* [6].

In Figure 5.10(a), the electron ground state charge density is strongly confined to the region of the QWWF due to the large net electric field, $\mathbf{E}_a$, across the QW. The hole charge density extends over a much smaller region than that of the electron due to the strong hole localising effect of random alloy fluctuations. The large electric field means that the positively charged hole is localised at the bottom interface of the QW. This was found to be the most commonly occurring result for different random alloy configurations of a 25 % In QW by Tanner *et al.* [6]. Figure 5.10(b) summarises some of the results calculated for a 15 % In QW [6]. The net electric field across the QW, $\mathbf{E}_b$, is smaller than in the 25 % In QW case. This means that the electron and hole ground state charge densities are not as strongly confined to the upper and lower interfaces of the QW, respectively. In the case of the electron, this has the additional consequence of reduced localisation by the QWWF in some cases. Tanner *et al.* [6] demonstrated that, for a 15 % In QW, in some random alloy configurations the electron ground state was strongly localised at the QWWF and in others it was not. In this sense, some cases could be represented as lying in an intermediate arrangement for the electrons between Figures 5.10(a) and 5.10(b). This resulted in a large distribution of electron ground state energies and may be the reason for the relatively broad PL emission peak from the 5 nm cap layer sample, with the strongest net electric field and a similar In fraction to the cited work (18 %), as described above. As the net electric field across the QW is reduced with reducing cap layer thickness, fewer electrons are strongly localised at the QWWFs and the electron ground state energy distribution becomes increasingly dominated by the weakly localised case, resulting in a narrowing emission peak. In the case of the 2 nm cap layer sample, the nextnano^3 calculations predict that the net electric field across the QW, $\mathbf{E}_c$, is of opposite sign to that of the cases calculated by Tanner *et al.* [6]. However, since these calculations neglect the QW inhomogeneity, it is possible that this reversal of the net electric field only occurs in some regions of the QW. In these regions, it would be expected that the electron and hole ground state charge densities would be localised at the bottom and top QW

interfaces, respectively, as illustrated in Figure 5.10(c). Electrons in these regions would be weakly localised due to the reduced presence of QWWFs on the bottom QW interface [9], while holes would now be susceptible to localisation at QWWFs at the top interface. This would result in a wider effective QW in these regions, leading to a reduced recombination energy as well as a reduced radiative recombination rate due to the increased QCSE. This is in agreement with the long PL decay times on the low energy side of the emission peak shown in Figure 5.9. The shorter PL decay times at higher detection energies, where $\tau_{1/e}$ is similar to the values measured for the other samples, originate from recombination in regions of the QW where the net electric field is not reversed and so the localisation effects are the same as in the other samples. The nextnano^3 simulations also predict that the net field has been reversed by a small amount in the 3 nm cap layer sample, but no evidence of this was found in the experimental work reported here. It may be the case that the field is reversed in some regions of the QW but that the system and the experimental observations are dominated by regions where it is not.

Morel *et al.* [35, 42] demonstrated that the low temperature PL decay shapes for InGaN/GaN QWs are determined by their microstructural properties (In composition fluctuations and QWWFs) which give rise to localisation potential landscapes in the plane of the QW that are separate for electrons and holes. The decay time scale is determined by the out-of-plane modulus electron-hole wavefunction overlap. By plotting PL decays on a "reduced" scale with time in units of the measured decay time, the out-of-plane dependence was removed and the decay shape was found not to vary for a given for a given QW alloy composition, indicating that the in-plane localisation landscape is identical between the QWs. PL decays detected at two different energies for each of the samples with varying cap layer thickness are shown with time, t, in units of $\tau_{1/e}$ (the "reduced" time scale from Morel *et al.* [35, 42]) in Figure 5.11. Reduced PL time decays detected on the high energy sides of the PL spectra, at 3.811 eV, are shown in Figure 5.11 (top) to be of identical shape. This indicates that recombination

at this energy occurs between electrons and holes that experience the same in-plane localisation landscape in all of the samples. Reduced PL time decays detected on the low energy sides of the spectra, at 2.713 eV, are shown in Figure 5.11 (bottom). In this case, the decay curves for the 3, 4 and 5 nm cap layer samples have similar shapes, but for the 2 nm cap layer sample it is dramatically different. This suggests that the in-plane localisation landscape is different for carriers recombining with low energies in that sample. This is consistent with the model described above in which the low energy PL is attributed to carriers localised in regions where the electric field across the QW is reversed: electrons are localised at the lower QW interface with fewer QWWFs, while holes now experience potential minima due to the QWWFs at the upper interface in addition to those caused by random alloy composition fluctuations. Again, the fact that this behaviour is restricted to the low energy side of the spectrum is likely because the electric field is only reversed in some regions of the QW. Where this is the case, the localisation of the hole at a QWWF results in a wider effective QW, leading to lower energy recombination.

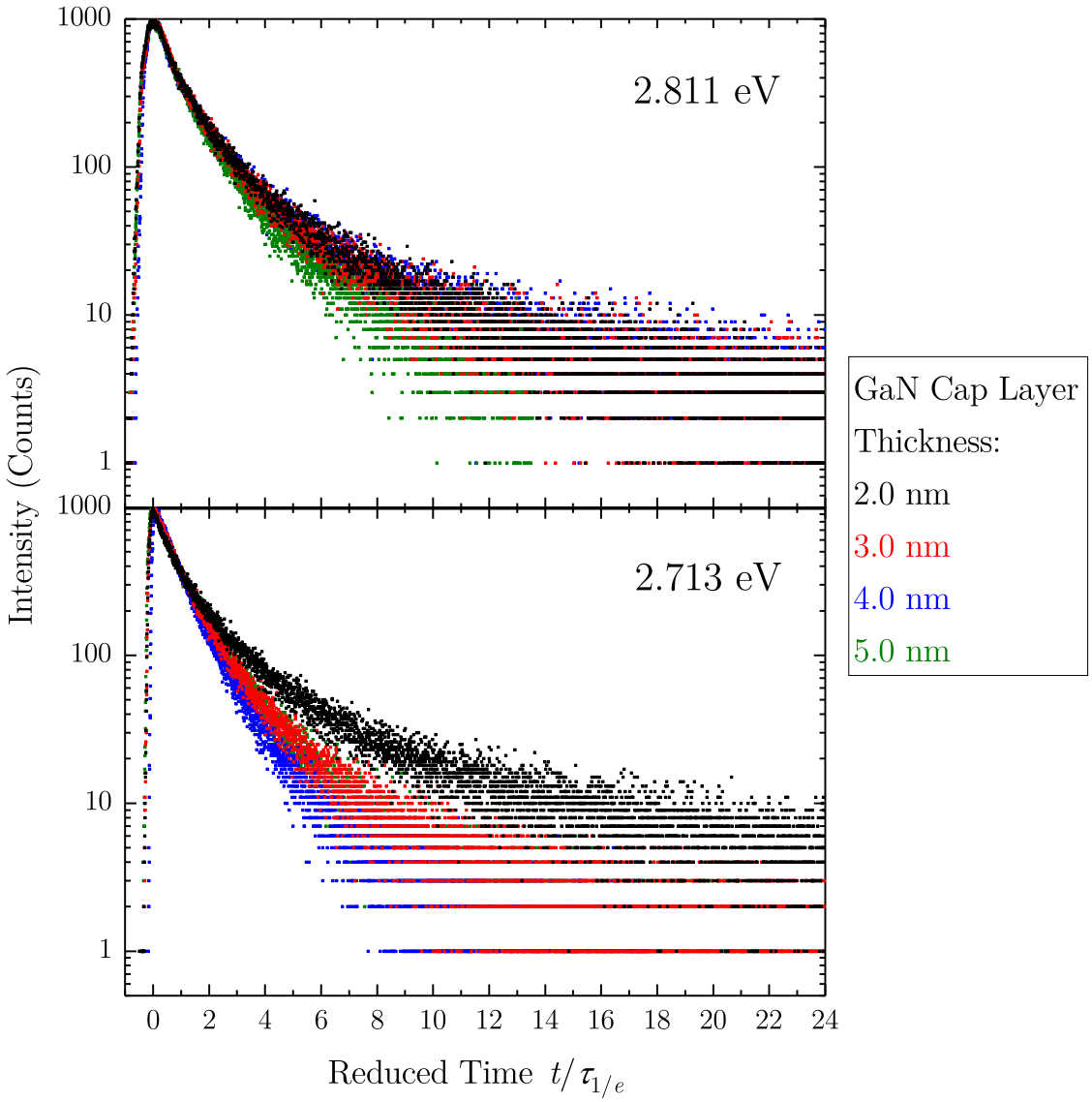

Figure 5.11: PL time decay curves plotted on a reduced time scale, in units of $\tau_{1/e}$, detected at 2.811 eV (top) and 2.713 eV (bottom).

As all of the samples studied in this chapter were grown by the 1T method (described in Section 2.4 of Chapter 2), it is likely that diffusion of In atoms into the cap layer has occurred. The characteristic length of the exponential tail of In atoms in the upper barriers of a 10-period InGaN/GaN QW structure grown by the 1T method was measured by Massabuau *et al.* [43] to be 2.1 nm. This could mean that the InGaN layer is continuous up to the sample/air interface for the 2 nm cap layer sample, at least in some regions of the QW. This would have a dramatic effect on the

in-plane electron localisation as there would be no barrier at which QWWFs could occur in these regions. Assuming that QWWFs occur to a similar degree among the rest of the samples, this could also explain the different shape of the reduced time-scale PL decay curves for the 2 nm cap layer sample as it would result in a different microstructural profile at the upper QW interface and therefore a different in-plane localisation "landscape" for electrons in this sample. If there exist regions of the QW where In atoms have not penetrated into the barrier and regions where they have, this could explain the fact that the shape of the PL decays changes only when detected on the low energy side of the emission peak; the QW width would be effectively wider in the regions with In penetration into the barrier than the rest of the QW, leading to a reduced electron-hole recombination energy due to the increased potential drop across the QW. Detailed microstructural analyses of all of these samples would be necessary to determine whether the In penetration into the barriers has caused the 2 nm cap layer sample to have gaps in some regions of the upper QW barrier, and if this makes it structurally distinct from the rest of the samples in the series, to provide experimental evidence to support or rule out this reasoning.

5.5 Summary and Conclusions

The low temperature PL emission properties of four single QW samples containing InGaN:Si ULs with varying cap layer thicknesses were investigated. Using simulated CB and VB profiles, it was predicted that the net electric field across the QW in a sample decreases with decreasing cap layer thickness due to the increasing strength of the surface depletion field. For two of the samples, the net electric field across the QWs determined from the simulated band profiles was of opposite sense to the strain-induced polarisation field. These simulations do not account for carrier localisation effects and so reflect only changes in the average electric field perpendicular to the plane of the QW.

PL spectra obtained at 10 K showed that the QW emission peak broadened on the low energy side as the cap layer thickness increased. This was attributed to the increasing variation in ground state energies for electrons with decreasing net electric field across a QW, due to the reduced degree of localisation at QWWFs for some electrons.

Huang-Rhys factors were extracted from the 10 K PL spectra. The Huang-Rhys factor increased slightly as the cap layer thickness was increased from 3–5 nm due to the increasing out-of-plane separation of electrons and holes with increasing net electric field across the QW. The Huang-Rhys factor extracted for the sample with the 2 nm thick cap layer was significantly smaller than for the other samples. This is consistent with a reversed electric field across the QW, relative to the other samples, in some parts of the QW leading to reduced electron localisation and so a smaller average spatial separation of electrons and holes both in and out of the plane of the QW.

PL time decay measurements performed at 10 K showed a similar variation in $\tau_{1/e}$ across the QW emission peak for the samples with 3, 4 and 5 nm thick cap layers, but for the 2 nm thick cap sample the $\tau_{1/e}$ values detected on the low energy side of the emission were much longer than for the other samples. This was attributed to recombination involving holes which are localised at QWWFs at the upper QW interface due to the reversed electric field. This leads to a wider effective QW, with a lower recombination energy, and an increased QCSE resulting in a longer radiative lifetime. Comparing the shapes of the PL decay curves on a reduced scale with time in units of $\tau_{1/e}$ revealed a different shape for the curves on the low energy side of the 2 nm cap layer sample, compared to decay curves detected across the full range of emission energies for the other samples. This indicates a different localisation landscape for electrons and holes recombining at low energies in this sample, according to the model of Morel *et al.* [35, 42]. This may be due to the reversal of the net electric field across some regions of the QW, since the density of QWWFs at the bottom QW interface

is expected to be lower than that at the top. Alternatively, it may be due to the penetration of In atoms into the upper QW barrier caused by the 1T growth method leading to regions of the QW where there is no upper barrier present. Detailed microstructural characterisation would be necessary to determine whether this is the case.

The results presented in this chapter provide experimental evidence that carrier localisation in *c*-plane InGaN/GaN QWs is strongly influenced by the internal electric fields, and that achieving perfectly square (that is, zero net electric field) QWs may not be possible in this system. This must be taken into careful consideration when interpreting results obtained from QWs where the net electric field is calculated to be close to zero in a 1-dimensional model, as local variations mean that the electric field is still strong enough to localise electrons and holes independently in a given region of the QW, even if the average field is zero.

5.6 References

[1] V. Fiorentini *et al.* "Effects of macroscopic polarization in III-V nitride multiple quantum wells". *Physical Review B* **60**, 12 (1999), 8849. DOI: 10.1103/PhysRevB.60.8849 (Cited on pages 121, 122, 129).

[2] O. Mayrock *et al.* "Polarization charge screening and indium surface segregation in (In,Ga)N/GaN single and multiple quantum wells". *Physical Review B* **62**, 24 (2000), 16870. DOI: 10.1103/PhysRevB.62.16870 (Cited on pages 121, 122, 129).

[3] T. Takeuchi *et al.* "Determination of piezoelectric fields in strained GaInN quantum wells using the quantum-confined Stark effect". *Applied Physics Letters* **73**, 12 (1998), 1691. DOI: 10.1063/1.122247 (Cited on pages 121, 129).

[4] H. Gotoh *et al.* "Piezoelectric effects on photoluminescence properties in 10-nm-thick InGaN quantum wells". *Applied Physics Letters* **83**, 23 (2003), 4791. DOI: 10.1063/1.1632539 (Cited on pages 121, 129).

[5] T. H. Ngo *et al.* "Internal quantum efficiency in yellow-amber light emitting AlGaN-InGaN-GaN heterostructures". *Applied Physics Letters* **107**, 12 (2015), 122103. DOI: 10.1063/1.4931624 (Cited on pages 121, 122, 129).

[6] D. S. P. Tanner *et al.* "Random alloy fluctuations and structural inhomogeneities in c-plane InGaN quantum wells: theory of ground and excited electron and hole states". *RSC Advances* **6**, 69 (2016), 64513. DOI: 10.1039/C6RA07540A (Cited on pages 121, 123, 129, 131, 134, 139, 140, 141).

[7] D. Watson-Parris *et al.* "Carrier localization mechanisms in InGaN/GaN quantum wells". *Physical Review B* **83**, 11 (2011), 115321. DOI: 10.1103/PhysRevB.83.115321 (Cited on pages 121, 123, 129).

[8] P. Dawson *et al.* "The nature of carrier localisation in polar and nonpolar InGaN/GaN quantum wells". *Journal of Applied Physics* **119**, 18 (2016), 181505. DOI: 10.1063/1.4948237 (Cited on pages 121, 123, 124, 129, 136).

[9] M. J. Galtrey *et al.* "Three-dimensional atom probe analysis of green- and blue-emitting InGaN/GaN multiple quantum well structures". *Journal of Applied Physics* **104**, 1 (2008), 013524. DOI: 10.1063/1.2938081 (Cited on pages 121, 123, 132, 134, 142).

[10] H. Zhao *et al.* "Growths of staggered InGaN quantum wells light-emitting diodes emitting at 520-525 nm employing graded growth-temperature profile". *Applied Physics Letters* **95**, 6 (2009), 061104. DOI: 10.1063/1.3204446 (Cited on pages 122, 124, 125).

[11] W. Qi *et al.* "Effects of thickness ratio of InGaN to GaN in superlattice strain relief layer on the optoelectrical properties of InGaN-based green LEDs grown

on Si substrates". *Journal of Applied Physics* **122**, 8 (2017), 084504. DOI: 10.1063/1.5000134 (Cited on page 122).

[12] M. Auf der Maur *et al.* "Efficiency Drop in Green InGaN/GaN Light Emitting Diodes: The Role of Random Alloy Fluctuations". *Physical Review Letters* **116**, 2 (2016), 027401. DOI: 10.1103/PhysRevLett.116.027401 (Cited on page 122).

[13] M.-H. Kim *et al.* "Origin of efficiency droop in GaN-based light-emitting diodes". *Applied Physics Letters* **91**, 18 (2007), 183507. DOI: 10.1063/1.2800290 (Cited on pages 122, 124, 128).

[14] Z.-H. Zhang *et al.* "InGaN/GaN multiple-quantum-well light-emitting diodes with a grading InN composition suppressing the Auger recombination". *Applied Physics Letters* **105**, 3 (2014), 033506. DOI: 10.1063/1.4891334 (Cited on pages 122, 124, 125).

[15] D. S. Meyaard *et al.* "Identifying the cause of the efficiency droop in GaInN light-emitting diodes by correlating the onset of high injection with the onset of the efficiency droop". *Applied Physics Letters* **102**, 25 (2013), 251114. DOI: 10.1063/1.4811558 (Cited on page 122).

[16] D.-P. Han *et al.* "Nonradiative recombination mechanisms in InGaN/GaN-based light-emitting diodes investigated by temperature-dependent measurements". *Applied Physics Letters* **104**, 15 (2014), 151108. DOI: 10.1063/1.4871870 (Cited on page 122).

[17] X. Meng *et al.* "Study on efficiency droop in InGaN/GaN light-emitting diodes based on differential carrier lifetime analysis". *Applied Physics Letters* **108**, 1 (2016), 013501. DOI: 10.1063/1.4939593 (Cited on page 122).

[18] D.-P. Han *et al.* "Carrier accumulation in the active region and its impact on the device performance of InGaN-based light-emitting diodes". *Applied Physics Express* **10**, 12 (2017), 122101. DOI: 10.7567/APEX.10.122101 (Cited on page 122).

[19] D. Biswas *et al.* "Constructive and comprehensive studies on the advantages of using staggered InxGa1-xN/InyGa1-yN QWs in LEDs". *Optical Materials* **66** (2017), 367. DOI: 10.1016/j.optmat.2017.02.028 (Cited on pages 122, 124, 125).

[20] R. Vaxenburg *et al.* "The role of polarization fields in Auger-induced efficiency droop in nitride-based light-emitting diodes". *Applied Physics Letters* **103**, 22 (2013), 221111. DOI: 10.1063/1.4833915 (Cited on pages 122, 124, 125).

[21] P. H. Pathak *et al.* "Visible Light Communication, Networking, and Sensing: A Survey, Potential and Challenges". *IEEE Communications Surveys & Tutorials* **17**, 4 (2015), 2047. DOI: 10.1109/COMST.2015.2476474 (Cited on page 122).

[22] S. Schulz *et al.* "Structural, electronic, and optical properties of m-plane InGaN/GaN quantum wells: Insights from experiment and atomistic theory". *Physical Review B* **92**, 23 (2015), 235419. DOI: 10.1103/PhysRevB.92.235419 (Cited on pages 123, 124, 136).

[23] S. Marcinkevičius *et al.* "Photoexcited carrier recombination in wide m -plane InGaN/GaN quantum wells". *Applied Physics Letters* **103**, 11 (2013), 111107. DOI: 10.1063/1.4820839 (Cited on pages 123, 124, 136).

[24] T. Detchprohm *et al.* "Green light emitting diodes on a-plane GaN bulk substrates". *Applied Physics Letters* **92**, 24 (2008), 241109. DOI: 10.1063/1.2945664 (Cited on page 123).

[25] S. F. Chichibu *et al.* "Localized exciton dynamics in strained cubic In0.1Ga0.9N/GaN multiple quantum wells". *Applied Physics Letters* **79**, 26 (2001), 4319. DOI: 10.1063/1.1428404 (Cited on page 124).

[26] S. Li *et al.* "Room temperature green light emission from nonpolar cubic InGaN/GaN multi-quantum-wells". *Applied Physics Letters* **90**, 7 (2007), 071903. DOI: 10.1063/1.2475564 (Cited on page 124).

[27] C. J. M. Stark *et al.* "Green cubic GaInN/GaN light-emitting diode on microstructured silicon (100)". *Applied Physics Letters* **103**, 23 (2013), 232107. DOI: 10.1063/1.4841555 (Cited on page 124).

[28] N. G. Young *et al.* "Polarization field screening in thick (0001) InGaN/GaN single quantum well light-emitting diodes". *Applied Physics Letters* **108**, 6 (2016), 061105. DOI: 10.1063/1.4941815 (Cited on pages 124, 128).

[29] P. Prajoon *et al.* "Investigation of efficiency enhancement in InGaN MQW LED with compositionally step graded GaN/InAlN/GaN multi-layer barrier". *Superlattices and Microstructures* **116** (2018), 71. DOI: 10.1016/j.spmi.2018.02.008 (Cited on page 125).

[30] R. A. Oliver *et al.* "The impact of gross well width fluctuations on the efficiency of GaN-based light emitting diodes". *Applied Physics Letters* **103**, 14 (2013), 141114. DOI: 10.1063/1.4824193 (Cited on pages 125, 126).

[31] C. Ferrari *et al.* "InGaAs/GaAs strained single quantum well characterization by high resolution X-ray diffraction". *Journal of Crystal Growth* **126**, 1 (1993), 144. DOI: 10.1016/0022-0248(93)90235-O (Cited on page 126).

[32] S. Birner *et al.* "nextnano: General Purpose 3-D Simulations". *IEEE Transactions on Electron Devices* **54**, 9 (2007), 2137. DOI: 10.1109/TED.2007.902871 (Cited on page 127).

[33] M. J. Davies *et al.* "The effects of Si-doped prelayers on the optical properties of InGaN/GaN single quantum well structures". *Applied Physics Letters* **105**, 9 (2014), 092106. DOI: 10.1063/1.4894834 (Cited on page 128).

[34] S. Schulz *et al.* "Atomistic analysis of the impact of alloy and well-width fluctuations on the electronic and optical properties of InGaN/GaN quantum wells". *Physical Review B* **91**, 3 (2015), 035439. DOI: 10.1103/PhysRevB.91.035439 (Cited on page 129).

[35] A. Morel *et al.* "Donor-acceptor-like behavior of electron-hole pair recombinations in low-dimensional (Ga,In)N/GaN systems". *Physical Review B* **68**, 4 (2003), 045331. DOI: 10.1103/PhysRevB.68.045331 (Cited on pages 132, 136, 138, 142, 146).

[36] D. M. Graham *et al.* "Optical and microstructural studies of InGaN/GaN single-quantum-well structures". *Journal of Applied Physics* **97**, 10 (2005), 103508. DOI: 10.1063/1.1897070 (Cited on pages 132, 133, 138).

[37] K. Huang and A. Rhys. "Theory of Light Absorption and Non-Radiative Transitions in F-Centres". *Proceedings of the Royal Society A: Mathematical, Physical and Engineering Sciences* **204**, 1078 (1950), 406. DOI: 10.1098/rspa.1950.0184 (Cited on page 132).

[38] S. Kalliakos *et al.* "Large size dependence of exciton-longitudinal-optical-phonon coupling in nitride-based quantum wells and quantum boxes". *Applied Physics Letters* **80**, 3 (2002), 428. DOI: 10.1063/1.1433165 (Cited on pages 132, 133).

[39] R. Pecharromán-Gallego *et al.* "Investigations of phonon sidebands in InGaN/GaN multi-quantum well luminescence". *Materials Science and Engineering: B* **93**, 1-3 (2002), 94. DOI: 10.1016/S0921-5107(02)00024-7 (Cited on page 133).

[40] I. Brener *et al.* "Particle localization and phonon sidebands in GaAs/AlGaAs multiple quantum wells". *Physical Review B* **46**, 12 (1992), 7927. DOI: 10.1103/PhysRevB.46.7927 (Cited on page 133).

[41] D. Mowbray *et al.* "Optical spectroscopy of AlGaInP based wide band gap quantum wells". *Superlattices and Microstructures* **15**, 3 (1994), 313. DOI: 10.1006/spmi.1994.1060 (Cited on page 133).

[42] A. Morel *et al.* "Two-dimensional pseudo-donor-acceptor-pairs model of recombination dynamics in InGaN/GaN quantum wells". *Physica E: Low-dimensional Systems and Nanostructures* **17** (2003), 64. DOI: 10.1016/S1386-9477(02)00762-2 (Cited on pages 136, 142, 146).

[43] F. C.-P. Massabuau *et al.* "Investigation of unintentional indium incorporation into GaN barriers of InGaN/GaN quantum well structures". *physica status solidi (b)* **252**, 5 (2015), 928. DOI: 10.1002/pssb.201451543 (Cited on page 144).

Chapter 6

High Power Density Photoluminescence Studies of InGaN/GaN Single Quantum Wells

6.1 Introduction

In recent years, LEDs based on group III-nitride QW structures have become a popular alternative to incandescent and fluorescent lamps for use in domestic, commercial and civic lighting applications [1–3]. However, their widespread adoption remains hindered by the phenomenon known as efficiency droop [1, 4–29]. This is where the LED power conversion efficiency drops with increasing driving current at high current densities, meaning that LED chips must be operated at relatively low current densities. This drives up initial implementation costs as more LED chips are required to achieve a given total lumen output [4].

As well as in EL measurements (that is, LEDs), efficiency droop has been observed in CL and PL experiments. This means that the phenomenon must, at least in part, be due to a falling IQE with increasing excitation power density and not just related to current injection and light extraction efficiencies [1].

The physical origins of the efficiency droop remain hotly debated, with proposed mechanisms including Auger recombination [4–14], carrier leakage from QWs [15–20] and carrier delocalisation [21–29]. There have also been several reports of a high energy broadening, or high energy band (HEB), in emission spectra from InGaN/GaN QWs at high excited carrier densities [14, 18–20, 23, 24, 26–29]. This is often observed under the conditions that lead to efficiency droop and so is usually studied in this context. Proposals for the carrier dynamics involved in the HEB emission vary from Auger recombination [14] to recombination involving carriers outside of the QW confining potential [18–20] to recombination involving delocalised or weakly localised carriers [23, 24, 26–29]. In this work, a detailed study of the decay dynamics of the HEB is presented, and a comparison is made to the behaviour of semiconductor QDs.

6.2 Proposed Mechanisms for Efficiency Droop

Several mechanisms have been suggested as the main cause of efficiency droop. In this section, three of these mechanisms (Auger recombination, carrier leakage and carrier delocalisation) are summarised as these have also been invoked in explanations for the cause of the HEB emission.

6.2.1 Auger Recombination

One process suggested as the main cause of the efficiency droop in III-nitride semiconductors is Auger recombination. As illustrated in Figure 6.1, this is when the energy released following the recombination of an electron-hole pair is transferred to another carrier (either an electron or a hole) and then dissipated through the emission of phonons [30]. While evidence of Auger recombination has been observed in many semiconductors [30–34], its role in the phenomenon of efficiency droop in InGaN/GaN QWs remains the subject of debate.

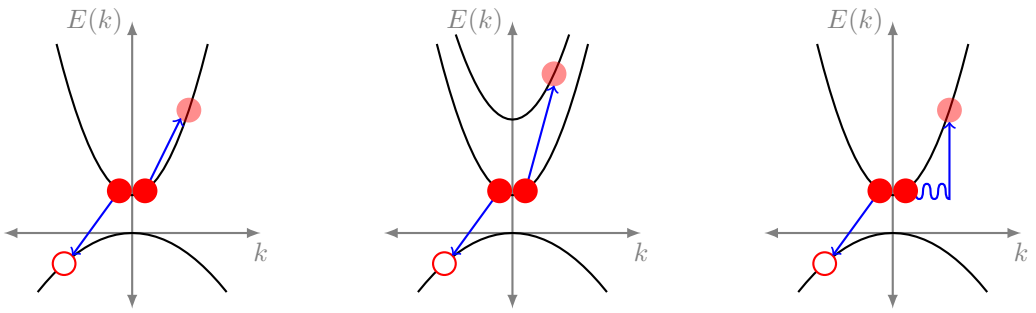

Figure 6.1: Different types of Auger recombination involving two electrons (filled red circles) and a hole (open red circles). (a): Intra-band Auger recombination, where the electron is scattered to an unoccupied part of the lowest energy CB. (b): Inter-band Auger recombination, where the electron is scattered to a higher energy CB. (c): Indirect Auger recombination, in which the energy transfer is mediated through alloy and phonon scattering processes. Adapted from Kioupakis *et al.* [7].

Shen *et al.* [5] proposed an empirical rate equation model to study the efficiency droop in LEDs. In the steady state condition, the change in carrier density with time, t, in an LED is given by

$$\frac{\mathrm{d}n}{\mathrm{d}t} = G - R = 0 \tag{6.1}$$

where G is the generation rate, R is the total recombination rate and n is the equilibrium electron density. It is assumed that $n = p$, where p is the equilibrium hole density, as the material is under optical excitation where the absorption of a photon results in the generation of an electron-hole pair.

The electron and hole radiative recombination rate, R_{rad}, is proportional to n and p since both an electron and a hole must be present for the process to take place:

$$R_{\mathrm{rad}} = Bnp = Bn^2 \tag{6.2}$$

where B is the radiative recombination coefficient.

Non-radiative recombination due to defect states, referred to as Shockley-Read-Hall (SRH) recombination, is described as having a rate, R_{SRH}, proportional to n (or

p),

$$R_{\mathrm{SRH}} = An \tag{6.3}$$

where A is the SRH recombination coefficient. Here it is assumed that the defect states are close in energy to the CB minimum and far from the VB maximum (or vice versa), so that electrons (or holes) are captured quickly into these states and the recombination rate depends on the capture rate of the hole (or electron), and that the transition probability is the same for all hole (or electron) and defect states [35]. This is illustrated in Figure 6.2.

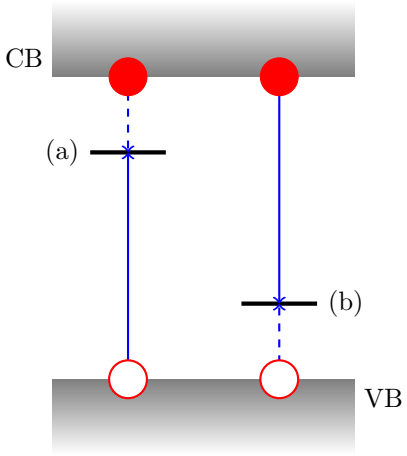

Figure 6.2: Diagram illustrating SRH recombination. Electrons and holes are represented by filled and open red circles, respectively. In (a), a defect state sits close to the CB minimum, so the electron is captured quickly. The rate of SRH recombination is then governed by the slower capture rate of the hole at the same defect state. In (b), the analogous case for a defect state close to the VB maximum is shown.

The Auger recombination rate, R_{Aug}, requires three carriers to be present (as described above and illustrated in figure 6.1, it depends on n^2p or np^2), so it is assumed to be proportional to n^3 with the Auger recombination coefficient designated as C:

$$R_{\mathrm{Aug}} = Cn^3. \tag{6.4}$$

R is therefore given by

$$\begin{aligned} R &= R_{\mathrm{SRH}} + R_{\mathrm{rad}} + R_{\mathrm{Aug}} \\ &= An + Bn^2 + Cn^3 \end{aligned} \tag{6.5}$$

and the IQE, η_{IQE}, defined as the fraction of injected carriers which recombine radiatively in the QW, becomes

$$\eta_{\mathrm{IQE}} = \frac{Bn^2}{An + Bn^2 + Cn^3}. \tag{6.6}$$

This is referred to as the ABC model [14, 36]. For LEDs, the generation rate in equation 6.1 is given by

$$G = \frac{\eta_{\mathrm{inj}} J}{qd} \tag{6.7}$$

where d is the QW thickness, q is the electron charge, J is the injected current density and η_{inj} is the carrier injection efficiency [5].

The magnitude of C, and therefore that of the role played by the Auger effect in carrier recombination in LEDs, can be determined by fitting Equation 6.1 (with R and G as defined by Equations 6.5 and 6.7, respectively) to curves generated by efficiency measurements at various injected carrier densities. Using this method, Shen *et al.* [5] determined a value for C in the range (1.4–2) $\times 10^{-30}\,\mathrm{cm^6\,s^{-1}}$ for InGaN epitaxial layers with various In fractions. The authors claimed that this value accounts for the current densities at which peak IQE values are usually measured. While many groups have applied the ABC model in studies of the efficiency droop in QWs under optical [5, 9, 14] and electrical [1, 37–40] injection, this approach makes no distinction between Auger recombination and other possible loss mechanisms. This has meant that attempts to calculate C theoretically have been necessary to determine the validity of this treatment [41, 42]. Many-body calculations performed by Hader *et al.* [41] gave $C \sim 10^{-34}\,\mathrm{cm^6\,s^{-1}}$, which is much smaller than the values typically

determined by fitting the ABC model to experimental results [5, 14, 37–39]. This has led [9, 43] to several groups proposing models to account for this discrepancy, some of which are described in this section.

It has been suggested [44–47] that the Auger recombination is enhanced in InGaN/GaN QWs due to the reduced effective volume caused by the localisation of carriers at potential minima, as discussed in Chapter 2. This leads to higher local carrier densities than would otherwise be estimated by assuming that carriers are uniformly distributed within the nominal active region volume, which could make Auger recombination more likely. In all of these works, however, the ABC fitting was still applied to the efficiency curves using one uniform carrier density and proportionality to n^3 was still assumed. Calculations by Hader *et al.* [35, 41, 48] showed that phase space filling effects lead to the Auger recombination rate becoming proportional to n^2 at high ($\sim 10^{12}\,\mathrm{cm}^{-2}$) carrier densities. In any case, the reduced effective volume treatment still relies on a single value for C that is determined from a large number of local potential minima which would presumably not be identical.

Delaney *et al.* [6] performed first-principles density-functional theory and many-body-perturbation theory to show that different types of Auger recombination involving two electrons and a hole dominate at high injected carrier densities depending on the bandgap of the material in question. For narrow ($< 1.5\,\mathrm{eV}$) bandgaps, intra-band Auger recombination (illustrated in Figure 6.1(a)), in which an electron is scattered to an unoccupied part of the lowest energy CB, was reported to be the dominant process. For larger bandgap materials inter-band Auger recombination, where the electron is scattered to a higher energy CB (Figure 6.1(b)), was said to dominate. The value of C for inter-band Auger recombination was calculated to vary with bandgap, with a peak value of $\sim 2 \times 10^{-30}\,\mathrm{cm}^6\,\mathrm{s}^{-1}$ centred around 2.5 eV, and therefore was said to have a strong effect in InGaN alloys. However, efficiency droop has been observed in group III-nitride-based structures emitting light at a wide range of energies [20, 21, 39, 49, 50] which are not sufficiently accounted for in the conclusions of Delaney *et al.*

[6]. This work was disputed by Bertazzi *et al.* [42], who calculated a peak value for C of $\sim 10^{-32}\,\mathrm{cm}^6\,\mathrm{s}^{-1}$ centred on 2.9 eV for a random InGaN bulk alloy using a virtual crystal approximation. The reduction in C by a factor of $\sim$100 for the random alloy treatment led the authors to conclude that Auger recombination plays a negligible role in the efficiency droop.

Kioupakis *et al.* [7, 8] performed atomistic first-principles calculations to demonstrate that the disordered nature of InGaN alloys and the strong carrier-phonon coupling lead to enhanced indirect Auger recombination, where the process is mediated through alloy and phonon scattering, respectively (Figure 6.1(c)). These processes cause C to increase smoothly with decreasing InGaN bandgap energy (increasing In fraction) and with increasing temperature. This is in contrast to the peak at 2.5 eV calculated by Delaney *et al.* [6]. The authors concluded that the additional momentum provided by the scattering processes makes this form of Auger recombination far more likely than direct Auger recombination due to the restriction of the latter by momentum conservation.

Several authors have claimed to have observed direct experimental evidence of Auger recombination [4, 9–12]. Binder *et al.* [9] grew MQW structures with periods of alternating green- and UV-emitting QWs and performed PL spectroscopy on them using a blue laser as the excitation source. Peaks in the green and UV region of the emission spectrum were observed and attributed to recombination involving the QWs. Since the UV emission energy was higher than that of the excitation light, the authors stated that this was evidence of the generation of "hot" electrons and holes by Auger recombination in the green-emitting QW which could overcome the QW energy barriers and recombine in the UV-emitting QW. The authors argued that the 7 nm QW barriers grown in these structures were sufficiently wide that other carrier escape processes which might lead to similar effects, such as quantum tunnelling, could be ignored. The IQE of the combined green- and UV-emitting QWs was compared with that of the green-emitting QWs alone, and it was shown that efficiency droop occurs

only when considering the latter case. By showing that this drop in IQE exhibited a dependence on the cube of the injected carrier density, the authors concluded that the carriers recombining in the UV-emitting QWs must have been generated by Auger recombination in the green-emitting QWs.

Iveland *et al.* [4, 10, 11] reported direct measurement of Auger electrons by electron emission spectroscopy. The kinetic energies of electrons emitted into vacuum from the p contact layer of a single QW LED under different injection currents were analysed. For low injection currents, a single peak in the electron energy spectrum was observed and attributed to electrons which were photoexcited by light from the LED [11]. When the LED was driven into the efficiency droop regime, additional peaks were observed at higher energies on the spectrum and were attributed to electrons which had higher kinetic energies following the energy transferred to them by the Auger recombination process. These electrons were concluded to have been promoted to a higher energy CB valley, and it was via this valley that they were eventually transported to the p contact layer. The experimental results of Iveland *et al.* [4, 10] were reproduced in Monte Carlo simulations by Sadi *et al.* [13], who concluded that only electron transport via higher energy CB valleys would lead to the observed rate of emitted electrons since other electron transport mechanisms, such as electron leakage from the QW, would not generate sufficient electrons in the p contact layer according to the calculations. A similar experiment was performed more recently by Williams *et al.* [12] using an "uncapped" QW, where a 3 nm thick layer of $In_{0.12}Ga_{0.88}N$ was exposed to vacuum. This was intended to remove the possibility of inelastic scattering, which the authors claimed complicated the results of Iveland *et al.* [4, 10, 11] due to the large amount of capping material through which the electrons had to travel before being emitted into vacuum in that work. The "uncapped" QW was excited optically and time-resolved photoemission spectra were fitted by the ABC model to give $C = (5.0 \pm 0.2) \times 10^{-25}\,\mathrm{cm^6\,s^{-1}}$. The authors claimed that the determination of C by this method measures directly the time-dependent carrier density, and so is

preferable to analyses of the efficiencies of structures where it is determined indirectly by measuring the luminescence intensity.

Shahmohammadi *et al.* [14] reported a broadening on the high energy side of the PL spectra for a variety of different QW structures under high excitation power densities. In TRPL spectroscopy experiments, the FWHMs of the emission spectra of *c*-plane InGaN/GaN and GaN/AlGaN QWs were observed to reduce with increasing time for an initial excited carrier density of $10^{13}\,\mathrm{cm}^{-2}$. Under these conditions, the InGaN/GaN QW underwent efficiency droop but the GaN/AlGaN QW did not. The same observations were made for two *m*-plane InGaN/GaN QWs, one of which was grown at a lower temperature than the other which the authors claimed promoted a higher degree of alloy disorder. The difference in alloy disorder was confirmed in temperature dependent PL experiments at low excited carrier densities by the fact that the lower growth temperature *m*-plane QW showed a more pronounced S-shaped peak energy dependence, as well as having a broader FWHM than the other QW at all temperatures. Efficiency droop was observed for the more disordered *m*-plane QW but not for the less disordered one. The authors suggested that enhanced localisation effects due to disorder were related to the efficiency droop, where the disordered InGaN alloy QW was compared to the uniform GaN QW in the GaN/AlGaN structure. Based on previous work on the same GaN/AlGaN QW [51], the authors attributed the high energy broadening at high excited carrier densities to a transition from the creation of excitons in the QW to that of an electron-hole plasma. In the case of the disordered QWs in the work of Shahmohammadi *et al.* [14], both structures exhibited a fast initial PL decay component in their time-resolved spectrally integrated intensities. The ABC model was fitted to these decays and Auger recombination was concluded to be the dominant process as non-zero values of C were required to achieve good fits to the experimental data for the disordered QWs. Increased disorder in the QW was said to lead to enhanced indirect Auger recombination by scattering processes based on the work of Kioupakis *et al.* [7, 8]. Importantly, in the analysis of the PL decay

of the HEB performed by Shahmohammadi *et al.* [14], any dependence of the decay dynamics on the emission energy would have been ignored in the application of the ABC model to the spectrally integrated intensities.

6.2.2 Carrier Leakage

Another proposed cause of efficiency droop is the leakage of carriers from QWs [15–20]. Evidence has been presented for the loss of carriers, initially captured by a QW, before recombination can occur due to thermionic emission [52, 53] or quantum tunnelling [53]. It has also been suggested that droop is caused by a reduced efficiency of carrier capture by QWs altogether [15].

Schubert *et al.* [16] measured a reverse photocurrent across an InGaN/GaN MQW LED that was excited optically below the bandgap of the GaN barrier layers. This photocurrent increased with increasing optical excitation power density, and was attributed to carriers escaping the confinement of the QWs and being swept along by the electric field that exists between the *n*- and *p*-type regions in an LED. The authors concluded that the impact of carrier escape from QWs should be taken into account as a contributing factor in efficiency droop.

It has been reported that QWs with improved carrier confinement can be designed and that the efficiency droop is partially suppressed in these structures [15, 17]. Kim *et al.* [15] reported observing efficiency droop in an InGaN/GaN MQW LED when driven electrically, but not when the QWs were excited directly using a laser with photon energy below the GaN barrier bandgap. With reference to simulated CB and VB profiles, it was concluded that droop must be caused by the leakage of electrons that were not successfully captured by the QWs into the *p*-type GaN cladding layer when a bias was applied. This conclusion was supported by results obtained for LEDs where the GaN QW barriers were replaced with AlGaN with composition chosen such that the net polarisation between the layers was zero; efficiency droop was shown to

be reduced in these LEDs and this was attributed to improved quantum confinement due to the reduced strength of the electric fields across the QWs. Chang *et al.* [17] compared the variation in IQE with current in EL experiments on an $In_{0.21}Ga_{0.79}N$/GaN and an $In_{0.21}Ga_{0.79}N/Al_{0.05}Ga_{0.95}N$ 5 QW LED. The LED with AlGaN barriers reached a higher peak IQE and efficiency droop occurred at higher currents than for the one with GaN barriers. This was partly attributed to the deeper QWs caused by the larger bandgap of the AlGaN barrier material compared to GaN, leading to improved electron confinement and so reducing carrier leakage.

Han *et al.* [18] observed a high energy peak at high injection currents in an InGaN/GaN MQW LED, centred at a wavelength of around 400 nm. The authors attributed this to an optical transition from the conduction band to a Mg acceptor state in the *p*-type GaN layer [54, 55], made possible by the fact that some electrons overflowed from the QWs at the associated carrier densities.

Schulz *et al.* [19] observed a high energy emission band in PL measurements on an InGaN/GaN single QW that decayed on a faster time scale than the rest of the emission. The authors claimed that the QCSE reduces the confinement of electron states with energies above the ground state at low carrier densities, and that the observed PL emission was due to recombination involving electrons in the ground state and holes in the ground and first excited states. At high carrier densities, it was stated that charge carrier-induced screening of the QCSE occurs and that this leads to confinement of electrons in the first excited state. Simulated PL spectra produced based on this model showed a similar HEB to that observed experimentally, and so it was attributed to recombination involving electrons and holes, both in the first excited states. The faster recombination time for this emission feature was said to be due to an increased wavefunction overlap between the electrons and holes in the first excited states relative to those in the ground states.

Nippert *et al.* [20] also reported on the observation of a broad HEB in a variety of single and multiple InGaN/GaN QWs, some of which were grown in LED structures,

under high power pulsed optical excitation. Exponential PL decays were detected across the HEB, with decay times that decreased with increasing detection energy. The authors ascribed the HEB to recombination involving ground state electrons and a continuum of hole states confined by the triangular potential well formed between the bottom QW barrier and the edge of the top QW barrier, illustrated schematically in Figure 6.3. PL spectroscopy was also performed on one of the LED structures under bias. No change in the HEB region of the spectrum was observed relative to when no bias was applied. This was said to be evidence that the carriers involved must still be confined, otherwise they would have been swept out of the active region under the applied bias which would lead to a reduced QW emission intensity.

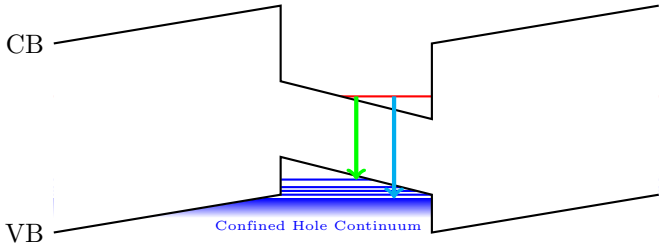

Figure 6.3: Schematic diagram illustrating recombination involving electron and hole ground states (green arrow), and electron ground states and the "confined hole continuum" (cyan arrow), adapted from Nippert *et al.* [20].

In the models for carrier leakage described in this section, InGaN/GaN QWs were treated as simple 1-dimensional potential wells. The experiments reported by Schulz *et al.* [19] were performed at room temperature, where the authors claimed that carrier localisation does not occur. Nippert *et al.* [20] claimed that the energy range over which the HEB was observed would require a large degree of In clustering in the QWs if it were due to carriers in localised states. However, 3-dimensional models of QWs which incorporate localisation effects [56, 57] have shown that they are important both at low temperatures and at room temperature, and that this arises as a result of the random InGaN alloy (that is, with no non-random clustering of In atoms). In this case, the simple 1-dimensional QW cannot be considered as sufficient for describing mechanisms for non-radiative losses at high carrier densities. Several analyses where

carrier localisation has been taken into account when describing a "leakage" of carriers from QWs have therefore been performed and are discussed in Section 6.2.3.

6.2.3 Carrier Delocalisation

Carrier localisation (described in detail in Section 2.5 of Chapter 2) is widely accepted to be the mechanism for the high room temperature IQEs of InGaN/GaN QW structures in spite of the large density of defects present in this group of materials. There have been several reports [21–29] of carriers overcoming this localisation effect at high carrier densities following the saturation of the localised states. This was mentioned in an early study where the efficiency droop was observed in blue and green LEDs by Mukai *et al.* [21]; it was suggested that, at high currents, some carriers overflow from the localised energy states and reach threading dislocations where they recombine non-radiatively. Similar conclusions were reached by Hader *et al.* [22], who derived rate equations for an LED featuring non-radiative recombination at defects as a carrier loss process that became active at high current densities following the saturation of the localising potential minima in the QWs. Several groups [23, 24, 26–29] have attributed observations of fast luminescence decay components or HEBs, or both, to recombination involving weakly localised or delocalised carriers with different dynamics to localised carriers.

Feng *et al.* [23] attributed a PL decay component with lifetime < 200 ps, observed at early times after excitation, to recombination from weakly localised states at 12 K. The authors also performed PL decay measurements at higher temperatures, where they observed that the decay time increased with increasing temperature between 10 K and about 50–60 K for detection energies on the low energy side of the QW spectral peak, and decreased over the same temperature range for detection energies on the high energy side of the spectrum where the fast component was observed. This was attributed to carrier transfer from the weakly localised states to the more

strongly localised states as they gained energy to overcome some potential barrier that prevented this at low temperatures.

Bochkareva *et al.* [24] performed current density dependent experiments on a commercial white LED and reported a direct correlation between the high energy spectral broadening and the efficiency droop of the EL emission at current densities above $10\,\mathrm{A\,cm^{-2}}$. In the model proposed by the authors, the high energy emission was caused by the occupation of higher energy weakly localised states in the band tail following partial filling of the deeply localised tail states at high injected carrier densities. The authors concluded that the increased occupation of the lower energy states leads to a reduced rate of carrier relaxation from the higher energy states, meaning that instead the higher energy carriers are thermally excited above the mobility edge where they are delocalised and therefore more likely to recombine non-radiatively at defects.

Hammersley *et al.* [25] performed temperature dependent PL spectroscopy on a 5-period InGaN/GaN QW structure at two excitation power densities: one where the structure was not observed to undergo efficiency droop, and a much higher power density where the IQE had fallen to 20 % of its peak value. The authors observed that the depth of the S-shape temperature dependence minimum (most commonly attributed to the thermally activated redistribution of carriers among localised states in the QW [58–60]) was dramatically decreased at the higher excitation power density. The authors suggested that this was due to a saturation of localised states preventing the redistribution of carriers to these states as the temperature was increased from 10 K to around 100 K.

Davies *et al.* [26] reported on the observation of a high energy spectral broadening in high excitation power density TIPL measurements performed on an InGaN/GaN single QW structure at 10 K. TRPL measurements revealed that this broadening was caused by a weak PL emission feature which decayed exponentially with a lifetime of 1.9 ns on the high energy side of the QW spectral peak. This was very different in nature to the non-exponential decays observed across the QW peak, with much slower

lifetimes (∼10–100 ns), which were attributed to recombination involving separately localised electrons and holes. For this reason, it was concluded that the fast decay component must have a fundamentally different origin. With reference to the works by Bochkareva *et al.* [24] and Hammersley *et al.* [25], it was attributed to recombination involving carriers in weakly localised or delocalised energy states following the saturation of the strongly localised states.

A distinct HEB was observed in the PL spectrum for an InGaN/GaN MQW structure by Sun *et al.* [27], who performed time-resolved pump-probe spectroscopy to determine a decay time constant for this band of 1.41 ns at 5 K. This was much faster than the main QW emission decay, which exhibited a lifetime of 570 ns. The authors concluded that the main QW peak was due to recombination from localised electrons and holes, while the high energy band was attributed to recombination from "extended" states. The decay time of the HEB was observed to vary much less with temperature than that of the localised states emission peak, and so it was suggested that the "extended" states were less susceptible to non-radiative recombination.

More recently, Nomeika *et al.* [28] performed pump-probe measurements on cyan and green emitting QW samples to demonstrate a reduction in the absorption on the high energy side of the spectrum at high excitation powers, an effect that the authors ascribed to the filling of states. A high energy broadening of the QW PL spectrum at high excitation power densities, accompanied by a faster PL decay rate, was concluded to be due to recombination from delocalised holes following the saturation of the lower energy localised hole states. The authors noted the compatibility of their work with the conclusions of Feng *et al.* [23] and Bochkareva *et al.* [24], as well as the model for hole localisation developed by Schulz *et al.* [61] that is discussed in detail in Chapter 2.

In work by Dunn *et al.* [29], a 10-period $In_{0.18}Ga_{0.82}N$/GaN QW structure was optically excited at room temperature at a power density where the IQE was observed to droop to 3 % of its maximum value. Under these excitation conditions, the

spectrally-integrated TRPL intensity featured a fast component, which decayed to $1/e$ of its maximum intensity in 19.6 ps, and a slow component with a $1/e$ decay time of 5.8 ns. The slow component was also observed in TRPL measurements performed at much lower excitation power densities, below the efficiency droop regime for this structure, and was attributed to recombination involving localised electron and hole states. The intensity of the slow component was observed not to increase with excitation power density beyond the peak efficiency of the structure, leading the authors to conclude that this component was saturated in the efficiency droop regime. The time-resolved transmission of terahertz radiation through the sample was then measured under the same two excitation conditions. The terahertz transmission was observed to increase over time giving similar fast and slow components in the time-resolved transmission spectra as were observed in the TRPL spectra. The slow component was observed to increase in intensity at the higher excitation power density, and the fast component was much less pronounced than in the PL measurements. The reduction in terahertz transmission of a sample under optical excitation is proportional to the density of photoexcited carriers in that sample. The authors predicted that the much larger effective mass of holes compared to electrons in InGaN QWs meant that this reduction in transmission would be governed by the excited electron population rather than that of the holes. It was therefore concluded that the saturation of the slow PL component was due to the saturation of localised hole states, and that since the terahertz transmission experiment was not sensitive to the excited holes, the slow component observed in the time-resolved transmission data would not saturate at high excitation carrier densities.

Studies of the spectral dependence of the HEB decay dynamics have been very limited. In the work of Davies *et al.* [26], PL decays detected at only one energy were discussed. In most of the other works summarised in this section, decay curves and lifetimes were produced by integrating over the full energy range of the time-resolved spectra in which the HEB was observed [14, 23, 27–29]. Feng *et al.* [23] presented

PL decays detected at different energies across the high energy side of the emission, but the authors did not observe a distinct band that was separated in energy from the low power QW emission. Rather, only a high energy broadening was seen which prevented any definitive analysis of the form of the associated decays due to the spectral overlap of the fast and slow decaying features. Nippert *et al.* [20] reported exponential decays with decreasing lifetime as the detection energy across the HEB was increased, but no examples of the form of the decays were given. In the work presented in this chapter, PL spectra from single InGaN/GaN QWs are shown to feature a very broad HEB at high excited carrier densities which extends far beyond the low carrier density QW emission region. This enables the spectral dependence of the PL decays across this band to be studied. The overall shape of these decays is unlike any previously presented in studies of similar HEBs, and it is compared to the shape of decays observed in PL studies of semiconductor QDs.

6.3 Sample Details

Three single InGaN/GaN QW samples with different QW In fractions were investigated in this work. The samples were grown by MOVPE by the 1T growth method with nominally identical QW widths. Once grown, the In fractions and QW widths were determined by electron energy-loss spectroscopy and high-resolution TEM, respectively. The details of the three samples relevant to this work are presented in Table 6.1. Further details on the growth and characterisation of these samples are available in the work of Graham *et al.* [62]. All growth and structural characterisation was performed by colleagues at the Department of Materials Science and Metallurgy, University of Cambridge.

Table 6.1: Summary of the QW In fractions and widths for the three single QW samples investigated in this work.

Sample Number	Growth Temperature (°C)	QW In Fraction (%)	QW Width (nm)
C187	750	15	2.9
C189	730	19	3.2
C191	710	25	3.3

Single QWs were chosen for this work as they tend to produce narrower PL spectra than MQWs, where spectral broadening is caused by variations in alloy composition and well width between the different QWs [62]. This ensured the best possible spectral resolution to enable detailed study of the decay dynamics at all energies.

6.4 Results and Discussion

6.4.1 Time-Integrated Photoluminescence Spectroscopy

Low temperature (10 K) PL TIPL spectra were obtained using the pulsed frequency-tripled Ti:sapphire laser as the excitation source with a final photon energy of 4.661 eV. These are shown normalised to their peak intensities in Figure 6.4 for a peak excited sheet carrier density of $\sim 10^{11}\,\mathrm{cm}^{-2}\,\mathrm{pulse}^{-1}$. Carrier densities were estimated by assuming that each photon incident on the sample generates one electron-hole pair which are both subsequently captured by the QW. The peak emission energies of the QW zero-phonon peaks, which are assigned to recombination involving separately localised electrons and holes [62], were determined for each sample from the spectra and are given in Table 6.2. The lowest energy electron and hole states involved in the recombination at this carrier density and at low temperatures are referred to as the electron and hole ground states in this chapter.

The QW peak emission energy decreases with increasing In fraction due to the decreasing bandgap energy of the QW. The first, second and, in the case of the 19 %

and 25 % In samples, third LO phonon replica peaks are clearly visible. The peak energies of these, referred to as LO1, LO2 and LO3, respectively, are given in Table 6.2. The LO phonon replica peaks for a particular QW are separated in energy by (91 ± 2) meV.

Table 6.2: Summary of the zero-phonon and first, second and third LO phonon peak energies for the three single QW samples at 10 K. The third LO phonon peak was not measurable for the 15 % In sample.

QW In Fraction (%)	Zero-Phonon Peak (eV)	LO1 (eV)	LO2 (eV)	LO3 (eV)
15	2.651 ± 0.001	2.556 ± 0.001	2.468 ± 0.001	-
19	2.309 ± 0.001	2.218 ± 0.001	2.126 ± 0.001	2.037 ± 0.001
25	2.143 ± 0.001	2.053 ± 0.001	1.960 ± 0.001	1.870 ± 0.001

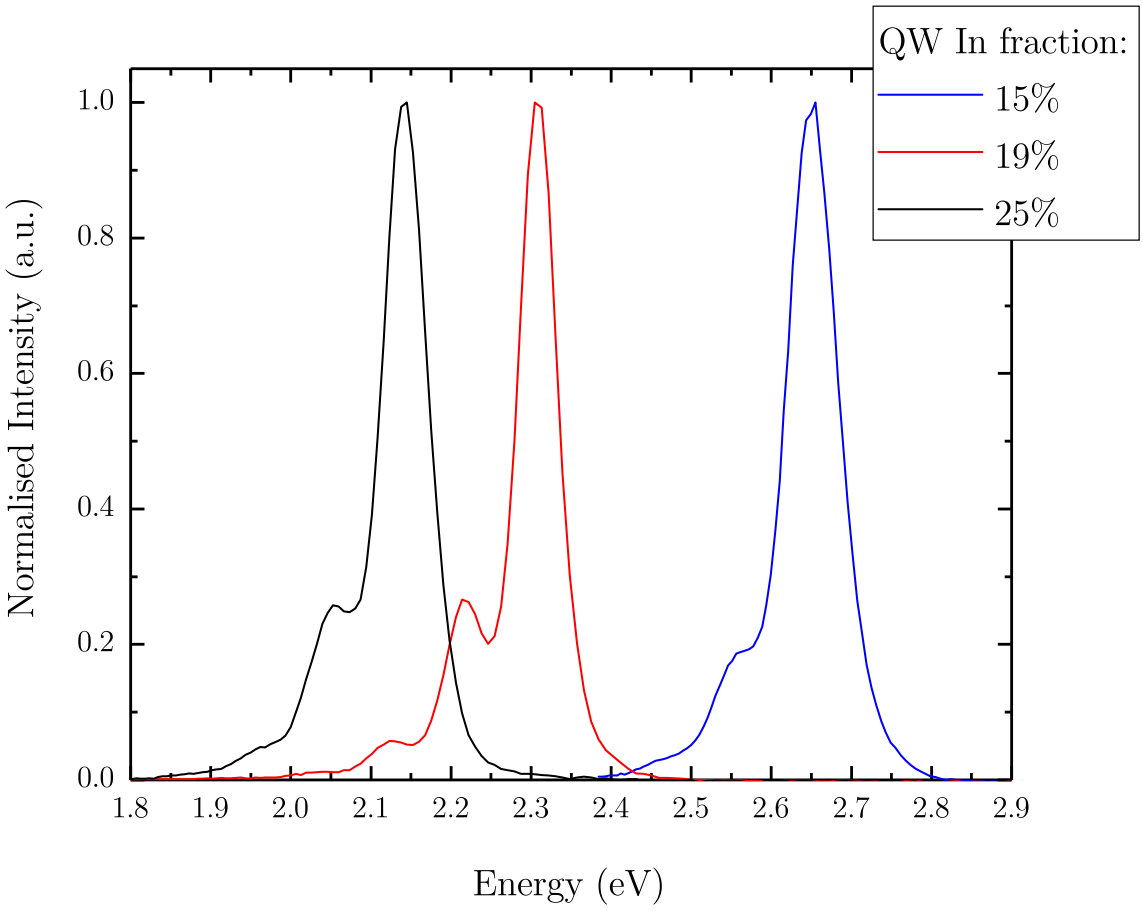

Figure 6.4: Normalised TIPL spectra for the three single QW samples measured at 10 K and low ($\sim 10^{11}$ cm^{-2} pulse^{-1}) excited carrier density.

Excitation power dependent TIPL spectroscopy was performed on each of the samples at 10 K and spectra are shown for the 25 % In sample in Figure 6.5 at various peak excited carrier densities. Power dependent TIPL spectra for the 19 and 25 % In samples are shown in Appendix A. For carrier densities of $\sim 10^{12}\,\mathrm{cm}^{-2}\,\mathrm{pulse}^{-1}$ and above, an additional emission band is present on the high energy side of the QW ground state emission feature. The FWHM of this HEB increases as the excited carrier density is increased, as does its peak intensity relative to that of the ground state emission peak. Attempts to eliminate the Fabry-Pérot interference fringes that are visible across the HEB were unsuccessful.

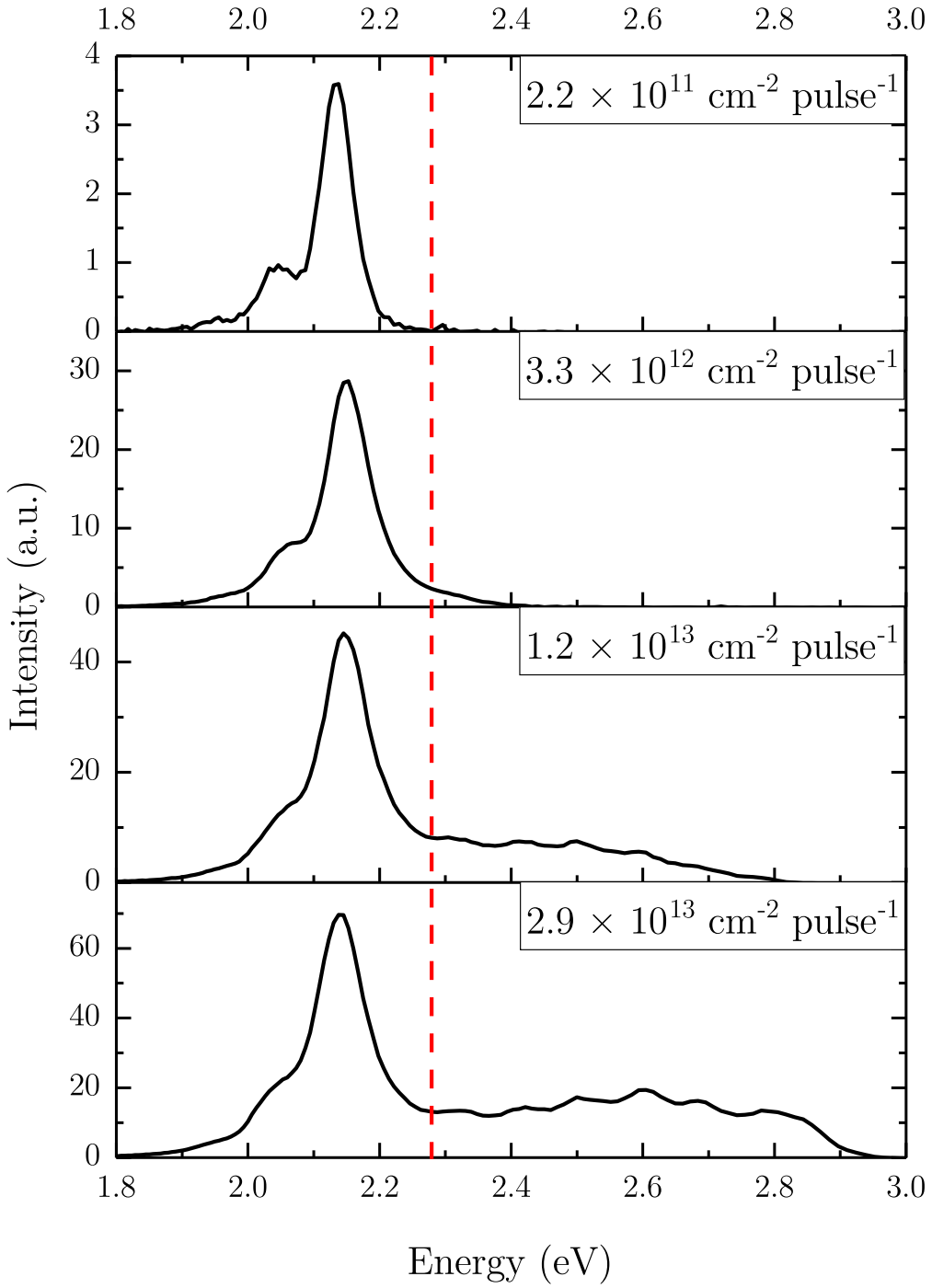

Figure 6.5: TIPL spectra for the 25 % In sample, measured at 10 K, at various peak carrier densities. The red dashed line marks the point in the spectrum where the QW ground state emission and the HEB have been separated for the purposes of comparing the integrated intensities of the two features.

The FWHM of the HEB is at least around 540 meV at the highest peak excited

carrier density that was achieved for the 25 % In QW sample. This is in contrast to the QW ground state peak, which has a FWHM of 60 meV at a peak carrier density of $2.2 \times 10^{11}\,\mathrm{cm}^{-2}\,\mathrm{pulse}^{-1}$. The low energy limit of the HEB is difficult to discern due to the overlap with the QW ground state emission peak, so the true FWHM of the HEB may be larger.

Many broad luminescence bands have been identified in bulk GaN and attributed to various defects and impurities in the material [63]. The assignment of the HEB to one of these bands can be ruled out since its peak emission energy and FWHM varies with excited carrier density, and with QW In composition for a given excited carrier density. It also occurs exclusively on the high energy side of the QW ground state emission in all of the samples. These points are illustrated in Figure 6.6, which shows normalised TIPL spectra for all three single QW samples at a peak excited carrier density of $2.5 \times 10^{13}\,\mathrm{cm}^{-2}\,\mathrm{pulse}^{-1}$. This confirms that the HEB must be related in some way to the recombination of carriers in the QW and is not due to an entirely separate recombination process in the bulk GaN.

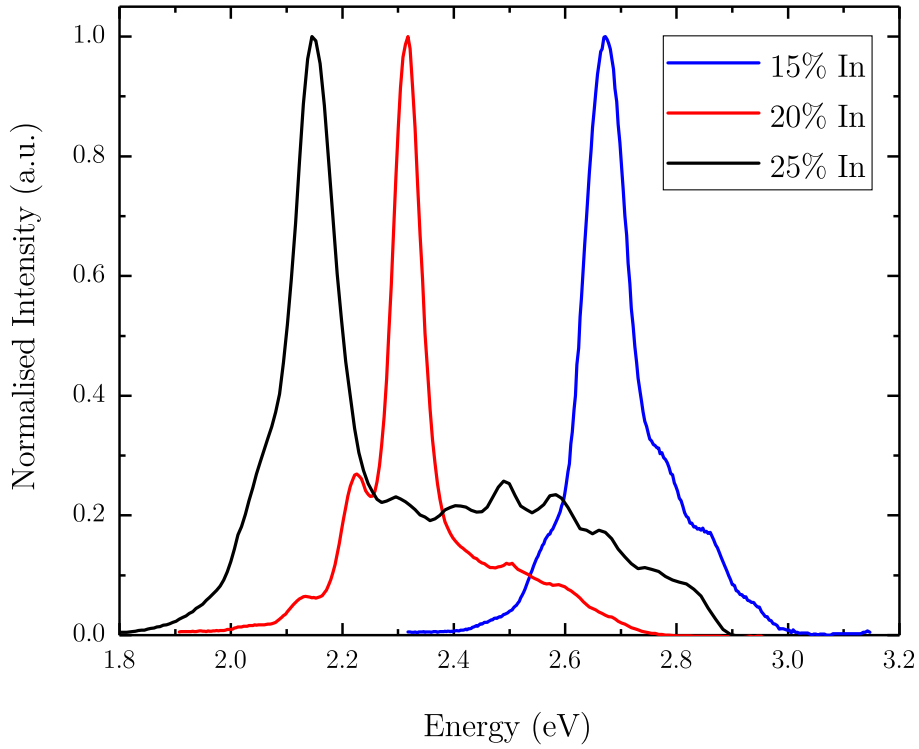

Figure 6.6: TIPL spectra, normalised to the QW ground state emission peak intensity, for the three single QW samples with different In compositions at a peak carrier density of $2.5 \times 10^{13}\,\mathrm{cm}^{-2}$.

The integrated intensities of the QW ground state emission and the HEB, as well as that of the total spectrum, per unit *total* peak carrier density are shown as a function of *total* peak carrier density for the 25 % In QW sample in Figure 6.7. The *total* carrier density is used here because the relative densities of carriers involved in the two emission bands is unknown. The integrated intensities were determined for the two features by cutting the spectrum at 2.279 eV on the energy axis, marked by the red dashed line in Figure 6.5, and integrating over energies below (ground state) and above (HEB) this value, respectively. Figure 6.7 shows that the integrated intensity per unit excited carrier density of the QW ground state emission peak reaches a peak value and begins to decrease as the total peak carrier density is raised above $\sim 10^{12}\,\mathrm{cm}^{-2}\,\mathrm{pulse}^{-1}$. This coincides with the onset of the HEB, for which the integrated intensity increases super-linearly with increasing total peak carrier density.

However, the radiative recombination pathway that causes the HEB cannot account fully for the decrease in the QW ground state emission intensity per unit carrier density as the total spectrally integrated intensity per unit excited carrier density is also decreasing over this excitation density range.

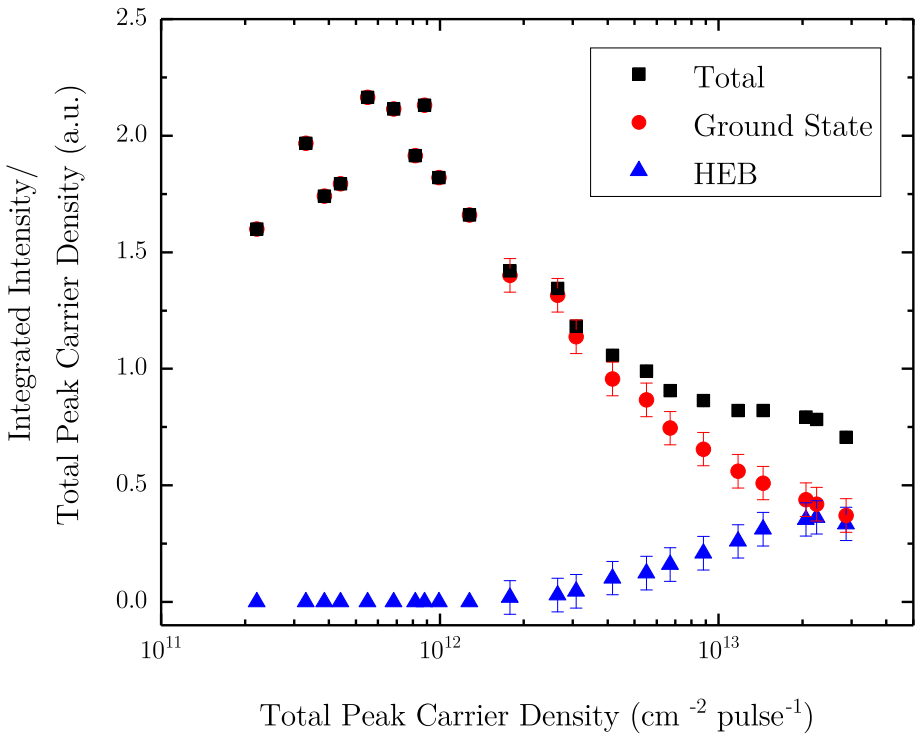

Figure 6.7: Integrated intensity per unit total peak carrier density varying with total peak carrier density for the ground state, HEB and total PL emission from the 25 % In QW sample.

6.4.2 Time-Resolved Photoluminescence Spectroscopy

TRPL spectra were measured at a peak total carrier density at time, $t = 0$, of $3.1 \times 10^{13}\,\mathrm{cm}^{-2}$, and are shown for the 25 % In sample in Figure 6.8. Each spectrum is integrated over the time range as shown on the figure. For the earliest detection time window (0–0.3 ns), the PL FWHM is 282 meV with a peak at around 2.65–2.66 eV (Fabry-Pérot interference prevents precise determination of the peak energy). This emission reduces on the high energy side with increasing time.

The same TRPL spectra are shown together on a logarithmic intensity scale in

Figure 6.9. This shows more clearly that, at early detection times, the PL emission energy extends across the region associated with the QW ground state peak (and LO phonon replicas) as well as the HEB.

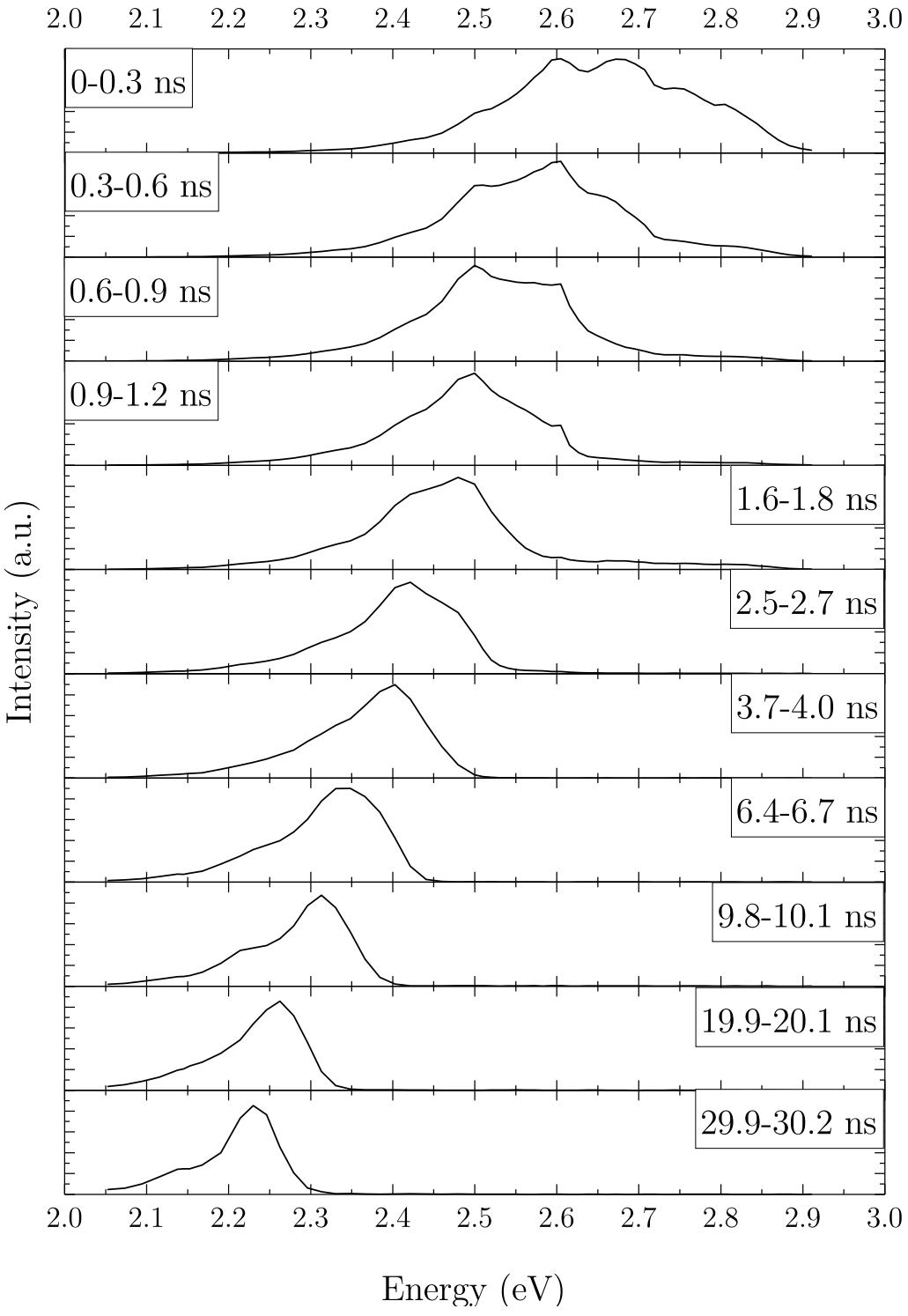

Figure 6.8: TRPL spectra for the 25 % In QW sample for a peak excited carrier density of $3.1 \times 10^{13}\,\mathrm{cm}^{-2}\,\mathrm{pulse}^{-1}$.

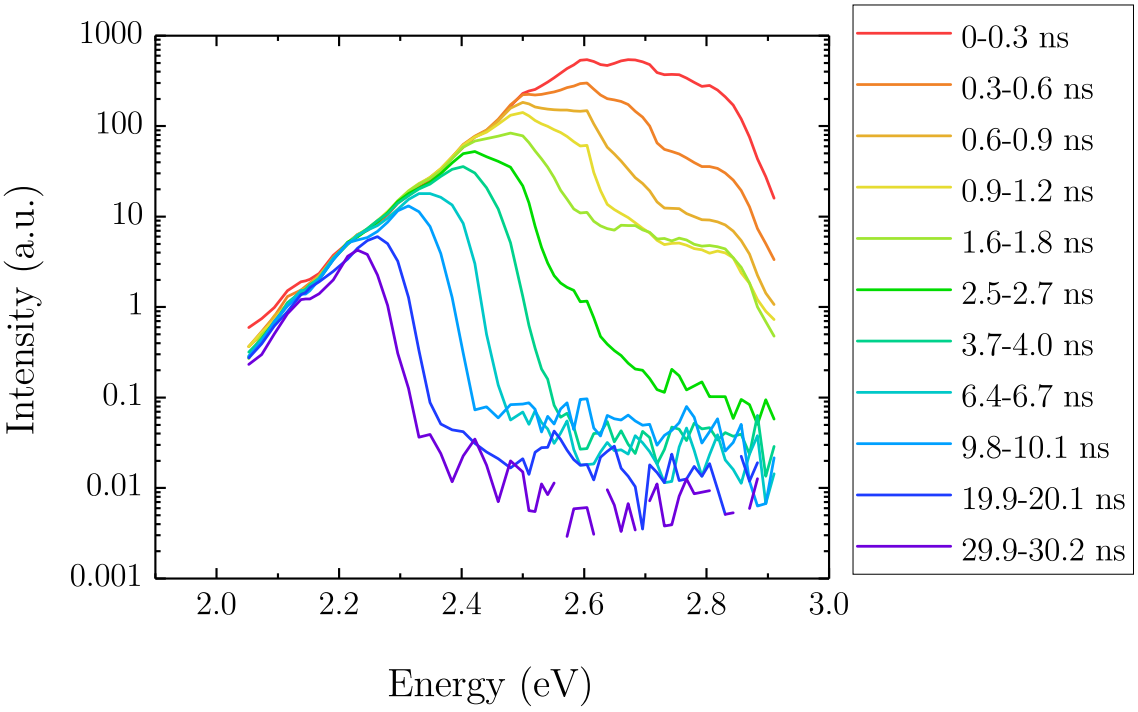

Figure 6.9: TRPL spectra from Figure 6.8 for the 25 % In QW sample plotted together on a logarithmic intensity scale.

The TRPL spectra indicate that the HEB that was observed in the TIPL experiments is actually a broad, fast-decaying emission feature which dominates the spectrum at early detection windows. The shape of the spectrum detected for the 29.9–30.2 ns time window resembles that of the QW ground state TIPL spectrum, but the peak energy of this TRPL spectrum is 88 meV higher in energy than that of the TIPL spectrum. The continued temporal evolution of the spectrum was investigated by repeating the TRPL experiment with a peak excited carrier density at $t = 0$ of $2.9 \times 10^{12}\,\mathrm{cm}^{-2}$. These conditions are just inside the efficiency droop regime but with little to no detectable presence of the HEB in TIPL measurements. TRPL spectra from this experiment are shown at 100 ns intervals averaged over 3 ns time windows in Figure 6.10. The QW ground state emission peak red shifts by (50 ± 1) meV between the 0–3 ns and 500–503 ns detection windows. It has been reported that the PL spectrum of InGaN/GaN QWs can blue shift with increasing excited carrier density due to the charge-carrier induced screening of the QCSE [64–

66]. However, the blue shift observed for the QW ground state peak in the TIPL in Section 6.4.1 is only 6 meV as the peak excited carrier density increases over the range 2.2×10^{11}–$2.9 \times 10^{13}\,\mathrm{cm}^{-2}\,\mathrm{pulse}^{-1}$. The peak of the spectrum occurs at higher energies for intermediate peak carrier densities, but this is likely to be artificial and due to the overlapping HEB spectrum as the effect is reversed once the HEB spectral peak becomes resolvable from the ground state emission. It is possible that the blue shift due to the screening of the field was not observed in the TIPL measurements because the majority of the screened emission only persists for a short time, with the emission between laser pulses being dominated by the lower energy, unscreened emission. However, the Huang-Rhys factor (that is, the ratio between subsequent LO phonon replica peak intensities) remains constant at 0.24 ± 0.01 over the time range. If the QCSE were screened, the subsequent increased overlap of the electron and hole wavefunctions should lead to a reduced Huang-Rhys factor [62] at early times, and it should increase with increasing time. This is therefore further evidence that this red shift with increasing time is not due to the gradually returning QCSE.

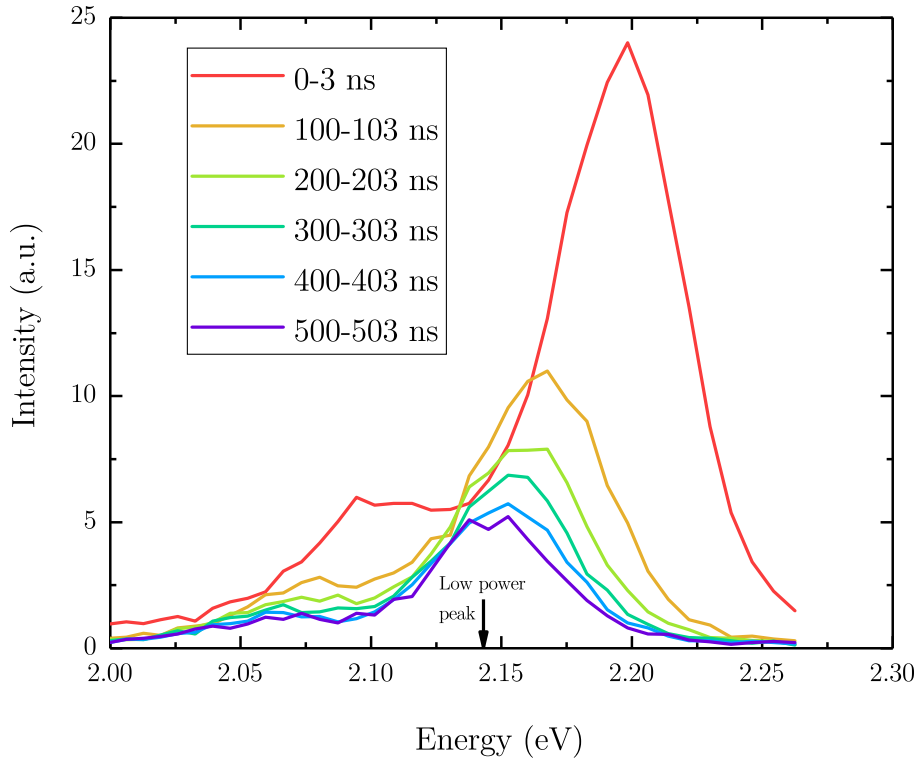

Figure 6.10: TRPL spectra for the 25 % In QW sample for a peak excited carrier density of $2.9 \times 10^{12}\,\mathrm{cm}^{-2}\,\mathrm{pulse}^{-1}$. The low power zero-phonon TIPL peak energy is indicated by the arrow.

To investigate the dynamics of the HEB further, PL time decay measurements were performed at detection energies across the emission spectrum under a similar excited carrier density as for the first set of TRPL measurements. These are shown in Figure 6.11. The inset shows a TIPL spectrum with arrows marking the detection energies of the correspondingly coloured PL decays. The peaks at 1.7 ns on the decays detected at 2.883, 2.725 and 2.583 eV are due to the instrumental response. The final parts of all of the PL decays detected across the HEB, away from the QW ground state emission, are exponential. However these parts of the decay are preceded by plateaus, the durations of which increase as the detection energy across the HEB is decreased. The PL decay detected at 2.234 eV is shown in full in Figure 6.12. It features a 5 ns plateau, followed by an exponential drop in intensity to 63 % of its peak value. The final part of this decay is non-exponential and resembles decays at low excited carrier

densities that are attributed to recombination from separately localised electron and hole ground states. The complex shape of this PL decay may be due to spectral overlap between the QW ground state emission peak and the HEB at this detection energy, where the decay is dominated at early times by features associated with the HEB (plateau followed by exponential decay) and then by the non-exponential decay associated with the ground state emission at later times.

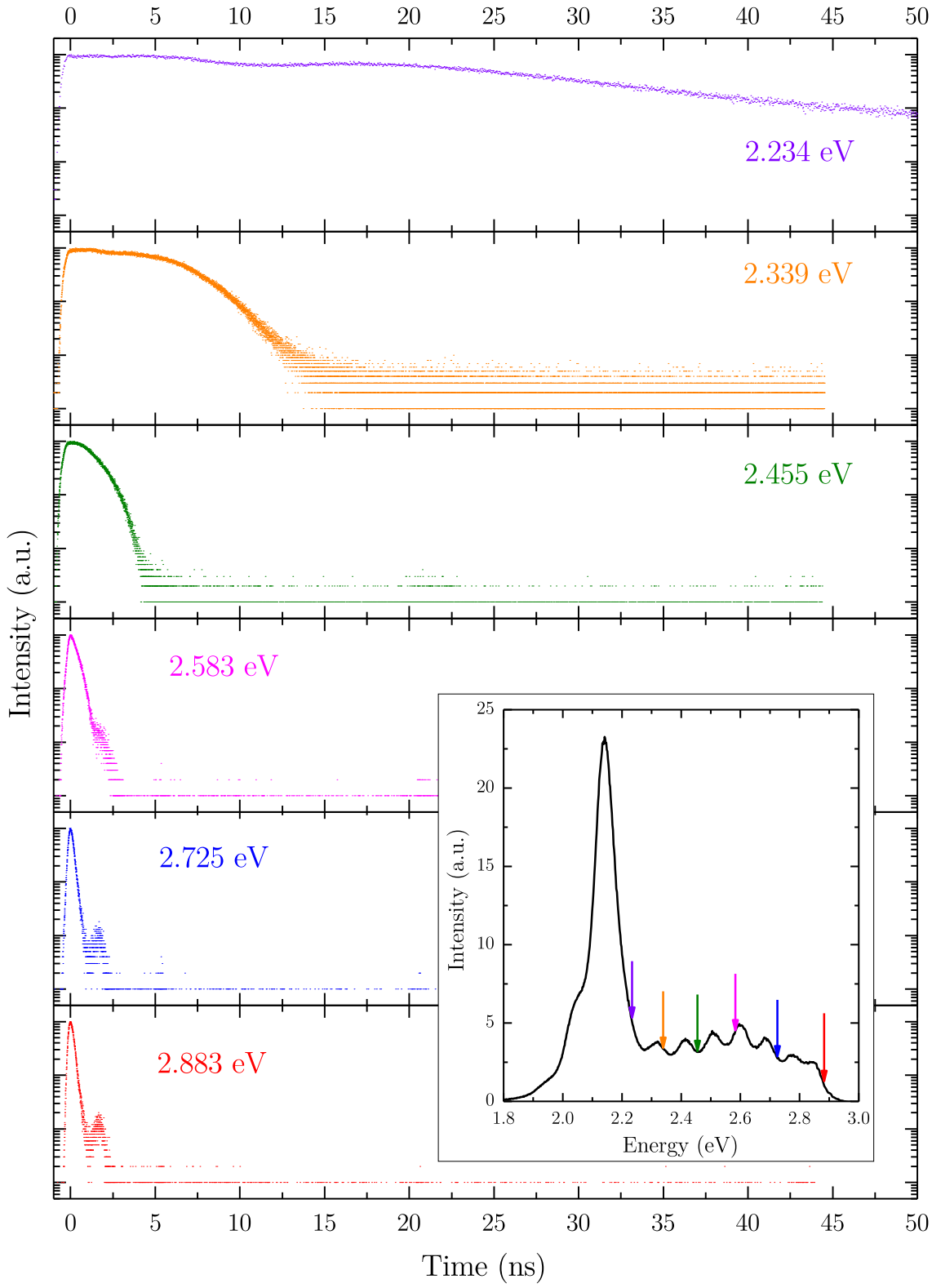

Figure 6.11: PL time decays detected across the HEB for the 25 % In QW sample for a peak excited carrier density of $\sim 10^{13}\,\mathrm{cm}^{-2}\,\mathrm{pulse}^{-1}$. Inset: TIPL spectrum marked with arrows corresponding to the coloured PL time decays.

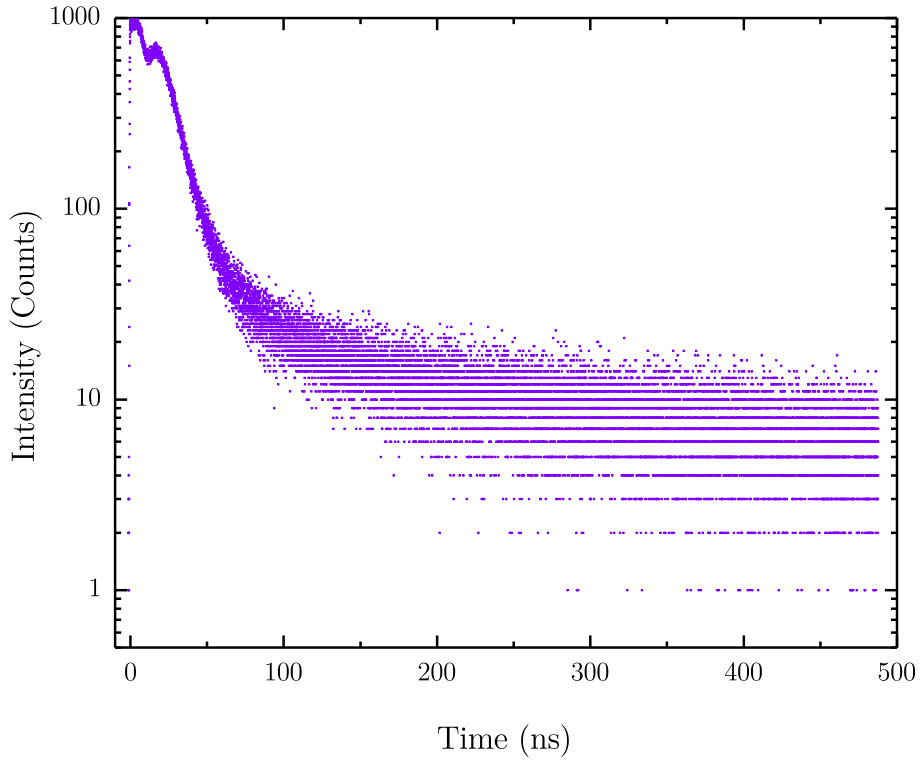

Figure 6.12: PL time decay for the 25 % In QW sample, detected at 2.234 eV for a peak excited carrier density of $2.9 \times 10^{13}\,\mathrm{cm}^{-2}\,\mathrm{pulse}^{-1}$.

Single exponential functions were fitted to the exponential parts of the PL decays across the HEB to extract their characteristic lifetimes. These lifetimes are shown to decrease with increasing detection energy in Figure 6.13.

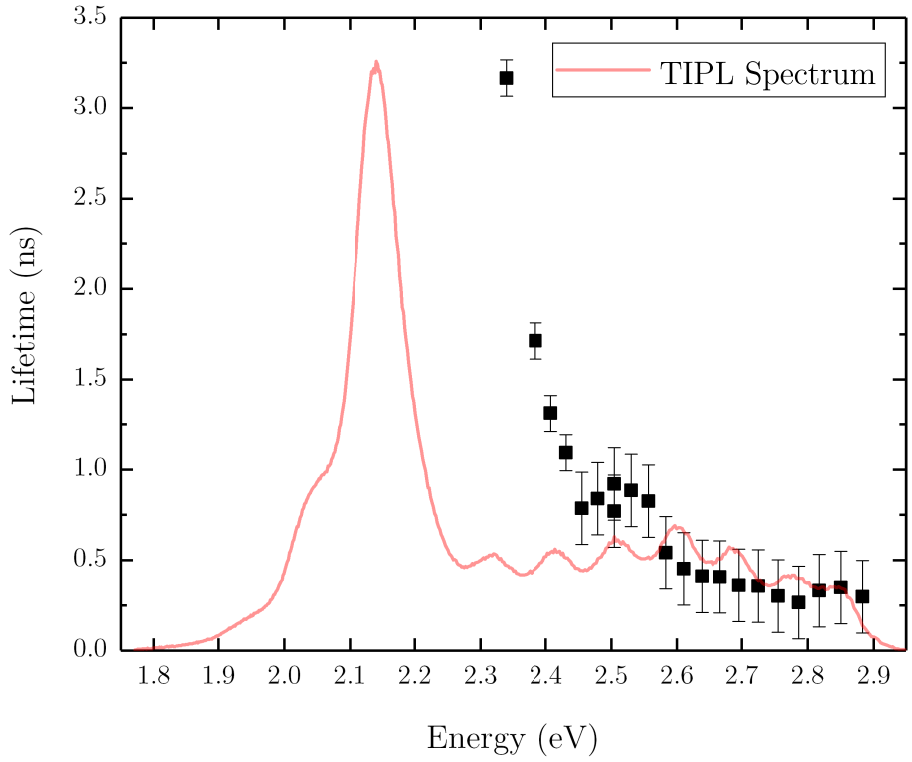

Figure 6.13: Lifetimes of the exponential parts of the PL decays varying with detection energy across the HEB for the 25 % In QW sample. A TIPL spectrum recorded at the same excited carrier density as the PL time decays is shown for reference.

Both the TRPL and PL time decay results show that the HEB decays sequentially from the highest energies to the lowest. The PL intensity at a given detection energy remains essentially constant with time until the PL at a higher detection energy has begun to decay. This is similar to PL decays reported for In(Ga)As/GaAs self-assembled QDs [67–71]. In these works, additional peaks were observed to occur on the high energy side of the QD ground state PL emission peak with increasing excitation photon densities. These peaks were identified as being due to excited electron states of the QDs, occupied following saturation of the lower energy electron states due to Pauli state blocking. Buckle *et al.* [67] and Grosse *et al.* [68] reported PL time decays detected at these emission peaks which exhibited plateaus before the decays for high excited carrier densities. These plateaus were attributed to the refilling of the lower energy states by carriers which scatter down from the higher energy states.

The durations of the plateaus were shown to decrease with increasing excited state energy, which is very similar behaviour to that observed in the HEB associated with the InGaN QWs.

PL time decay measurements were performed on the 25 % In QW sample for a range of excited carrier densities per laser pulse. These are shown in Figure 6.14 alongside normalised TIPL spectra on which the detection energies are indicated by coloured arrows. The duration of the plateau region of the decay increases with increasing excited carrier density for a given detection energy in the region of the HEB, while the exponential part maintains a fixed lifetime. This was also observed in the QDs studied by Grosse *et al.* [68], and it suggests that the lifetime of the exponential decay at a given detection energy is characteristic of the recombination involving carriers in the state(s) corresponding to that energy.

A simple model to describe this QD-like behaviour is illustrated schematically in Figure 6.15, in which a carrier in a particular energy state, E_i, will either scatter to a lower energy state, E_j, with associated characteristic scattering lifetime, τ_{ij}, or exit the system via some recombination process with characteristic lifetime, $\tau_{\mathrm{R}i}$. If the carrier scatters to state E_j, then either a recombination process with characteristic lifetime, $\tau_{\mathrm{R}j}$, or scattering to a third lower energy state with scattering time, τ_{jk}, will occur. If the carrier is in the ground state, E_0, then recombination is the only possible event.

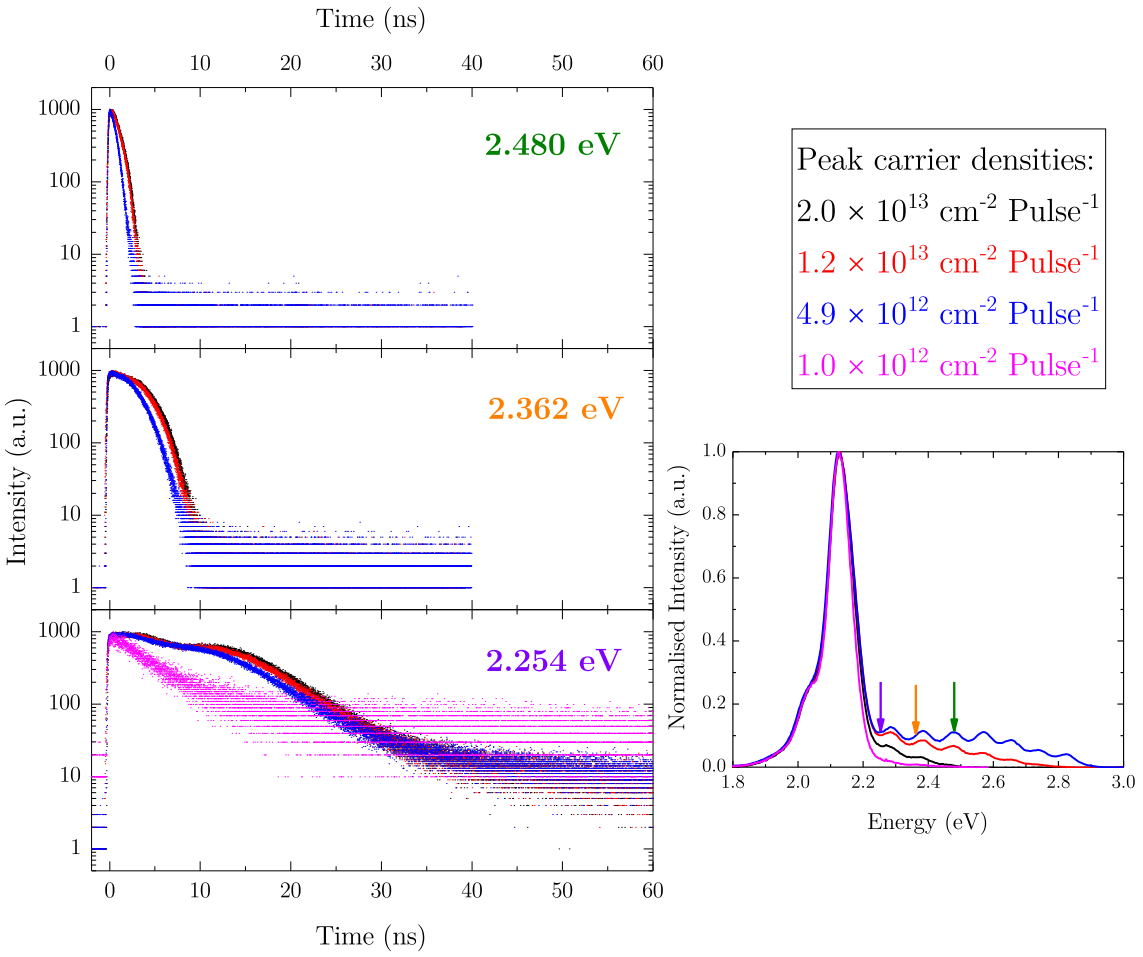

Figure 6.14: Left: Power dependent PL time decays at different detection energies. Right: TIPL spectra corresponding to the different peak carrier densities used in the time decay measurements. The arrows correspond to the different detection energies for the time decays.

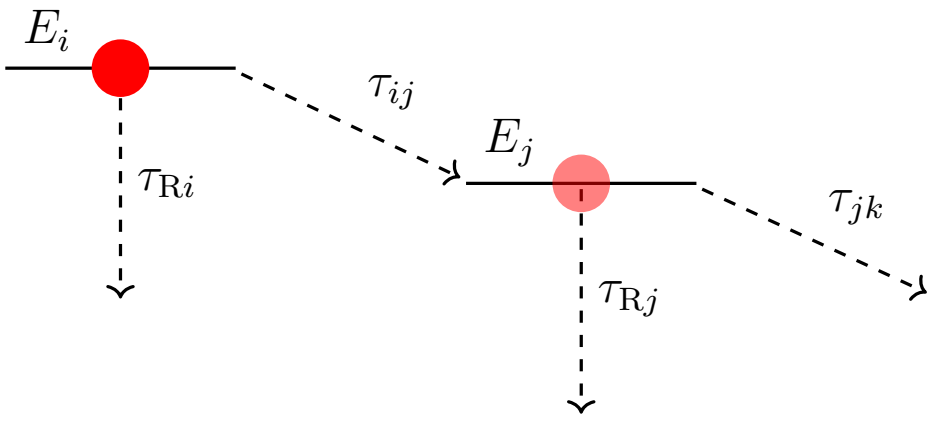

Figure 6.15: Schematic diagram of a simple model describing carriers (red circles) which can either scatter down from higher to lower energy states, or recombine.

A Monte Carlo simulation was applied to the model described above and illustrated in Figure 6.15. The probability of a carrier scattering from E_i to E_j, P_{ij}, is given by

$$P_{ij} = \begin{cases} \dfrac{N_i(t)\,\mathrm{d}t}{\tau_{ij}} & \text{for} \quad 0 < i < j \quad \text{and} \quad N_j(t) < N_{\max} \\ 0 & \text{otherwise} \end{cases} \tag{6.8}$$

where $N_i(t)$ is the number of carriers in state E_i, $\mathrm{d}t$ is the time step used for the simulation and $N_{\max}$ is the occupation limit of any state. The characteristic scattering lifetime was set to $\tau_{ij} = 100\,\mathrm{ps}$. The probability of a carrier in state E_i exiting the system via some recombination process, $P_{\mathrm{R}i}$, is given by

$$P_{\mathrm{R}i} = \frac{N_i(t)\,\mathrm{d}t}{\tau_{\mathrm{R}i}} \tag{6.9}$$

where the characteristic recombination lifetimes were set at $\tau_{\mathrm{R}i} = 0.5\,\mathrm{ns}$ for $i > 0$ and $\tau_{\mathrm{R}0} = 10\,\mathrm{ns}$.

The recombination lifetimes were chosen to be of the same order of magnitude as those observed in the PL time decay experiments. For simplicity, the same lifetime was used for all the energy states above the ground state since the experimental variation between these is small compared with the difference in lifetime for the ground state. The scattering lifetime was chosen to be of a similar order of magnitude to those reported in the works on QDs [67, 68]. The conditions specified in Equation 6.8 mean that carrier transfer to higher energy states was forbidden, as was scattering to a state that is full. The occupation limit was set to $N_{\max} = 10\,000$ for all states. States were filled sequentially from E_0, where the next lowest state would begin to be filled once the previous one reached its maximum capacity. The simulated variations in the populations of 5 energy states (4 excited states and the ground state) with time, t, are shown in figure 6.16. All states are full at $t = 0$ from a total of 50 000 initial carriers, and $\mathrm{d}t = 0.1\,\mathrm{ps}$.

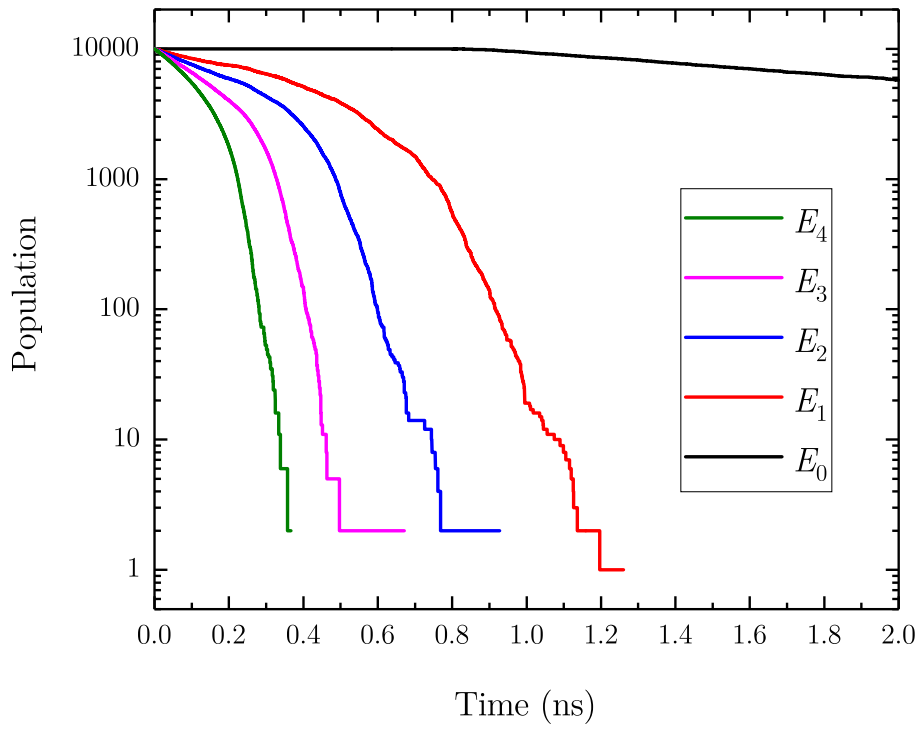

Figure 6.16: Monte Carlo simulation results for population decays for the ground state, E_0, and 4 excited states, E_{1-4}.

The simulated results in Figure 6.16 are analogous to PL decay curves, and show qualitatively similar behaviour to those in Figure 6.11, where the highest energy state populations decay first, with carrier scattering processes leading to refilling of the lower energy states and so delaying the lower energy decays resulting in plateaus. While this model does not describe fully the experimental results reported in this work, it does provide a simple illustration of the type of process that could lead to PL decays of this shape.

A major difference between the HEB observed here and the high energy peaks reported for the QDs is that it is a continuous emission band rather than a series of discrete peaks. The InGaN/GaN QW ground state emission originates from many localised states with small energy separations. This leads to the much broader ground state emission compared to the In(Ga)As/GaAs QDs, and the HEB may comprise emission from higher order states corresponding to each of these ground states. This could also explain the fact that the HEB overlaps with the QW ground state emission

peak; the emission at energies in this region appears to consist of a component that is due to recombination from QW ground states and a component from higher order states corresponding to ground states at lower energies than the detection energy.

The fastest PL decays on the HEB would be detected at the high energy extreme of the band, but here the emission is very weak. This may be why the simulated decays for the simple five state system described above are on much shorter total time scales than those observed experimentally.

The PL decays detected at 2.254 eV include one for a peak carrier density at which the HEB was not measurable (and therefore decays were not measured at higher energies for this peak carrier density). At peak carrier densities of 4.9×10^{12}, 1.2×10^{13} and $2.0 \times 10^{13}\,\mathrm{cm^{-2}\,pulse^{-1}}$, the PL decays feature a plateau, followed by an exponential decay and then a non-exponential decay, similarly to the decay shown in Figure 6.12. As with the decays detected at 2.362 and 2.480 eV, the duration of the plateau region increases with increasing peak carrier density and the lifetime of the exponential part of the decay remains fixed. The increasing duration of the plateau causes the entire PL decay to be delayed until increasingly later times. The PL decay produced for a peak excited carrier density of $1.0 \times 10^{12}\,\mathrm{cm^{-2}\,pulse^{-1}}$ exhibits no plateau or exponential parts. Instead, only a non-exponential decay similar to the final part of the decays at higher peak carrier densities is observed. Since this occurs under conditions where the HEB is not present, it provides further evidence that the decays detected in this region of the spectrum at high peak carrier densities contain components due to the separate but overlapping QW ground state and HEB emission features.

In the 3-dimensional atomistic model for InGaN/GaN QWs employed by Tanner *et al.* [56], discussed in Section 2.5 of Chapter 2, the spatial extents of electron and hole wavefunctions localised by random alloy fluctuations and QWWFs were calculated along with their overlaps with other states in the system. It was shown that, for a 10 % In QW, hole states with energies up to ∼100 meV have small wavefunction overlaps

with other energy states. These states were considered to be strongly localised and the energy range of the localised states was reported to increase with increasing In fraction. A higher energy regime was also identified in which the hole wavefunctions have large overlaps with other states; these states were described as weakly localised or delocalised. At low electron and hole state energies, the electron-hole wavefunction overlap was calculated to be very small for a 25 % In QW. However, the higher energy (less localised) hole states have larger wavefunction overlaps with all electron energy states and the wavefunction overlap increases with increasing hole state energy. The electron-hole recombination rate is proportional to the wavefunction overlap, so this agrees with the experimental observation that the ground state PL decay is much slower than the decays measured across the HEB, where the HEB emission can be attributed to recombination of electrons and the higher energy, weakly localised or delocalised hole states. Other groups have similarly assigned the HEB to less localised states [23, 24, 26, 27, 29], but without reference to a complete atomistic model for localisation.

The exponential PL decays detected across the HEB must be due to a fundamentally different recombination process to that which causes the non-exponential QW ground state PL decays. While the QW ground state recombination process at low temperature has been shown to be dominated by radiative recombination between separately localised electrons and holes, the nature of the recombination process that gives rise to the HEB has not been established. None of the PL decays exhibit a cubic dependence on carrier density, as could be expected if Auger recombination were the dominant mechanism [72]. If the HEB is caused by the recombination of delocalised electrons *and* holes, then it may be reasonable to assume that these form excitons as the reason that this does not happen at low carrier densities is because of the separate localisation of electrons and holes. The exponential decays detected across the HEB may be evidence of excitonic recombination. However, according to the model of Tanner *et al.* [56], a hole in a delocalised energy state can recombine with an electron in any

energy state. This would result in a non-exponential decay due to the wide variation in electron and hole wavefunction overlaps. As shown above in Figure 6.7, the combined PL emission from the QW ground state and the HEB exhibits the efficiency droop with increasing excited carrier density. This necessarily means that a non-radiative recombination process is active at carrier densities above $\sim 10^{12}\,\mathrm{cm}^{-2}\,\mathrm{pulse}^{-1}$. Since the occurrence of the HEB coincides with the onset of droop, it may be that the dominant associated recombination process is non-radiative. If the HEB is the result of recombination between carriers in high energy delocalised states, these carriers may be more susceptible to non-radiative recombination processes that are mitigated for carriers in the localised ground states, such as recombination at threading dislocations or point defects [21, 22]. Further investigations are required to determine the nature of the recombination.

In the TRPL experiments, it was shown that the QW ground state emission continues to red shift over time after the HEB emission has completely decayed away (Figure 6.10). These TRPL spectra are much more similar in form to the QW ground state TIPL spectra produced at low excited carrier densities than to the spectra where the HEB dominates. However, the TIPL measurements show that the initial carrier density used to produce these spectra is within the efficiency droop regime. It may be the case that this represents a mid-point region where higher energy carriers are weakly localised enough that non-radiative processes become competitive, but that the spectrum is not dominated by the more weakly localised (or delocalised) carriers whose recombination gives rise to the HEB.

6.5 Summary and Conclusions

TIPL spectra of three InGaN/GaN single QW structures with different QW In fractions measured over a range of peak excited carrier densities showed the emergence of a HEB which coincides with the onset efficiency droop. The HEB occurs on the

high energy side of the QW ground state emission in all of the samples, and its peak energy at a particular excited carrier density shifts with QW In fraction, ruling out its origin as defect luminescence from the bulk GaN.

TRPL spectra showed that the HEB decays on much faster time scales than the QW ground state emission, with a decay time that increases with decreasing emission energy. This behaviour was studied in more detail through PL time decay measurements, which revealed plateaus in the decays detected across the HEB. These plateaus precede an exponential decay, and the duration of the plateau increases with decreasing detection energy across the HEB. For a given detection energy, the plateau duration increases with increasing excited carrier density. This behaviour strongly resembles that of self-assembled QDs, in which plateaus have been detected on PL peaks at carrier densities where peaks from higher order dot states were also present in the spectra. In the QD case, the plateaus were attributed to the refilling of lower energy states by carriers scattering down from higher energy states. Analogous behaviour may occur for hole states in InGaN/GaN QW. A simple Monte-Carlo simulation was produced to illustrate this model.

Comparisons were made to theoretical work in which it was shown that hole states are strongly localised up to 100 meV into the VB for In fractions as low as 10 %. Hole states at higher energies experience larger modulus wavefunction overlaps with other hole states, and so can be considered to be weakly localised or delocalised. The same theoretical work also demonstrated that the electron-hole modulus wavefunction overlap increases with increasing hole energy, which would be expected to lead to an increasing radiative recombination rate. It is likely that the HEB is due to recombination involving holes in these less localised states. The exponential part of the decays could indicate that they are due to excitonic recombination, but as the total integrated intensity of the PL spectrum is saturating, or drooping, over the investigated range of carrier densities, it must be considered that a non-radiative recombination process is also active. Holes in weakly localised or delocalised states may

be more susceptible to non-radiative recombination processes, such as recombination at threading dislocations or point defects. In the model of Tanner *et al.* [56], a weakly localised or delocalised hole experiences a large wavefunction overlap with all electron states. This would be expected to lead to non-exponential PL decays. Therefore, the form of the decays on the HEB in this work may be further evidence that the dominant recombination process is non-radiative.

6.6 References

[1] C. Weisbuch *et al.* "The efficiency challenge of nitride light-emitting diodes for lighting". *physica status solidi (a)* **212**, 5 (2015), 899. DOI: 10.1002/pssa.201431868 (Cited on pages 154, 158).

[2] Y. Narukawa. "White-Light LEDS". *Optics and Photonics News* **15**, 4 (2004), 24. DOI: 10.1364/OPN.15.4.000024 (Cited on page 154).

[3] P. Pust *et al.* "A revolution in lighting". *Nature Materials* **14**, 5 (2015), 454. DOI: 10.1038/nmat4270 (Cited on page 154).

[4] J. Iveland *et al.* "Auger effect identified as main cause of efficiency droop in LEDs". *SPIE Newsroom* **1**, c (2014), 2. DOI: 10.1117/2.1201406.005109 (Cited on pages 154, 155, 160, 161).

[5] Y. C. Shen *et al.* "Auger recombination in InGaN measured by photoluminescence". *Applied Physics Letters* **91**, 14 (2007), 141101. DOI: 10.1063/1.2785135 (Cited on pages 154, 155, 156, 158, 159).

[6] K. T. Delaney *et al.* "Auger recombination rates in nitrides from first principles". *Applied Physics Letters* **94**, 19 (2009), 191109. DOI: 10.1063/1.3133359 (Cited on pages 154, 155, 159, 160).

[7] E. Kioupakis *et al.* "Indirect Auger recombination as a cause of efficiency droop in nitride light-emitting diodes". *Applied Physics Letters* **98**, 16 (2011), 161107. DOI: 10.1063/1.3570656 (Cited on pages 154, 155, 156, 160, 162).

[8] E. Kioupakis *et al.* "First-principles calculations of indirect Auger recombination in nitride semiconductors". *Physical Review B* **92**, 3 (2015), 035207. DOI: 10.1103/PhysRevB.92.035207 (Cited on pages 154, 155, 160, 162).

[9] M. Binder *et al.* "Identification of nnp and npp Auger recombination as significant contributor to the efficiency droop in (GaIn)N quantum wells by visualization of hot carriers in photoluminescence". *Applied Physics Letters* **103**, 7 (2013), 071108. DOI: 10.1063/1.4818761 (Cited on pages 154, 155, 158, 159, 160).

[10] J. Iveland *et al.* "Direct Measurement of Auger Electrons Emitted from a Semiconductor Light-Emitting Diode under Electrical Injection: Identification of the Dominant Mechanism for Efficiency Droop". *Physical Review Letters* **110**, 17 (2013), 177406. DOI: 10.1103/PhysRevLett.110.177406 (Cited on pages 154, 155, 160, 161).

[11] J. Iveland *et al.* "Origin of electrons emitted into vacuum from InGaN light emitting diodes". *Applied Physics Letters* **105**, 5 (2014), 052103. DOI: 10.1063/1.4892473 (Cited on pages 154, 155, 160, 161).

[12] K. W. Williams *et al.* "Ultrafast and band-selective Auger recombination in InGaN quantum wells". *Applied Physics Letters* **108**, 14 (2016), 141105. DOI: 10.1063/1.4945669 (Cited on pages 154, 155, 160, 161).

[13] T. Sadi *et al.* "On the correlation of the Auger generated hot electron emission and efficiency droop in III-N light-emitting diodes". *Applied Physics Letters* **105**, 9 (2014), 091106. DOI: 10.1063/1.4894862 (Cited on pages 154, 155, 161).

[14] M. Shahmohammadi *et al.* "Enhancement of Auger recombination induced by carrier localization in InGaN/GaN quantum wells". *Physical Review B* **95**, 12 (2017), 125314. DOI: 10.1103/PhysRevB.95.125314 (Cited on pages 154, 155, 158, 159, 162, 163, 169).

[15] M.-H. Kim *et al.* "Origin of efficiency droop in GaN-based light-emitting diodes". *Applied Physics Letters* **91**, 18 (2007), 183507. DOI: 10.1063/1.2800290 (Cited on pages 154, 155, 163).

[16] M. F. Schubert *et al.* "On resonant optical excitation and carrier escape in GaInN/GaN quantum wells". *Applied Physics Letters* **94**, 8 (2009), 081114. DOI: 10.1063/1.3089691 (Cited on pages 154, 155, 163).

[17] J.-Y. Chang *et al.* "Advantages of blue InGaN light-emitting diodes with AlGaN barriers". *Optics Letters* **35**, 9 (2010), 1368. DOI: 10.1364/OL.35.001368 (Cited on pages 154, 155, 163, 164).

[18] D.-P. Han *et al.* "Nonradiative recombination mechanisms in InGaN/GaN-based light-emitting diodes investigated by temperature-dependent measurements". *Applied Physics Letters* **104**, 15 (2014), 151108. DOI: 10.1063/1.4871870 (Cited on pages 154, 155, 163, 164).

[19] T. Schulz *et al.* "Recombination dynamics in InGaN quantum wells - Contribution of excited subband recombination to carrier leakage". *Applied Physics Letters* **105**, 18 (2014), 181109. DOI: 10.1063/1.4901256 (Cited on pages 154, 155, 163, 164, 165).

[20] F. Nippert *et al.* "Polarization-induced confinement of continuous hole-states in highly pumped, industrial-grade, green InGaN quantum wells". *Journal of Applied Physics* **119**, 21 (2016), 215707. DOI: 10.1063/1.4953254 (Cited on pages 154, 155, 159, 163, 164, 165, 170).

[21] T. Mukai *et al.* "Characteristics of InGaN-Based UV/Blue/Green/Amber/Red Light-Emitting Diodes". *Japanese Journal of Applied Physics* **38**, Part 1, No. 7A (1999), 3976. DOI: 10.1143/JJAP.38.3976 (Cited on pages 154, 155, 159, 166, 193).

[22] J. Hader *et al.* "Density-activated defect recombination as a possible explanation for the efficiency droop in GaN-based diodes". *Applied Physics Letters* **96**, 22 (2010), 221106. DOI: 10.1063/1.3446889 (Cited on pages 154, 155, 166, 193).

[23] S.-W. Feng *et al.* "Multiple-component photoluminescence decay caused by carrier transport in InGaN/GaN multiple quantum wells with indium aggregation structures". *Applied Physics Letters* **80**, 23 (2002), 4375. DOI: 10.1063/1.1484546 (Cited on pages 154, 155, 166, 168, 169, 192).

[24] N. I. Bochkareva *et al.* "Efficiency droop and incomplete carrier localization in InGaN/GaN quantum well light-emitting diodes". *Applied Physics Letters* **103**, 19 (2013), 191101. DOI: 10.1063/1.4828780 (Cited on pages 154, 155, 166, 167, 168, 192).

[25] S. Hammersley *et al.* "The consequences of high injected carrier densities on carrier localization and efficiency droop in InGaN/GaN quantum well structures". *Journal of Applied Physics* **111**, 8 (2012), 083512. DOI: 10.1063/1.3703062 (Cited on pages 154, 155, 166, 167, 168).

[26] M. J. Davies *et al.* "High excitation carrier density recombination dynamics of InGaN/GaN quantum well structures: Possible relevance to efficiency droop". *Applied Physics Letters* **102**, 2 (2013), 022106. DOI: 10.1063/1.4781398 (Cited on pages 154, 155, 166, 167, 169, 192).

[27] G. Sun *et al.* "Investigation of fast and slow decays in InGaN/GaN quantum wells". *Applied Physics Letters* **99**, 8 (2011), 081104. DOI: 10.1063/1.3627166 (Cited on pages 154, 155, 166, 168, 169, 192).

[28] K. Nomeika *et al.* "Impact of carrier localization and diffusion on photoluminescence in highly excited cyan and green InGaN LED structures". *Journal of Luminescence* **188** (2017), 301. DOI: 10.1016/j.jlumin.2017.04.055 (Cited on pages 154, 155, 166, 168, 169).

[29] A. Dunn *et al.* "Investigating efficiency droop in InGaN/GaN quantum well structures using ultrafast time-resolved terahertz and photoluminescence spectroscopy". *physica status solidi (c)* **13**, 5-6 (2016), 252. DOI: 10.1002/pssc.201510193 (Cited on pages 154, 155, 166, 168, 169, 192).

[30] J. I. Pankove. *Optical Processes in Semiconductors*. Dover, 1975, 422 (Cited on page 155).

[31] A. R. Beattie and P. T. Landsberg. "Auger Effect in Semiconductors". *Proceedings of the Royal Society A: Mathematical, Physical and Engineering Sciences*. Vol. 249. 1256. 1959, 16. DOI: 10.1098/rspa.1959.0003 (Cited on page 155).

[32] A. R. Beattie and G. Smith. "Recombination in Semiconductors by a Light Hole Auger Transition". *physica status solidi (b)* **19**, 2 (1967), 577. DOI: 10.1002/pssb.19670190209 (Cited on page 155).

[33] M. Takeshima. "Auger recombination in InAs, GaSb, InP, and GaAs". *Journal of Applied Physics* **43**, 10 (1972), 4114. DOI: 10.1063/1.1660882 (Cited on page 155).

[34] B. Sermage *et al.* "Photoexcited carrier lifetime and Auger recombination in 1.3-μm InGaAsP". *Applied Physics Letters* **42**, 3 (1983), 259. DOI: 10.1063/1.93907 (Cited on page 155).

[35] J. Hader *et al.* "Beyond the ABC: carrier recombination in semiconductor lasers". *2006 International Conference on Numerical Simulation of Semiconductor Optoelectronic Devices*. Vol. 6115. IEEE, 2006, 39. DOI: 10.1109/NUSOD.2006.306730 (Cited on pages 157, 159).

[36] J. Piprek. "Efficiency droop in nitride-based light-emitting diodes". *physica status solidi (a)* **207**, 10 (2010), 2217. DOI: 10.1002/pssa.201026149 (Cited on page 158).

[37] P. G. Eliseev *et al.* "Recombination balance in green-light-emitting GaN/InGaN/AlGaN quantum wells". *Applied Physics Letters* **75**, 24 (1999), 3838. DOI: 10.1063/1.125473 (Cited on pages 158, 159).

[38] M. Shatalov *et al.* "Differential Carrier Lifetime in AlGaN Based Multiple Quantum Well Deep UV Light Emitting Diodes at 325 nm". *Japanese Journal of Applied Physics* **41**, Part 2, No. 10B (2002), L1146. DOI: 10.1143/JJAP.41.L1146 (Cited on pages 158, 159).

[39] K. A. Bulashevich and S. Y. Karpov. "Is Auger recombination responsible for the efficiency rollover in III-nitride light-emitting diodes?" *physica status solidi (c)* **5**, 6 (2008), 2066. DOI: 10.1002/pssc.200778414 (Cited on pages 158, 159).

[40] Z.-H. Zhang *et al.* "InGaN/GaN multiple-quantum-well light-emitting diodes with a grading InN composition suppressing the Auger recombination". *Applied Physics Letters* **105**, 3 (2014), 033506. DOI: 10.1063/1.4891334 (Cited on page 158).

[41] J. Hader *et al.* "On the importance of radiative and Auger losses in GaN-based quantum wells". *Applied Physics Letters* **92**, 26 (2008), 261103. DOI: 10.1063/1.2953543 (Cited on pages 158, 159).

[42] F. Bertazzi *et al.* "A numerical study of Auger recombination in bulk InGaN". *Applied Physics Letters* **97**, 23 (2010), 231118. DOI: 10.1063/1.3525605 (Cited on pages 158, 160).

[43] G. Verzellesi *et al.* "Efficiency droop in InGaN/GaN blue light-emitting diodes: Physical mechanisms and remedies". *Journal of Applied Physics* **114**, 7 (2013), 071101. DOI: 10.1063/1.4816434 (Cited on page 159).

[44] A. David and M. J. Grundmann. "Influence of polarization fields on carrier lifetime and recombination rates in InGaN-based light-emitting diodes". *Applied Physics Letters* **97**, 3 (2010), 033501. DOI: 10.1063/1.3462916 (Cited on page 159).

[45] H.-Y. Ryu *et al.* "Analysis of efficiency droop in nitride light-emitting diodes by the reduced effective volume of InGaN active material". *Applied Physics Letters* **100**, 13 (2012), 131109. DOI: 10.1063/1.3698113 (Cited on page 159).

[46] T. H. Ngo *et al.* "Photo-induced droop in blue to red light emitting InGaN/GaN single quantum wells structures". *Journal of Applied Physics* **122**, 6 (2017), 063103. DOI: 10.1063/1.4997608 (Cited on page 159).

[47] C. M. Jones *et al.* "Impact of carrier localization on recombination in InGaN quantum wells and the efficiency of nitride light-emitting diodes: Insights from theory and numerical simulations". *Applied Physics Letters* **111**, 11 (2017), 113501. DOI: 10.1063/1.5002104 (Cited on page 159).

[48] J. Hader *et al.* "Supression of carrier recombination in semiconductor lasers by phase-space filling". *Applied Physics Letters* **87**, 20 (2005), 201112. DOI: 10.1063/1.2132524 (Cited on page 159).

[49] J. Cho *et al.* "Efficiency droop in light-emitting diodes: Challenges and countermeasures". *Laser & Photonics Reviews* **7**, 3 (2013), 408. DOI: 10.1002/lpor.201200025 (Cited on page 159).

[50] J. Wang *et al.* "Understanding efficiency droop effect in InGaN/GaN multiple-quantum-well blue light-emitting diodes with different degree of carrier localization". *Applied Physics Letters* **97**, 20 (2010), 201112. DOI: 10.1063/1.3520139 (Cited on page 159).

[51] G. Rossbach *et al.* "High-temperature Mott transition in wide-band-gap semiconductor quantum wells". *Physical Review B* **90**, 20 (2014), 201308. DOI: 10.1103/PhysRevB.90.201308 (Cited on page 162).

[52] P. Hurst *et al.* "Temperature Dependent Optical Properties of InGaN/GaN Quantum Well Structures". *physica status solidi (b)* **228**, 1 (2001), 137. DOI: 10.1002/1521-3951(200111)228:1<137::AID-PSSB137>3.0.CO;2-R (Cited on page 163).

[53] J. R. Lang *et al.* "Carrier escape mechanism dependence on barrier thickness and temperature in InGaN quantum well solar cells". *Applied Physics Letters* **101**, 18 (2012), 181105. DOI: 10.1063/1.4765068 (Cited on page 163).

[54] M. A. Reshchikov *et al.* "Behavior of 2.8- and 3.2-eV photoluminescence bands in Mg-doped GaN at different temperatures and excitation densities". *Physical Review B* **59**, 20 (1999), 13176. DOI: 10.1103/PhysRevB.59.13176 (Cited on page 164).

[55] C.-M. Lee *et al.* "Temperature dependence of the radiative recombination zone in InGaN/GaN multiple quantum well light-emitting diodes". *Journal of Applied Physics* **89**, 11 (2001), 6554. DOI: 10.1063/1.1370995 (Cited on page 164).

[56] D. S. P. Tanner *et al.* "Random alloy fluctuations and structural inhomogeneities in c-plane InGaN quantum wells: theory of ground and excited electron and hole states". *RSC Advances* **6**, 69 (2016), 64513. DOI: 10.1039/C6RA07540A (Cited on pages 165, 191, 192, 195).

[57] P. Dawson *et al.* "The nature of carrier localisation in polar and nonpolar InGaN/GaN quantum wells". *Journal of Applied Physics* **119**, 18 (2016), 181505. DOI: 10.1063/1.4948237 (Cited on page 165).

[58] P. G. Eliseev *et al.* "Blue temperature-induced shift and band-tail emission in InGaN-based light sources". *Applied Physics Letters* **71**, 5 (1997), 569. DOI: 10.1063/1.119797 (Cited on page 167).

[59] Y.-H. Cho *et al.* "S-shaped temperature-dependent emission shift and carrier dynamics in InGaN/GaN multiple quantum wells". *Applied Physics Letters* **73**, 10 (1998), 1370. DOI: 10.1063/1.122164 (Cited on page 167).

[60] O. Rubel *et al.* "Quantitative description of disorder parameters in (GaIn)(NAs) quantum wells from the temperature-dependent photoluminescence spectroscopy". *Journal of Applied Physics* **98**, 6 (2005), 063518. DOI: 10.1063/1.2058192 (Cited on page 167).

[61] S. Schulz *et al.* "Atomistic analysis of the impact of alloy and well-width fluctuations on the electronic and optical properties of InGaN/GaN quantum wells". *Physical Review B* **91**, 3 (2015), 035439. DOI: 10.1103/PhysRevB.91.035439 (Cited on page 168).

[62] D. M. Graham *et al.* "Optical and microstructural studies of InGaN/GaN single-quantum-well structures". *Journal of Applied Physics* **97**, 10 (2005), 103508. DOI: 10.1063/1.1897070 (Cited on pages 170, 171, 181).

[63] M. A. Reshchikov and H. Morkoc. "Luminescence properties of defects in GaN". *Journal of Applied Physics* **97**, 6 (2005), 061301. DOI: 10.1063/1.1868059 (Cited on page 175).

[64] B. Monemar *et al.* "Radiative recombination in In0.15Ga0.85N/GaN multiple quantum well structures". *MRS Internet Journal of Nitride Semiconductor Research* **4**, 01 (1999), e16. DOI: 10.1557/S1092578300000727 (Cited on page 180).

[65] T. Kuroda and A. Tackeuchi. "Influence of free carrier screening on the luminescence energy shift and carrier lifetime of InGaN quantum wells". *Journal of Applied Physics* **92**, 6 (2002), 3071. DOI: 10.1063/1.1502186 (Cited on page 180).

[66] H. Gotoh *et al.* "Piezoelectric effects on photoluminescence properties in 10-nm-thick InGaN quantum wells". *Applied Physics Letters* **83**, 23 (2003), 4791. DOI: 10.1063/1.1632539 (Cited on page 180).

[67] P. D. Buckle *et al.* "Photoluminescence decay time measurements from self-organized InAs/GaAs quantum dots". *Journal of Applied Physics* **86**, 5 (1999), 2555. DOI: 10.1063/1.371092 (Cited on pages 186, 189).

[68] S. Grosse *et al.* "Carrier relaxation dynamics in quantum dots: Scattering mechanisms and state-filling effects". *Physical Review B* **55**, 7 (1997), 4473. DOI: 10.1103/PhysRevB.55.4473 (Cited on pages 186, 187, 189).

[69] F. Adler *et al.* "Optical transitions and carrier relaxation in self assembled InAs/GaAs quantum dots". *Journal of Applied Physics* **80**, 7 (1996), 4019. DOI: 10.1063/1.363361 (Cited on page 186).

[70] M. J. Steer *et al.* "Electronic energy levels and energy relaxation mechanisms in self-organized InAs/GaAs quantum dots". *Physical Review B* **54**, 24 (1996), 17738. DOI: 10.1103/PhysRevB.54.17738 (Cited on page 186).

[71] M. Grundmann and D. Bimberg. "Theory of random population for quantum dots". *Physical Review B* **55**, 15 (1997), 9740. DOI: 10.1103/PhysRevB.55.9740 (Cited on page 186).

[72] S. Hammersley. "Optical Studies of Group III-Nitride Semiconductors". PhD thesis. University of Manchester, 2011 (Cited on page 192).

Chapter 7

Further Work

It was shown that the efficiency of InGaN/GaN MQW structures containing Si-doped ULs decreases as the number of QWs increases. This was attributed to the reduction in the strength of the surface polarisation field due to the increasing distance between the UL and the sample surface. In a series of MQW structures that did not contain ULs, the efficiency was found to increase with increasing number of QWs. This has previously been attributed to an increased probability of the recapturing of carriers that would otherwise be lost through thermionic emission, or to the improvement in interface quality by impurity gettering following the growth of successive layers. As the MQW samples that did not contain ULs were grown under considerably different conditions to the series with ULs, the comparisons that can be made between the two series are limited. Therefore, a series of QW structures should be produced by the same growth method with exactly the same QW alloy compositions and QW and barrier thicknesses as the UL series, but without ULs. A thorough investigation into the radiative and non-radiative recombination rates for all of the samples can then be undertaken to determine how the effects of the UL and of the number of QWs on the IQE of a MQW structure compete with each other.

PL excitation spectroscopy and temperature dependent PL time decay measurements on the 10 and 15 QW structures containing ULs may be informative in deter-

mining if it is possible to resolve a separate emission feature due to the QW closest to the UL, as the net electric field across this QW in these structures is slightly reduced compared to the others.

For the series of single QW structures with varying GaN cap layer thickness, the shape of the PL decays detected on the low energy side of the emission peak was found to be different from that of the other decays detected at all energies for all of the other samples when plotted on a reduced time scale. This may be due to the fact that the net electric field is in the opposite direction to the strain-induced polarisation field in some regions of this QW, which could lead to electrons being localised at the bottom QW interface where it is expected that there are fewer QWWFs compared to the top. This would mean that the in-plane "localisation landscape" for the electrons is modified in these regions and would cause the PL decay curves to have a different shape. Alternatively, the In atoms in some regions of this QW may have penetrated through the upper barrier and to the surface due to the 1T growth method. This could also lead to a different localisation landscape for electrons. This could be confirmed or ruled out by detailed microstructural characterisation of all of the samples.

A high energy emission band (HEB) was observed in single QW structures with different In composition fractions at high excitation power densities. This emission was attributed to recombination involving holes in weakly localised or delocalised states. As the occurrence of the HEB coincided with the onset of the efficiency droop, it was suggested that the dominant recombination pathway for this emission is be non-radiative, with the weakly localised or delocalised holes being more likely to recombine at defects. To investigate this possibility, the HEB PL decay dynamics could be investigated in QW structures with different known threading dislocation and/or point defect densities. If the efficiency droop is found to occur at lower carrier densities in QWs with a higher defect density, this would provide further evidence that the recombination of weakly localised or delocalised carriers at defects is the main cause of droop. If the HEB is caused by the recombination of these weakly localised

or delocalised carriers, it would be expected that the non-radiative recombination rate would increase with increasing defect density for recombination at these energies. This would lead to the observation of faster PL decays detected across the HEB.

The investigations into the HEB presented in this thesis were all performed at 10 K. Temperature dependent studies of the HEB PL emission and decay dynamics should be undertaken with the aim of understanding its behaviour under device operating conditions (that is, room temperature).

Appendix A

Carrier Density Dependent Time-Integrated Photoluminescence Spectra of Single Quantum Wells

TIPL spectra obtained at 10 K for the 15 % (sample C187, Figure A.1) and 19 % (sample C189, Figure A.2) In fraction single QW structures are shown in this Appendix at various peak excited carrier densities. All of the samples exhibited a HEB at carrier densities above $\sim 10^{12}\,\mathrm{cm}^{-2}\,\mathrm{pulse}^{-1}$, the FWHM of which increases with increasing excited carrier density. Investigations into the carrier dynamics of the HEB, as well as its possible origins, are presented in Chapter 6.

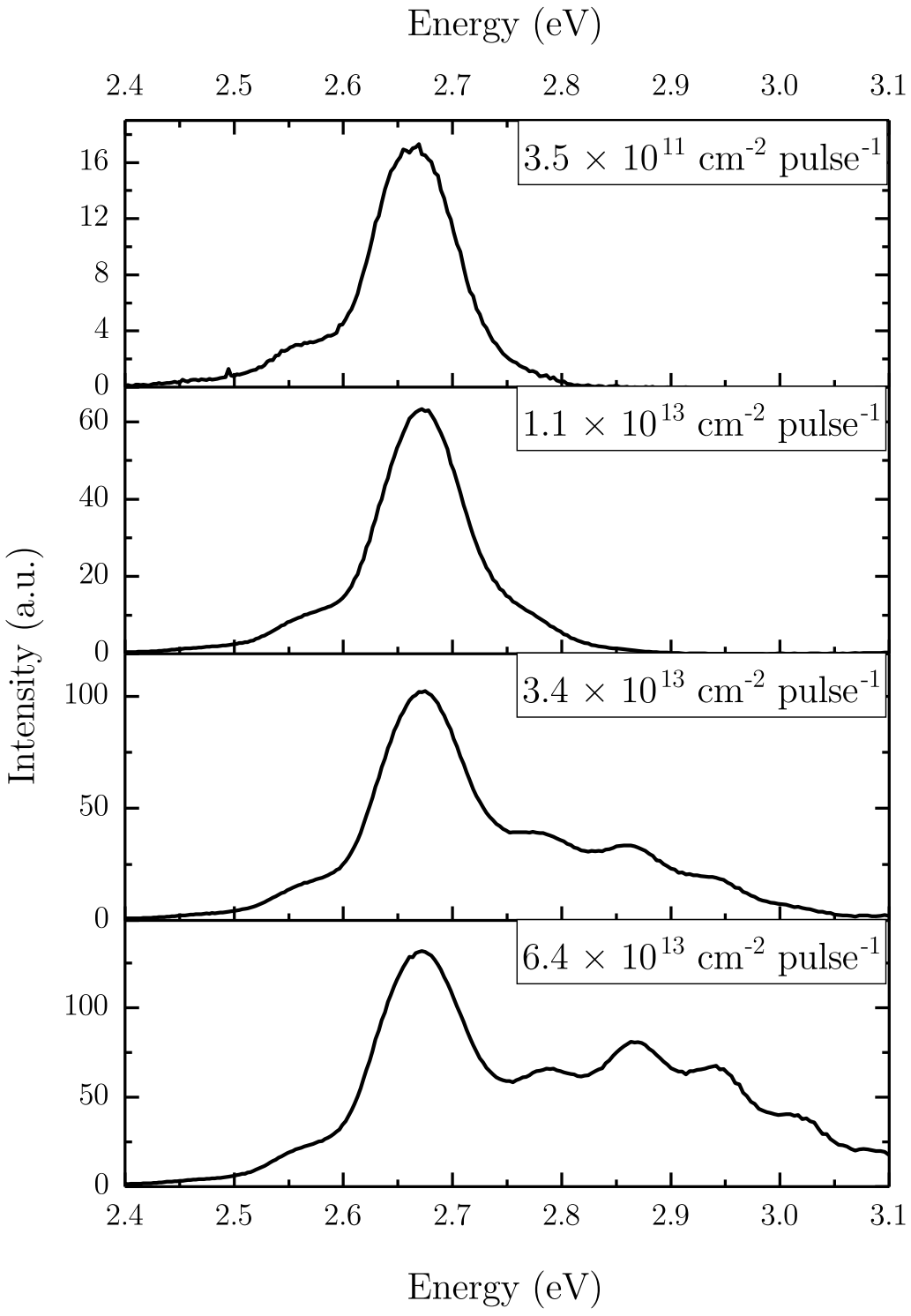

Figure A.1: TIPL spectra for the 15 % In single QW sample, measured at 10 K, at various peak carrier densities.

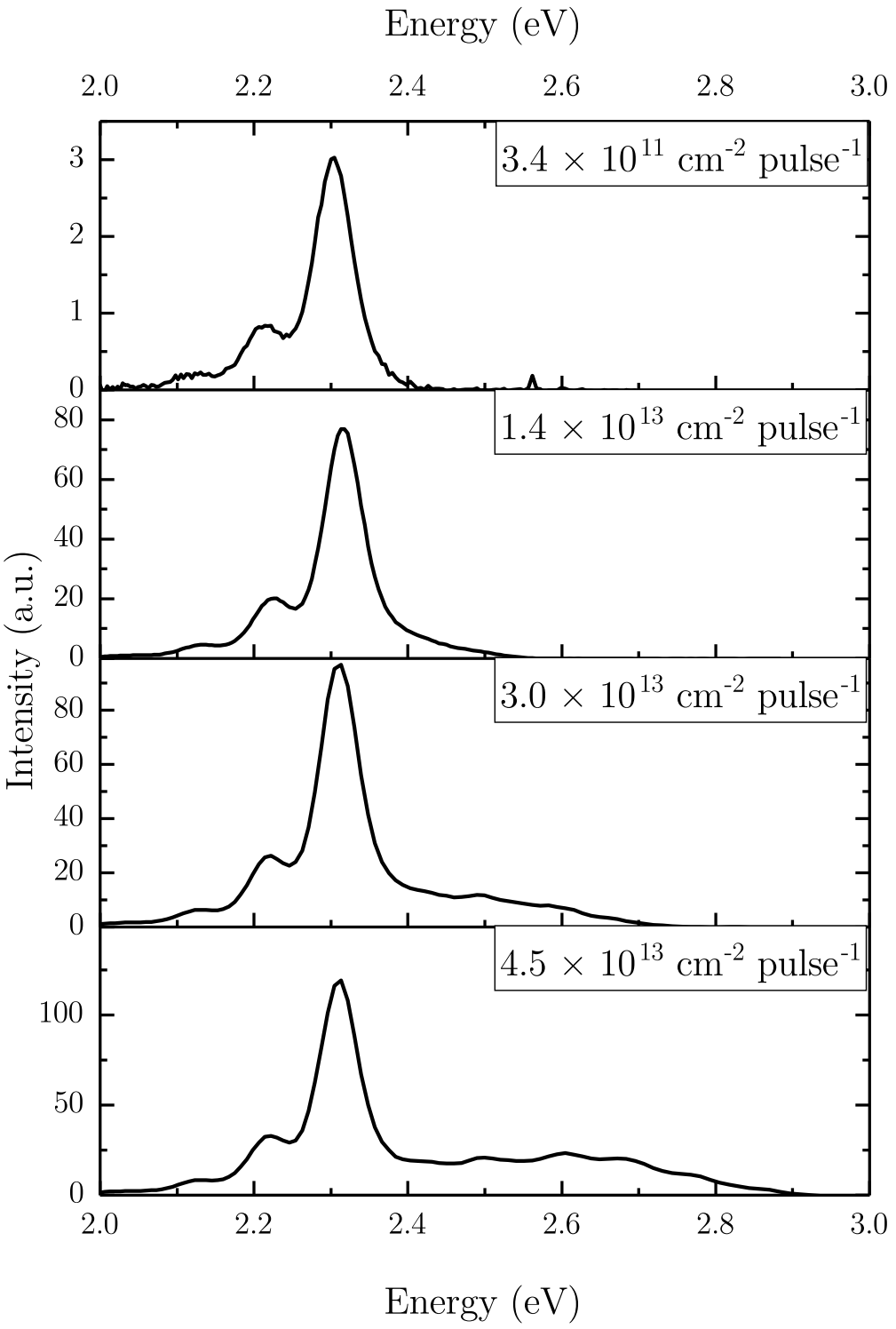

Figure A.2: TIPL spectra for the 19 % In single QW sample, measured at 10 K, at various peak carrier densities.